UNIVERSITY OF CALIFORNIA,
IRVINE

# Catalyst Layer Interfaces in Polymer Electrolyte Fuel Cells from Kinetics and Morphological Perspectives

DISSERTATION

submitted in partial satisfaction of the requirements
for the degree of

DOCTOR OF PHILOSOPHY

in Chemical and Biomolecular Engineering

by
Arezoo Avid

Dissertation Committee:

Associate Professor Iryna Zenyuk, Chair

Professor Plamen Atanassov

Assistant Professor Stacy Copp

2022

## DEDICATION

This work is dedicated to my loving parents, Mehran Avid and Parivash Ghadyani

in recognition of their love, support, and faith in me.

**TABLE OF CONTENTS**

Page

## LIST OF FIGURES

## LIST OF TABLES

## ACKNOWLEDGEMENTS

I would like to express my sincere gratitude and appreciation to my advisor, Professor Iryna V. Zenyuk, who has the substance of a genius and hard-working scientist. My conversations with her inspired me from multiple perspectives and has led me to the right path, both academically and personally. She continuously provided encouragement and always went above and beyond to assist in any way she could throughout my Ph.D. journey. Words cannot express how grateful I am to have her as my advisor, and I hope that I could be as energetic and enthusiastic member of energy profession as she is.

I would like to thank my committee members, Professor Plamen Atanassov whose guidance and support has been invaluable in this study, and Professor Stacy Copp for generously offering her time and advice throughout the process.

In addition, I thank my colleagues at SEE lab who have been a great source of support and friendship. I would like to thank Dr. Andrea Perego and Dr. Tristan Asset for wonderful collaborations and for passing their knowledge and experimental skills. I am thankful to Ying Huang, Jesus Lopez Ochoa, and Dr. Yuanchao Liu for their invaluable collaborating effort in ionic liquid project. I thank my lab mates, Dr. Yongzhen Qi, Kaustubh Khedekar, and Devashish Kulkarni for enthusiastic discussions and their inspiration during last four years.

I gratefully acknowledge support from National Fuel Cell Research Center and research funding from National Science Foundation and Electrochemical Society Toyota Young Investigator Fellowship.

Finally, I am forever indebted to my parents, Mehran Avid and Parivash Ghadyani. Their love and unconditional trust raised me up in hard times despite the long distance between us. I am extremely grateful to my sister, Azadeh Avid, for her emotional support, patience and encouragement. I could not have undertaken this journey without my family whose belief in me kept my spirits and motivation high.

# VITA

## Arezoo Avid

2010-2014 B.Sc. in Polymer Engineering, University of Tehran, Tehran, Iran

2014-2017 M.Sc. in Polymer Engineering, University of Tehran, Tehran, Iran

2018-2022 Ph.D. in Chemical and Biomolecular Engineering,
University of California, Irvine

## FIELD OF STUDY

Chemical and Biomolecular Engineering

## PUBLICATIONS

1- Avid, Arezoo, Jesus López Ochoa, Ying Huang, Yuanchao Liu, Plamen Atanassov, Iryna V. Zenyuk. “Ionic Liquids in Polymer Electrolyte Fuel Cells: New State-of-the-art in the Oxygen Reduction Reaction and Durability.” *Nature Communications* – Under review

2- Perego, Andrea, Arezoo Avid (co-first author), Divija N. Mamaniaa, Yechuan Chen, Plamen Atanassov, Hakan Yildirim, Madeleine Odgaard, and Iryna V. Zenyuk. "Investigation of Cathode Catalyst Layer Interfaces Evolution during Accelerated Stress Tests for Polymer Electrolyte Fuel Cells." *Applied Catalysis B: Environmental* 301 (2022): 120810.

3- Avid, Arezoo, Iryna V. Zenyuk, "Confinement effects for nano- electrocatalysts for oxygen reduction reaction", *Current Opinion in Electrochemistry* 25, 100634 (2021).

4- George, Thomas Y., Tristan Asset, Arezoo Avid, Plamen Atanassov, and Iryna V. Zenyuk. "Kinetic Isotope Effect as a Tool To Investigate the Oxygen Reduction Reaction on Pt-based Electrocatalysts–Part I: High-loading Pt/C and Pt Extended Surface." *ChemPhysChem* 21, no. 6 (2020): 468-468. (Front Cover article and Feature Article for the 06/2020 Special Issue)

5- Avid, Arezoo, Seyed Hassan Jafari, Hossein Ali Khonakdar, Mehdi Ghaffari, Beate Krause, and Petra Pötschke. "Surface modification of MWCNT and its influence on properties of paraffin/MWCNT nanocomposites as phase change material." *Journal of Applied Polymer Science* 137, no. 9 (2020): 48428.

6- Raee, Ehsan, Arezoo Avid, and Babak Kaffashi. "Effect of compatibilizer concentration on dynamic rheological behavior and morphology of thermo- plastic starch/polypropylene blends." *Journal of Applied Polymer Science* 137, no. 22 (2020): 48742.

# ABSTRACT OF THE DISSERTATION

Catalyst Layer Interfaces in Polymer Electrolyte Fuel Cells

from Kinetics and Morphological Perspectives

by

Arezoo Avid

Doctor of Philosophy in Chemical and Biomolecular Engineering

University of California, Irvine, 2022

Professor Iryna V. Zenyuk, Chair

In view of growing climate concerns and energy demands, polymer electrolyte fuel cells (PEFCs) are promising zero-emission energy-conversion technologies for stationary and mobile applications due to high thermodynamic efficiencies and power densities. However, their relatively short life and high cost are significant barriers to their widespread commercialization. Cathode catalyst layer (CL) plays a key role in design criteria of PEFC technology as significant performance decays occur there. Performance limitations stem from sluggish oxygen reduction reaction (ORR) kinetics, as well as proton and oxygen transport resistances in the CL. As a result, high loading of precious platinum (Pt) is needed to achieve sufficient current densities. ORR takes place at the interface of Pt and electrolyte; therefore, a deep understanding of the CL interface is vital for proposing novel designs to enhance Pt utilization. Moreover, degradation mechanisms of

CL components are not completely understood, and it is crucial to fully comprehend the interactions influencing the durability of the stack.

We have explored the ORR mechanism and reaction pathways using kinetic isotope effect (KIE) approach. The rate-determining step for ORR on dispersed Pt/C electrocatalyst and polycrystalline Pt was identified to be proton-independent. Nevertheless, when Pt is dispersed on a high surface area (HSA) support, morphological confinement becomes critical as it dictates proton and oxygen transport in the CL. We presented an overview of electrostatics and mass transport induced confinement that can be caused by ionic liquids (ILs) integration. We explored three imidazolium-derived ILs, selected for their high proton conductivity and oxygen solubility and incorporate them into HSA carbon black support. Nanoconfinements interpretation and their role on transport properties near Pt surface helped understand the ORR kinetics dependence on the morphology of the carbon-supported electrocatalyst. Further, we established a correlation between the physical properties and electrochemical performance of the IL-modified catalysts to provide guidance for catalyst interface modification and importantly design of highly durable and active Pt-based catalysts for PEFC application.

To understand the evolution of Pt|ionomer and carbon|ionomer interfaces in the CL during life cycle of PEFCs, electrodes with HSA and durable carbon supports were investigated using accelerated stress tests (ASTs). Electrochemical characterizations, as well as X-ray photoelectron spectroscopy (XPS) were utilized to assess degree of components degradation. Catalyst AST along with analytical methodologies brought thorough insight into the role of Pt|ionomer interface in fuel cell polarization loss. In addition, support AST results for HSA carbon showed that the degree of

ionomer degradation along with evolution of ionomer|carbon interface is responsible for performance decay.

# Chapter 1

# INTRODUCTION

## 1.1 Motivation

In the 21st century, rapid depletion of fossil fuels, concerns over climate change, and environment issues make the effective utilization of energy a critical issue. Atmospheric carbon dioxide ($CO_2$) level has increased 413 part per million, resulting in temperature rise and global warming. Taking proper initiatives to control the climate change by reducing greenhouse gas (GHG) production, particularly $CO_2$ emission, creates the need of exploiting renewable and sustainable energy sources toward an affordable energy technology in the future[1,2]. More than 24 % of the GHG emission worldwide stems from the transportation sector, among which the road vehicles are the main contributors responsible for 74 % of it[3]. In view of these issues, many countries are committed to decarbonization of energy systems by 2050. Battery electric vehicles will decarbonize the light-duty fleet to some extent, but for the heavy-duty transportation sector fuel cell electric vehicles (FCEVs) are promising alternative power sources to internal combustion engines, due to their low emission and high efficiency, between 40 and 60%; the efficiency can be even up to 85% if the waste heat can be utilized in cogeneration mode [4,5]. FCEVs have quick refueling time and high energy density designed for long driving range. California and other states already have existing hydrogen refueling infrastructure. Unlike passenger cars and buses that have reduced the petroleum consumption to some degree, long-haul trucks still rely heavily on diesel fuel making them responsible for a large portion of $CO_2$ production[6]. FCEVs rely on the zero-

emission energy-conversion technology of polymer electrolyte fuel cell (PEFC) with features including low operating temperature, high power density, and easy scale-up[7].

## 1.2 Polymer Electrolyte Fuel Cell

Fuel cell is an electrochemical device where compressed hydrogen fuel at the anode is oxidized to protons as charge carries ($H_2 \leftrightarrow 2H^+ + 2e^-$), and react with oxygen at the cathode to produce water and electricity ($4H^+ + 4e^- + O_2 \leftrightarrow 2H_2O$)[8].

Figure 1-1-1 illustrates a schematic of a PEFC. The core component of a PEFC is the membrane electrode assembly (MEA) consisting of a polymer electrolyte membrane (PEM) transporting the protons, sandwiched between the anode and cathode electrodes. Each electrode is composed of a gas diffusion layer (GDL) and catalyst layer (CL) where the half-cell electrochemical reaction occurs. GDLs are responsible for reactants transport, electron conduction, and water management. MEA is placed between two bipolar plates that introduce the reactants, collect the generated electric current, and transfer excess reactants and water product [9].

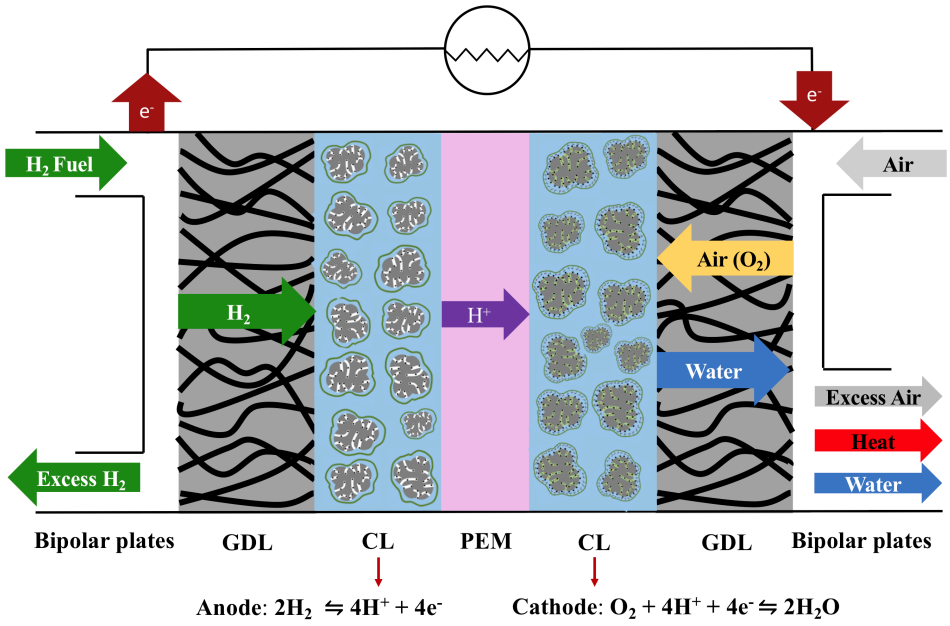


Figure 1-1. Schematic diagram of PEFC, transport processes and electrochemical reactions.

Typically, Platinum-based electrocatalyst are utilized for both hydrogen oxidation reaction (HOR) on anode and oxygen reduction reaction (ORR) on cathode. PEFC does not operate at the thermodynamic potential (1.229 V) and undergoes polarization losses during operation as shown in Figure 1-2.

Kinetic loss stems from the reactivity of the species and kinetics of the reaction on catalytic surface. Ohmic loss is due to the electronic resistance and proton transport resistance through PEM, and mass transport limitation is caused by flooding in the channels at high current densities and limited supply of reactants (oxygen and protons) to the reaction sites. ORR that occurs on the cathode side involves breakage of O=O double-bond and formation of four O-H bonds. This reaction is very sluggish and generates a high overpotential of more than 0.2 V. Kinetic loss in PEFCs limits the power density requiring high loadings of precious Pt metal to drive the ORR[10].

The significant polarization losses caused by the ORR, highlights the importance of understanding the ORR mechanism to enhance the activity of Pt-based electrocatalysts.

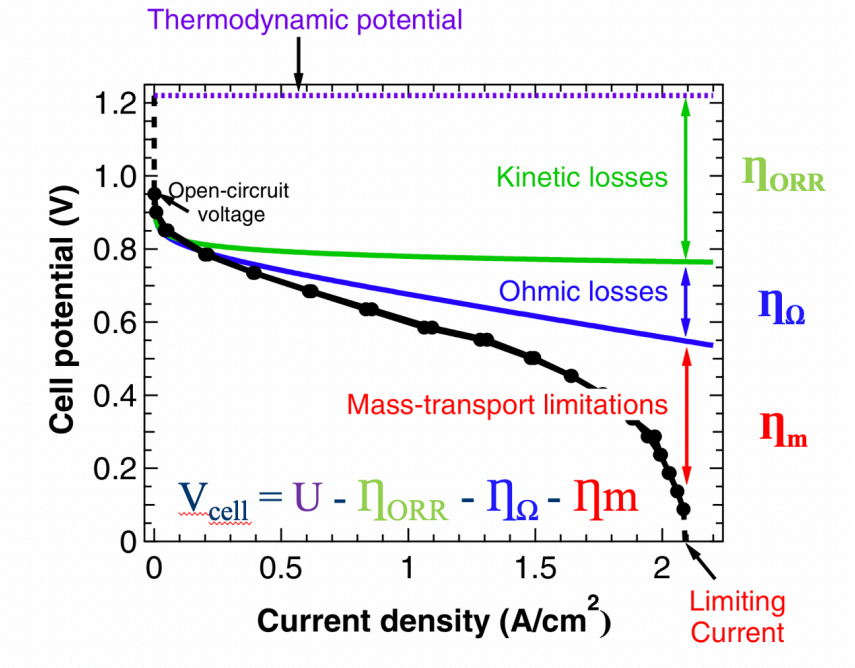


Figure 1-2 PEFC polarization losses[11].

## 1.3 Oxygen Reduction Reaction

It has been proposed that depending on the experimental conditions such as the potential, ORR takes place through two pathways: "direct 4e-" and a "series 2e- + 2e-" as shown below. ORR either proceeds directly to water (Equation 1-1) or via formation of hydrogen peroxide as an intermediate (Equation 1-2). Peroxide can further reduce to water (Equation 1-3) or decompose in acidic solution to $H_2O$ and $O_2$ (Equation 1-4)[12].

$$O_2 + 4H^+ + 4e^- \leftrightharpoons 2H_2O \qquad E^0 = 1.23\,V\ vs.\,RHE \qquad [1\text{-}1]$$

$$O_2 + 2H^+ + 2e^- \leftrightharpoons 2H_2O_2 \qquad E^0 = 0.7\,V\ vs.\,RHE \qquad [1\text{-}2]$$

$$H_2O_2 + 2H^+ + 2e^- \leftrightharpoons H_2O \qquad E^0 = 1.78\,V\ vs.\,RHE \qquad [1\text{-}3]$$

$$H_2O_2 \leftrightharpoons 2H_2O + \frac{1}{2}O_2 \qquad [1\text{-}4]$$

Typically, both associative and dissociative mechanisms are considered to occur depending on whether the $O_2$ molecule dissociates before reduction or not. The elementary steps of the associative mechanism are further described by the following equations[13] in which $OOH_{ads}$, $OH_{ads}$, $O_{ads}$ intermediates are involved.

$$O_2 + H^+ + e^- \longrightarrow OOH_{ads} \qquad [1\text{-}5]$$

$$OOH_{ads} + H^+ + e^- \longrightarrow H_2O + O_{ads} \qquad [1\text{-}6]$$

$$O_{ads} + H^+ + e^- \longrightarrow OH_{ads} \qquad [1\text{-}7]$$

$$OH_{ads} + H^+ + e^- \longrightarrow H_2O \qquad [1\text{-}8]$$

An alternative to water formation step (Equation 1-6) is the formation of hydrogen peroxide ($OOH_{ads} + H^+ + e^- \longrightarrow H_2O_2$) which will further proceed as explained above (Equation 1-2 to 1-4). The dissociative mechanism, however, involves $O_{ads}$ and $OH_{ads}$ intermediates only.

On Pt surfaces and nanostructures, oxygen first protonation (the $O_2 + H^+ + e^- \longrightarrow OOH_{ads}$ step) and $OH_{ads} + H^+ + e^- \longrightarrow H_2O$ are considered to be the potential determining step (RDS) of the ORR. Oxygen first protonation is consisted of the following steps, adsorption of molecular $O_2$ and direct transfer of proton/electron to it. (equation 1-9 to 1-11):

$$O_2 \longrightarrow O_{2,ads} \qquad [1\text{-}9]$$

$$O_{2,ads} + e^- \longrightarrow O_{2,ads}^- \qquad [1\text{-}10]$$

$$O_{2,ads}^- + H^+ \longrightarrow OOH_{ads} \qquad [1\text{-}11]$$

The electrochemical ORR has been the subject of numerous investigations; however, its detailed mechanism and predominant reaction pathway are still not well understood. A number of descriptor-based approaches have been applied to understand ORR mechanism and to improve the catalytic activity including linear scale relationships between the intermediates adsorption energies, thermodynamic analysis based on limiting potential and volcano plots, and microkinetic modeling of ORR[14]. Kinetic isotope effect (KIE) is one technique that will be studied thoroughly in the second chapter.

The main challenges of mass deployment of FCEVs are the cost, performance, and durability[15]. Currently, commercially-available FCEVs utilize high Pt loadings > 0.3 $mg_{Pt}$ $cm^{-2}$, which is higher than US Department of Energy's (DOE) 2020 performance target of 0.125 $g_{PGM}$ $kW^{-1}$ at rated power (total anode and cathode PGM areal loading of 0.125 $mg_{Pt}$ $cm^{-2}$ or cathode loading of 0.1 $mg_{Pt}$ $cm^{-2}$)[16].

Furthermore, durability concerns become even more significant within the context of heavy-duty fuel cell vehicles because of more stringent efficiency and lifetime targets compared to light-duty vehicles [6]. For heavy-duty trucks, the PEFC stack design requirements are different from existing automotive stacks: with more space available on board, power-to-weight ratio becomes subsidiary to durability aspects, since long-haul trucks must drive for up to 100,000 miles per year. Currently, the DOE lifetime goal set is 8,000 hours for automotive stacks, 20,000 hours for buses[17], and up to 30,000 hours for long haul tractor-trailers.[18,19] The technical targets for Class 8 long-haul fuel cell trucks are 25,000 h lifetime, 68% peak efficiency, and \$80/$kW_{net}$ fuel cell system cost by 2030

[19]. This To meet this durability criteria, further understanding of fundamental mechanisms of degradation within individual cell components is needed. Therefore, the development of low-cost, high-performing, and durable cathode electrodes is the key to the commercialization and mass production of affordable FCEVs for the transportation sector.

## 1.4 Catalyst Layer Structure

Catalyst layer (CL) is generally composed of electrocatalysts, electrolyte, and catalyst support. Perfluorinated sulfonic acid (PFSA) polymers (e.g., Famous DuPont's Nafion) consisting PTFE-like backbone and sulfonic acid groups have widely been used as the electrolyte due to the high chemical stability and acidity. Nafion enables the proton delivery to Pt active sites, and acts as a binder holding the CL mechanically together. To maximize electroactive surface area of the Pt nanoparticles, they are typically dispersed on either high surface area (HSA) Ketjenblack carbon black pr low surface area (LSA) Vulcan XC-72. Primary carbon black particles (~20 nm) are formed by assembly of micro-crystallites with micropores (< 2 nm) in between. Because of the tendency to aggregate, carbon blacks form agglomerates with mesopores (2–20nm). Inter-agglomerate pores are macropores (>20 nm).

High surface area carbon support is considered to be a great candidate for fuel cell application owing to its high internal mesoporosity. It can host up to 75% of Pt active surface area within the wide mesopores with size between 5.5 and 14 nm, but at the same time effectively deliver oxygen to Pt within pores [20]. Due to size-exclusion, ionomer does not penetrate pores below 20 nm in size; therefore, Pt nanoparticles present in the internal pores are not in contact with ionomer. This will reduce ionomer's sulfonate groups adsorption on Pt that are known to impede the kinetic activity towards ORR[21,22].

ORR occurs at the triple-phase boundary (TPB) of the solid Pt electrocatalyst deposited on the carbon support, electrolyte (ionomer), and oxygen gas. There are two governing principles controlling ORR that will be discussed thoroughly in the current work:

1) Kinetics of the ORR reaction on the surface of the electrocatalyst that involves the adsorption of reactants, interfacial charge transfer, and the desorption of intermediates/products near the active sites [23].

2) Mass transfer of the reactants, ions, and produced water toward and from the surface of the electrocatalyst. Therefore, a sufficient diffusion of oxygen in pore space and protons in the liquid media is vital for the ORR reaction.

## 1.5 Nanoconfinement

Nanoconfinement is imposed either by partial or complete encapsulation within a nanoscale cavity, pore, or channel. It can be also be induced by restriction of molecules or nanomaterials on the surface. Nanoconfinement contextualize the chemical reactivity of the confined spaces. The term 'molecular flask' was coined to describe artificial molecular containers that alter chemical reactivity through confinement[24].

In the CL of PEFC, the size of these micro- and meso-pores dictates the confinement for gas transport, as well as the proton transport due to electrostatics at solid-electrolyte interface. Confinement can also be induced by ionomer, ionic liquids (ILs) or other molecular additives. Confinement in thin-film ionomers is due to the polymer-catalyst interface, free surface interactions, and finite size effects[25]. Polymer properties, such as the backbone structure, equivalent weight, side-chain interaction with the substrate (specific adsorption etc.), and the chain

entanglement impact the degree of confinement [26]. Figure 1-3 summarizes the confinement effects that are technologically relevant for ORR and will be overviewed in this work.

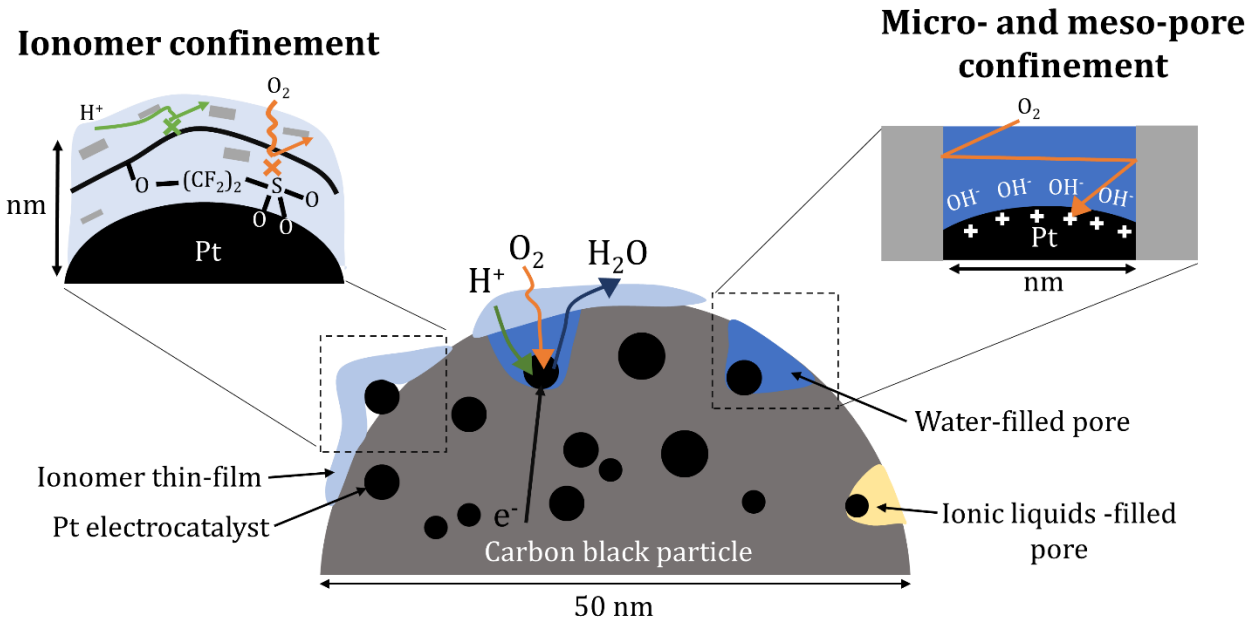


Figure 2-3 Schematic of a carbon-supported Pt electrocatalyst for ORR and associated transport phenomena. The interface between ionomer and Pt, and Pt within confined meso-pore are shown as well. Ionic liquids-filled pore is also shown in the schematic.

### 1.5.1 Nanoconfinement Effects on Ion Transport

Electric double layers (EDLs) form at the interface between the electrocatalyst and electrolyte. They are present whenever two dissimilar phases are in contact and equilibrium is established after the contact. EDLs result in preferential water dipole orientation at the interface, separation of charge, electron spillover and may include specific adsorption. The outer Helmholtz plane (OHP) is the plane of the closest approach for solvated ions and the solution plane of the diffuse double

layer. According to the classical Poisson-Boltzmann theory, EDLs diffuse layer thickness is expressed as the Debye length [27]:

$$\lambda = \sqrt{\frac{\epsilon RT}{F^2 \sum z_i^2 c_{i,bulk}}} \qquad [1\text{-}12]$$

where, $\epsilon$ is the dielectric permittivity, $R$ is the ideal gas constant, $T$ is temperature, $F$ is Faraday's constant, $z$ is charge number and $c_{i,bulk}$ is bulk ionic concentration. Confinement effect is pronounced when the pore size is less than twice the width of the EDLs causing the double layers to overlap. Figure 1-4a shows the plot of the Debye length as a function of ionic strength of solution, where a linear profile on logarithmic plot is observed. Water at pH of 7 and Nafion are approximated to be 1 M solution. On the right y-axis, pore sizes corresponding to micro, meso- and macro-pores are shown. The shaded region represents scenarios, where pores will be filled with electrolyte of specific concentration considered to be under confinement. For example, the Debye length for Nafion is 0.3 nm; thus, there will be no confinement effect for ion transport in the pores with the size of 0.6 nm or larger. For ILs, the double layer thickness was measured to be several nanometers [28], whereas ionic strength is measured to be in a range between $(2.77 - 5.3) \times 10^3$ mol/m$^3$ [29]. When micro-pores are less than 5 nm and filled with ILs, overlapped EDLs will be present, resulting in confinement. Figure 1-4b shows the two potential distributions within the water-filled and Nafion-filled pore of 12 nm radius [30]. Due to the low ionic strength of water, the surface charge on Pt cannot be shielded by ions present in water; therefore, the potential lines are almost straight within the pore. On the other hand, the double-layer thickness for Nafion-filled pore is only 0.3 nm; therefore, most of the potential drop is within the metal-OHP region, and no confinement is observed. Since the driving force for Faradaic reactions is from metal to OHP, having thin double layers is beneficial for ORR.

EDL structure with IL molecules and polymerized ionic liquid[31] show drastically different behavior than EDLs of aqueous electrolytes, where complex ion ordering at the interface is an active area of research including: the confinement effects[32] on EDL structure, potential[33,34] and molecular architecture[35,36] dependency of the interfacial ionic layer structure, developed theories and models on the state of the ions in the IL near the charged interface[37,38], the overall impact on the performance of the electrochemical systems such as batteries[39], and the design of surface-active ILs governing the energy density of the device[40]. In their seminal work, Bazant et al.[41] proposed two modes for ion distribution near the charged metal surface: 1) at potential of 0.26 V, the surface is over-screened with a monolayer of counterions, whereas 2) at higher potentials (2.6 V) ion crowding extends to two monolayers. This model assumes monotonic charging of metal surface (Figure 1-4c). Our earlier work reviewed in-detail the role of proton transport on ORR for water-filled and aqueous electrolytes[42]. Marion et al.[43] measured ion conductivities of imidazolium type ionic liquids in nanopores of 20–600 nm size glass capillaries, observing no confinement effect down to 20 nm pores showing that ionic liquids behave as glass liquids.

Studies have shown that thin-film ionomers have reduced conductivity by 1/7$^{th}$ of that of the bulk[44,45,46], reduction in the water uptake [47], and through-plane water diffusion coefficient[48]. Currently, ionomer confinement is generally studied with model systems[25],but is not well understood in actual catalyst layers. Figure 1-4e shows length-scales for ionomer confinement.

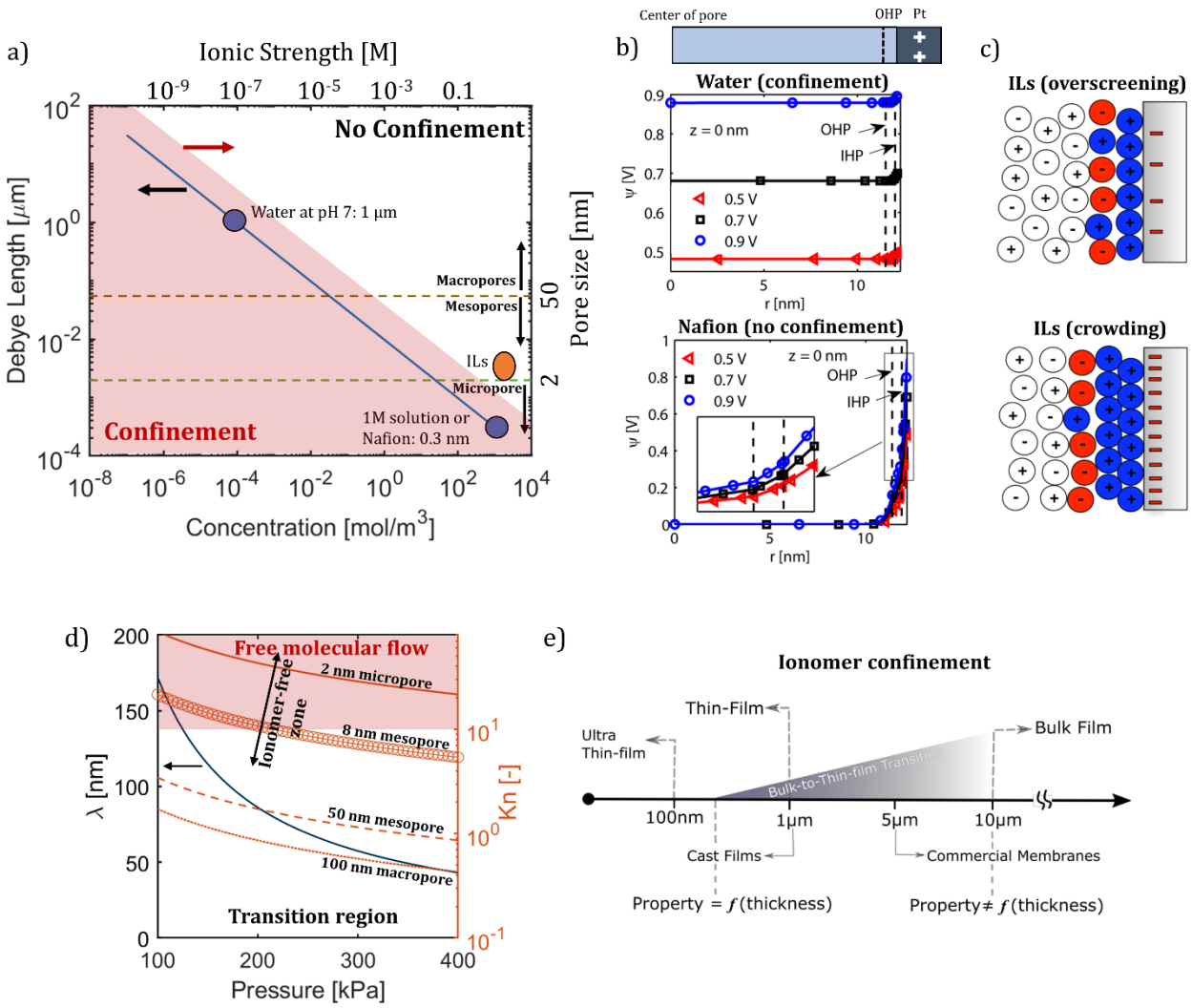


Figure 1-4 Confinement from the electrolyte perspective. a) Debye length as a function of ion concentration (or ionic strength), where linear relation is shown for aqueous electrolytes. Selected cases for DI water, 1 M solution or Nafion, and ILs are shown as well. The right-hand y-axis shown pore diameter and the shaded region represents definition of confinement. b) Potential distribution in 12 nm radius pore with Pt walls that is filled with water (top) and Nafion (bottom). Distribution for applied potentials of 0.5, 0.7 and 0.9 V are shown [30]. c) A schematic of ILs interface with a charged metal, where overscreening is observed for relatively low applied potentials (0.26 V), and ion crowding at interface is observed at high potentials (2.6 V) [41]. d) Gas mean free path for air as a function of gas pressure, where right y-axis shows Knudsen number. The Knudsen numbers for air in pores of 2, 8, 50

and 100 nm are shown too. Two regions of free molecular flow and transition regions are shown. e) Ionomer size from ultra-thin film to bulk film, where confinement effects are shown, adapted from [25].

### 1.5.2 Nanoconfinement Effects on Gas Transport

Here we define gas confinement, when the molecule interaction with the wall is more frequent than the gas molecule-to-molecule collision. In meso- and micro-pores, there are two transport regimes characterized by two length-scales. The first one is the viscous regime in which thermal mean free path, $\lambda_T \ll L_C$, where $L_C$ is the characteristic length-scale related to the dimension of the pore (for example a diameter for a cylindrical pore). The second transport regime is the free molecular flow, where $\lambda_T \gg L_C$, which was first investigated by Knudsen[49]. The Knudsen number, $Kn$ is defined as a ratio of thermal mean free path to characteristic length-scale, $Kn = \lambda_T / L_C$. In viscous regime, defined as $Kn < 0.1$, no confinement exists, and continuum theory can be applied to study the gas transport. For $Kn > 10$, the free molecular flow, gas is confined by nanostructure of the pore and so-called Knudsen diffusion takes place. In the transition region $0.1 < Kn < 10$, pressure-driven flow coexists with diffusion transport[50]. As presented in the study by Debe[51], the average time interval between oxygen molecules collision with the catalyst surface site determines the ORR rate determining step. In the Knudsen regime, the increased frequency of molecular collision with the pore wall will promote the ORR. Figure 1-4d shows mean free path for air across the range of pressure typically used in electrochemical conversion devices. Also, the Knudsen numbers are shown for the selected pores, where micro-pores and smaller meso-pores are located in the regime of the free molecular flow, as well as the pores where the ionomer is not present due to the size exclusion.

## 1.6 Scope of Thesis

This dissertation is divided into 5 chapters. Chapter 1 outlined the nanoconfinements in the catalyst layer of the PEFC that can be described as a state where polymer chains of ionomer are outside of their equilibrated state experiencing high strain. In chapter 2, kinetic isotope effect (KIE) has been applied to understand ORR mechanism and to identify the rate determining step of ORR. Although both oxygen gas and protons are ORR reactants, it was shown that protons do not participate in the rate-determining-step of the ORR. However, they can cause mass transport limitations when their transport is hindered by the confinements. In addition, oxygen gas transport is also affected by the confinements. Therefore, it is expected to observe an impact on the ORR activity induced by the confinement effects as will be discussed in chapter 3. Chapter 3 presents the novel approach of incorporating IL into the catalyst layer to improve the activity and long-term durability of Pt-based electrocatalysts towards ORR. To this end, using advanced electrochemical, imaging and spectroscopic techniques, the fundamental interactions at the catalyst layer interface were studied. Chapter 4 investigates the evolution of Pt|ionomer and carbon|ionomer interfaces during life cycle of PEFC electrodes with high surface area and durable carbon supports. Finally, chapter 5 reviews the conclusion and contributions of this research and makes recommendations for future work.

# Chapter 2

# Kinetic Isotope Effect as a Tool to Investigate the Oxygen Reduction Reaction on Pt-based Electrocatalysts. Part I: High-loading Pt/C and Pt Extended Surface

## 2.1 Introduction

As there is no firm consensus on primary reaction steps of the ORR[52,53-54], measuring kinetic isotope effect (KIE) is a promising strategy to experimentally uncover insights into its rate determining step. As written in Equation 2-1, the KIE for the ORR is defined as the ratio of the reaction rate constant when protons are available to the reaction rate constant when deuterium ions are available instead:

$$Kinetic\ Isotope\ Effect\ (KIE) = \frac{k_f^H}{k_f^D} \qquad [2\text{-}1]$$

A deuterium ion has essentially twice the mass of a proton, as it is a proton with an added neutron. Such significant increase in mass due to an isotope substitution cannot occur with heavier chemical species, so reactions involving protons are particularly well-suited for investigations with the KIE. The isotope substitution changes the reduced mass of the species involved in a bond-breaking or bond-forming event. Hence, if a reaction rate depends on the transfer of a proton, its substitution

with a deuterium ion will lower the rate constant.[55] The maximum kinetic isotope effect for a substitution of deuterium ions for protons is theoretically predicted to be 6.5 to 7, based on the stretching vibration of a chemical bond being replaced with a translational degree of freedom (a completely broken bond) at the transition state[56]. Therefore, two possible results will be informative in this KIE study of the ORR: a rate constant ratio appreciably greater than unity with respect to the theoretical limit indicates the rate under experimental conditions depends on a proton transfer, and a rate constant ratio insufficiently distinct from unity indicates that the rate determining step does not involve a proton transfer. When the rate determining step is proton dependent (a KIE is observed) it is either a (i) primary KIE, which ranges from 2 – 7, and involves the complete cleaving of the substituted specie bond, as mentioned above or a (ii) secondary KIE, *i.e.* $1 < KIE < 2$, which is induced by a modification of the rate determining step when shifting from $H_2O$-based to $D_2O$ based electrolyte, but which does not involve the breaking of the O-D/O-H bond [57].

In the first study of a KIE for the ORR on platinum catalysts, Ghoneim and Yeager carried out the reaction in a phosphoric acid electrolyte (phosphoric acid being known to poison Pt-based surfaces). They compared the reduction currents at a kinetically limiting potential regime and calculated a KIE sufficiently close to unity to conclude that the rate determining step did not include a proton transfer.[58] Since then, a growing interest in non-precious metal ORR catalysts to lower the costs of the electrocatalyst[59] has led to recent KIE studies of the ORR on different catalyst surfaces. A similar method to Yeager's was recently used to measure an appreciable kinetic isotope effect for the ORR on Fe-N/C catalysts in both acidic and alkaline conditions.[60] Sakaushi *et al.* similarly measured an appreciable KIE in acidic conditions and a KIE of unity in alkaline conditions for nitridated carbon (NC) catalysts.[61] Another recent study included both

platinum and non-platinum group catalysts and calculated KIE using the Koutecky-Levich equation with reduction currents limited by mass transport rather than a kinetic model at potentials approaching the standard reduction potential.[62] A KIE of approximately unity was reported for the ORR on platinum in a sulfuric acid electrolyte by this method, however, no measurements as of now have been conducted in perchloric, which poisons Pt to a much lower extent. Indeed, if several reports are underlining the perchloric specific adsorption on platinum surfaces [63,64,65], the latter impacts the Pt ORR activity to a much lower extent than $SO_4^{2-}$ [66].

This chapter aims to thoroughly establish the KIE of the ORR for the technologically relevant conditions of a platinum electrocatalyst in acidic electrolyte. Building upon previous studies of KIE for this reaction on platinum, this work includes calculations of the rate constant ratio from measurements in both potential regimes where the reaction is limited by mass transport of reacting species and where the reaction is kinetically limited approaching the standard reduction potential. Additionally, the KIE was measured in sulfuric acid as well as in perchloric acid, which unlike sulfuric acid, includes anionic species that only weakly poison platinum active sites.[67] The aim of this chapter is to provide mechanistic insights into the role of protons in the rate determining step of the ORR on state-of-the-art, Pt/C electrocatalysts. Rigorous experimental methods, well established in the literature [68,69,70,71], were followed, to create platinum catalyst ink, dry uniform and reproducible catalyst films on a millimeter-diameter scale working electrode, and perform careful electrochemical characterization of catalyst and ORR in a three electrode setup.

## 2.2 Experimental Methods

### 2.2.1 Three-electrode Setup

Figure 2-1 provides a representation of the electrochemical cell glassware, relevant accessories, and the three-electrode setup for electrochemical measurements. The glassware is custom-made for the purposes of these experiments by Adams & Chittenden. The three-electrode setup was connected to a Gamry potentiostat (1010E) to control potential at the working electrode and measure current. Potentials in this work are reported versus the reversible hydrogen reference electrode (RHE). However, measurement of potential is done experimentally with a mercury-mercurous sulfate reference electrode (MSE) (Pine Instruments) which is readily available and resilient to acidic environments; potentials are then adjusted to RHE for reporting data.

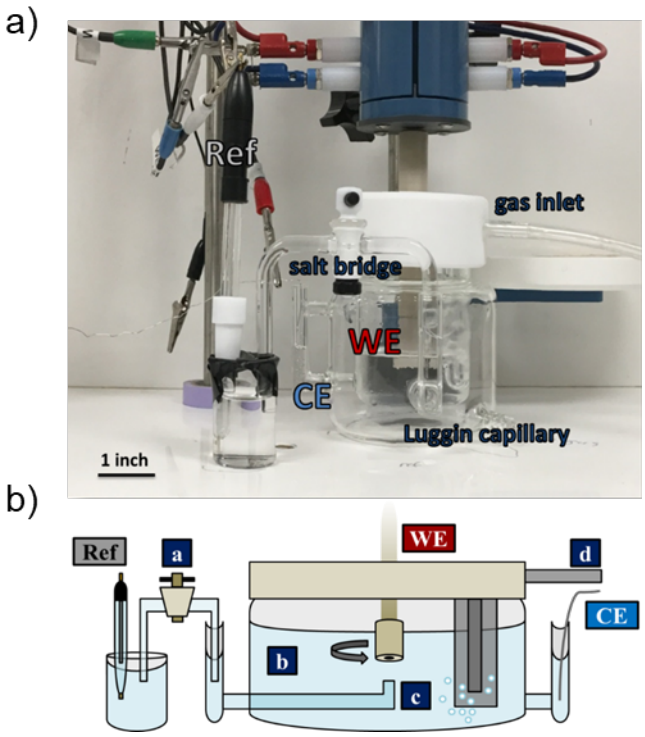


Figure 2-1 The schematic of the electrochemical cell set up: *Ref* is the reference electrode, *WE* is the working electrode, *CE* is the counter electrode, *a* is the salt bridge, *b* is the electrolyte, *c* is the Luggin capillary, and *d* is the inlet for gas.

The glassware was soaked in concentrated acid (Caro's acid, *i.e.* a solution of concentrated $H_2SO_4$ and $H_2O_2$ with equivalent volumes) before each experiment. The glassware and non-glass parts of the electrochemical cell were then thoroughly cleaned with MilliQ water (18.2 MΩ) and boiled to remove the adsorbed $H_2SO_4$. The electrocatalyst inks were prepared aiming at a 30 μg $cm^{-2}_{geo}$ Pt loading (on a 5 mm diameter working electrode), this being consistent with the literature [72]. The platinum electrocatalyst (Pt/C) used in this work was a HiSPEC 4000 (FuelCellStore), 40 wt. % on Vulcan XC72R. 2.3 mg of the active material was mixed with 1.507 mL of MilliQ H2O:IPA (24 wt. % IPA) and 37 μL of a 5 wt. % Nafion® solution (Chemours D521 Nafion dispersion). To promote uniform distribution of catalyst, the resulting ink was briefly mixed with a benchtop vortexer then moved to a bath ultrasonicator, for 60 to 90 minutes. The ultrasonic bath temperature was maintained at $T < 40$°C to preserve the Nafion® structure. After ultrasonication, the ink was mixed with a high-shear mixer at 8000 rpm for 1 min to disrupt any remaining agglomerates. The ink was stored on a stir plate and continuously mixed with a magnetic stir bar and ultrasonicated 30 minutes before depositing a catalyst film from the ink. A 10 μL ink aliquot was deposited on the electrode rotating at 100 rpm. The rotation was then gradually increased to 700 rpm and the aliquot was dried while rotating, at room temperature. Platinum polycrystalline disk (Pt-poly) was also used in this study. The preparation of the Pt-poly was as follow: (i) mechanical polishing with polishing paper (2,000 and 3,000 grit); (ii) mechanical polishing with alumina suspension (5 μm, 0.3 μm and 0.05 μm); (iii) cleaning of the Pt-poly for $t = 5$ min in 3 successive solutions, *i.e.* acetone, ethanol and MilliQ $H_2O$; (iv) cleaning for *ca.* 30 min in Caro's acid. Since the quality of a catalyst film is determined by the uniformity of its surface with respect to platinum distribution, the glassy carbon electrode used for the Pt/C characterization was also polished using 0.05 μm

alumina powder (or 5 µm, 0.3 µm and then 0.05 µm, depending of the surface condition), followed by cleaning with successive solutions. The electrochemical characterization was performed on a Gamry potentiostat (1010E interface) for poly-Pt, using the surface mode, and for commercial Pt/C. The reference electrode was mercurous-mercury sulfate electrode (MSE, Pine Instrument) and was connected to the main body of the cell by a salt bridge, to avoid any contamination. All the potentials in this work are reported *vs.* the reference hydrogen electrode, RHE. The counter electrode was a platinum wire. The experiments were performed in four different configurations presented in Table 2-1.

Table 2-1 Different experimental cases studied throughout this chapter.

| | **Perchloric** | **Sulfuric** |
|---|---|---|
| **Proteo** | $H_2O$ + 0.1 M $HClO_4$ (65 – 71 wt.%, OmniTrace Ultra™, Sigma Aldrich) | $H_2O$ + 0.05 M $H_2SO_4$ (VWR, Omitrace®) |
| **Deutero** | $D_2O$ (99.9 atom % D, Sigma-Aldrich) + 0.1 M $DClO_4$ (68 wt. %, Sigma-Aldrich) | $D_2O$ (99.9 atom % D, Sigma-Aldrich) + 0.05 M $D_2SO_4$ (96-98 wt. %, Sigma-Aldrich) |

Electrochemical characterizations were performed as follow: (i) the cell was purged with ultra-high purity (UHP) $N_2$ for 25 min; (ii) activation cyclic voltammetries (CVs) were performed between 0.00 V *vs.* RHE and 1.23 V *vs*. RHE at 500 mV $s^{-1}$ for 100 cycles; (iii) 5 cycles were recorded in the same potential range, at 20 mV $s^{-1}$; (iv) a linear sweep voltammetry (LSV) between 0.10 and 1.00 V *vs.* RHE was recorded at 20 mV $s^{-1}$ and 1600 rpm, for background correction-current which occurs in the system that is not a result of the oxygen reduction reaction, along with an electrochemical impedance spectrograph in potentiostatic mode to assess the ohmic losses (at 0.40 V vs. RHE, from 1 MHz and 1 Hz); (v) the cell was saturated in UHP $O_2$ for 25 min; (vi)

LSVs at the same scan rate and in the same potential range than (iv) were performed at 900, 1600 and 2500 rpm. The transmission electron microscopy (TEM) micrographs were obtained using JEOL 2800 TEM operated at an accelerating voltage of 200kV.

## 2.3 Results

### 2.3.1 Electrochemical Characterization by Cyclic and Linear Sweep Voltammetries

Transmission electron microscopy (TEM) images of the electrocatalyst are provided in Figure 2-2. The TEM images show well-dispersed Pt electrocatalyst on carbon-black support. The quality of the catalyst films was assessed by comparing electrochemical surface area (ECSA) and half-wave potential. For each case from Table 2-1, three independent measurements were performed.

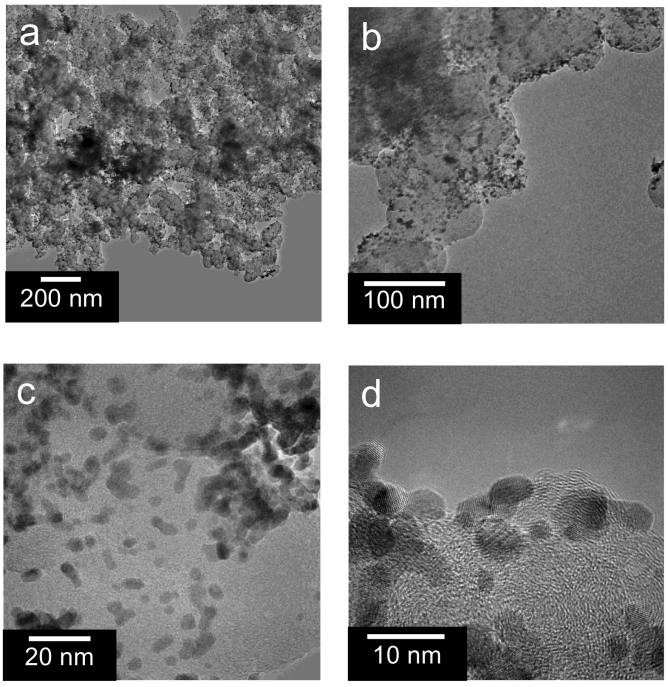


Figure 2-2 Transmission electron microscopy images of the HiSPEC 4000 Pt/C electrocatalysts at different magnifications.

Equation 2-2 provides the calculation of the electrochemical surface area (ECSA) of Pt, where $Q_{H\text{-}adsorption}$ is the charge of the adsorption of protons (or deuterium ions) on the catalytic surface of the working electrode measured by CV. [68] This value is calculated as the integral of the reduction currents below 0.4 V *vs.* RHE and before the hydrogen evolution reaction approaching 0 V *vs.* RHE divided by sweep rate. The constant in the denominator of Equation 2-2 is the charge of monolayer adsorption of protons to a surface of polycrystalline platinum, used as a conversion factor from charge to area.[73] The mass of platinum loaded on the working electrode is expressed as $m_{Pt}$. The slight differences in $H_{upd}$ observed when switching from $H_2O$- to $D_2O$-based electrolyte might be induced by a combination of two phenomena arising from: (i) the catalyst deposit and (ii) the intrinsic differences between deuterium and proton adsorption on Pt surfaces. Due to the non-uniform particle size distribution of the commercial Pt/C, slight differences in electrochemically active surface and relative abundance of platinum crystalline planes are to be observed in between the different ink deposits at the working electrode. In a similar fashion, the poly-Pt annealing, mandatory to achieve a clean Pt surface, induces slight restructuration of the latter and thus, changes in the $H_{upd}$. Furthermore, the differences in the free energy of adsorption of the deuterium *vs.* the protons on Pt might contribute to those changes in $H_{upd}$ [74].

$$ECSA_{Pt}(m^2 g_{Pt}^{-1}) = \left[\frac{Q_{H-adsorption}(C)}{210\ \mu C\ cm_{Pt}^{-2} * m_{Pt}(mg)}\right] * 10^5 \qquad [2\text{-}2]$$

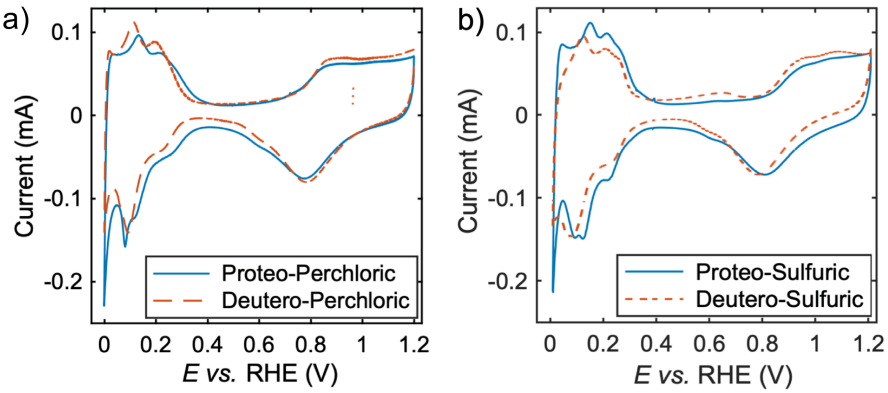


Figure 2-3 Cyclic voltammetry for commercial Pt/C (HiSPEC 4000) in $N_2$-saturated electrolyte at scan rate of 20 mV $s^{-1}$ a) $H_2O$ + 0.1 M $HClO_4$ or $D_2O$ + 0.1 M $DClO_4$; b) $H_2O$ + 0.1 M $H_2SO_4$ or $D_2O$ + 0.1 M $D_2SO_4$.

The ECSA was measured in the different electrocatalysts and is of *ca.* 80 $m^2$ $g_{Pt}^{-1}$ (see Figure 2-4a, which corresponds to the values reported in the literature. No trend between ECSA and electrolyte was observed. Therefore, the films represented by this dataset are comparable for the purposes of this mechanistic investigation.

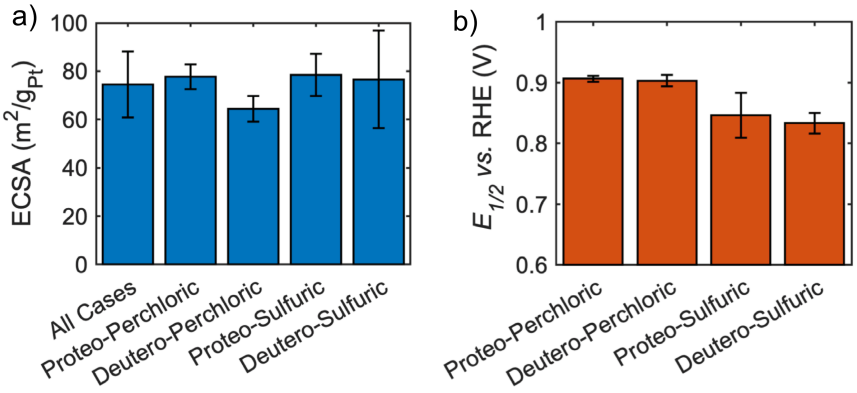


Figure 2-4 a) Platinum electrochemical surface area (ECSA) calculated from the hydrogen desorption peak for the different electrolytes ($N_2$-saturated) investigated in this work, on commercial Pt/C (HiSPEC 4000); b) half-wave potentials ($E_{1/2}$) calculated for the different

electrolytes investigated in this work ($O_2$-saturated), on commercial Pt/C (HiSPEC 4000), at 20 mV $s^{-1}$ and 1600 rpm.

Half-wave potentials ($E_{1/2}$ *vs.* RHE, in V) were provided from the linear sweep voltammetry in oxygen saturated electrolyte. Polarization curves obtained in $O_2$-saturated electrolyte from all four experimental cases are shown in Figure 2-5. Figure 2-4b shows $E_{1/2}$ values for the catalyst films used in this study. Irrespective of the difference between proteo and deutero electrolytes, perchloric electrolytes present consistent half-wave potential measurements of *ca.* 0.9 V *vs.* RHE and sulfuric electrolytes present measurements of *ca.* 0.85 V *vs.* RHE. The consistently lower $E_{1/2}$ for the sulfuric cases compared to the perchloric cases is expected, since sulfonate anions poison the active sites of the platinum catalyst to a much larger extent that perchlorate anions.[68] Therefore, investigating the KIE both in sulfuric acid, and perchloric acid is extremely relevant as it provides information on the ORR mechanism under different contributions from the electrolytes anions.

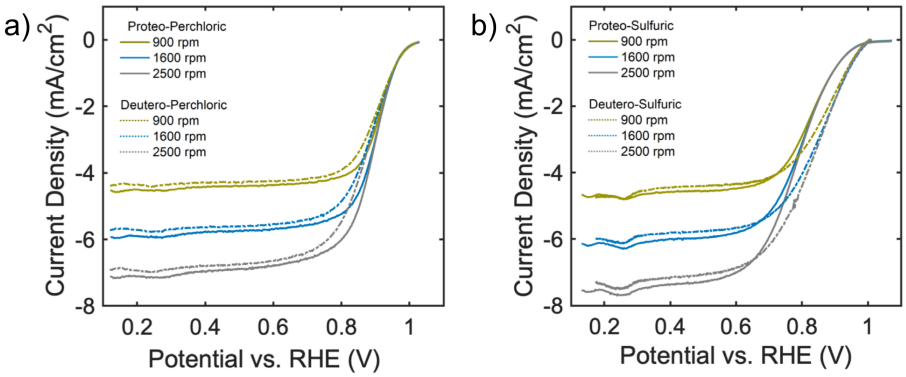


Figure 2-5 Cyclic voltammetry for commercial Pt/C (HiSPEC 4000) in $O_2$-saturated electrolyte at Scan rate, 20 mV $s^{-1}$, rotation speed 900 – 2500 rpm a) $H_2O$ + 0.1 M $HClO_4$ or $D_2O$ + 0.1 M $DClO_4$; b) $H_2O$ + 0.1 M $HClO_4$ or $D_2O$ + 0.1 M $DClO_4$.

### 2.3.2 Kinetic Isotope Effect from Koutecky-Levich and Tafel Analysis

A linear sweep voltammetry plot characterizing the ORR in oxygen saturated electrolyte, as in Figure 2-5, shows that the reaction proceeds between two limiting extremes, a mass transport limitation when reaction kinetics are favorable at the applied potential, *i.e.* at *E vs.* RHE < 0.7 V and a kinetic limitation, at 0.75 – 0.8 V < *E vs.* RHE < onset potential. The simplest form of the Koutecky-Levich equation, written as Equation 2-3, separates the contributions of kinetic limited current density ($j_k$) and mass transport limited current density ($j_{mt}$) to the total measured current density ($j$).[75]

$$\frac{1}{j} = \frac{1}{j_k} + \frac{1}{j_{mt}} \qquad [2\text{-}3]$$

At the surface of a rotating disk electrode, the mass transport can be defined according to Equation 2-4 [75]:

$$\frac{1}{j} = \frac{1}{j_k} + \left(\frac{1}{0.620nFAD^{2/3}\nu^{-1/6}C}\right)\omega^{-1/2} \qquad [2\text{-}4]$$

where, $n$ is the number of electrons transferred in reaction, $F$ is Faraday's constant, $A$ is the electrode area, $D$ is the diffusivity of oxygen in the electrolyte, $\nu$ is the kinematic viscosity, $C$ is the concentration of oxygen in the electrolyte, and $\omega$ is the rotation rate in radians per second. From this equation, it appears that a plot of reciprocal current density *vs.* inverse square root of rotation rate has the reciprocal kinetic current as the y-intercept. The reaction rate constant, and thus kinetic isotope effect, are calculated with Equations 2-5a and 2-5b respectively. The term

$C_{O_2}^*$ represents concentration of oxygen when the electrolyte is saturated, which is lower for a heavy water-based electrolyte ($C_{O_2}^D$) than for the proteo cases ($C_{O_2}^H$), by a factor of 0.908. [76]

$$j_k = nFk_f C_{O_2}^* \quad [2\text{-}5a]$$

$$KIE = \frac{k_f^H}{k_f^D} = \frac{n^D F j_k^H C_{O2}^D}{n^H F j_k^D C_{O2}^H} = \frac{j_k^H}{j_k^D} \cdot \frac{1}{0.908} \quad [2\text{-}5b]$$

To calculate KIE using the Koutecky-Levich equation in this study, current densities are taken in the mass transport limited regime of linear sweep voltammetry plots in oxygen saturated electrolyte (at 0.425 V *vs.* RHE) at 900, 1600, and 2500 rpm for each catalyst film. Each film measured for the proteo case is compared with each film measured for the deutero case for each type of acid (sulfuric and perchloric), thus allowing to assess the presence, or absence, of a KIE at *E vs.* RHE = 0.425 V. Figure 2-6 shows the Koutecky-Levich plots for each type of electrolyte.

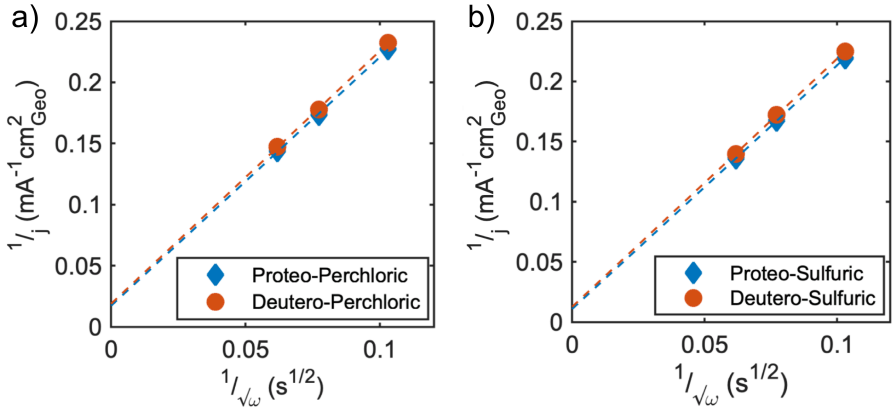


Figure 2-6 Koutecky-Levich plots for the different electrolytes investigated in this work, on commercial Pt/C (HiSPEC 4000).

The KIE calculation was also carried out using the Tafel analysis, which provides information on the KIE in the 0.75 – 0.8 V < *E vs.* RHE < onset potential region. Using Tafel plots to calculate KIE requires the Tafel approximation to the Butler-Volmer kinetic model for electrochemical reactions.[75] A form of the Tafel equation is given as:

$$\eta = \frac{2.303RT}{\alpha n_\alpha F} log\, j_0 - \frac{2.303RT}{\alpha n_\alpha F} log\, j_k \quad [2\text{-}6]$$

where $\eta$ is overpotential (the difference between potential and the standard reduction potential), $j_k$ the kinetic current density (calculated using Equation 2-6), $j_0$ the exchange current density (current at zero overpotential), $\alpha$ is a symmetry coefficient, $R$ is the gas constant, and $T$ is temperature. To accurately represent the ORR in proteo and deutero cases, it is necessary to consider that the standard reduction potential is different in heavy water as compared to the proteo case, arising from the different Gibbs free energies of formation for $H_2O$ and $D_2O$. Accounting for this discrepancy, $E^0_{deutero}\ vs. RHE = 1.26$ V while $E^0_{proteo}\ vs. RHE = 1.23$ V.[60,77] The Tafel equation can be rearranged into a linear form useful for constructing Tafel plots of $log\, j_k$ vs. overpotential, shown by Equation 2-7a. The y-intercept of these plots is $log\, j_0$, and exchange current density is directly related to the rate constant, so Equation 2-7b gives the kinetic isotope effect similarly to Equation 2-5b.

$$log\, j_k = -\frac{\alpha n_\alpha F}{2.303RT}\eta + log\, j_0 \quad [2\text{-}7a]$$

$$KIE = \frac{j_o^H}{j_o^D} \cdot \frac{C_{O2}^D}{C_{O2}^H} = \frac{j_o^H}{j_o^D} \cdot \frac{1}{0.908} \quad [2\text{-}7b]$$

However, there is significant error inherent in extrapolating to zero overpotential, induced by the fact that the extrapolation is performed over several decades of current and *ca.* 200 – 300 mV in potentials. Therefore, instead of assessing the KIE based on such large extrapolation, we calculated the KIE by comparing the kinetic current at the onset potential, defined as the potential were the current reaches 2% of the mass transport limited current (named onset current, $j_1$). Equation 2-8 is therefore used to calculate KIE from the Tafel plots.

$$KIE = \frac{j_1^H}{j_1^D} \cdot \frac{C_{O2}^D}{C_{O2}^H} = \frac{j_1^H}{j_1^D} \cdot \frac{1}{0.908} \qquad [2\text{-}8]$$

Figure 2-7 shows examples of the Tafel fits used to calculate the onset current and, thus, the KIE for the different electrolytes studied in this work. It is reasonable that the onset currents are observed at slightly different overpotentials for the proteo and deutero cases due to the discrepancy in standard reduction potential.

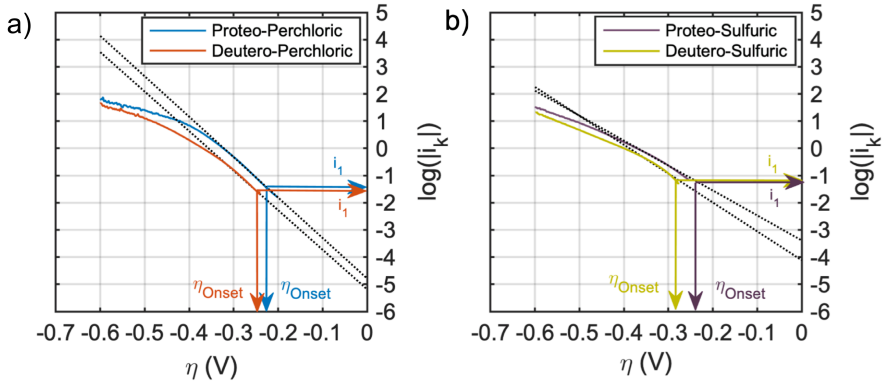


Figure 2-7 Tafel plots for the different electrolytes investigated in this chapter, on commercial Pt/C (HiSPEC 4000).

As summarized in Figure 2-8, KIEs of approximately unity were calculated for Pt/C (HiSPEC 4000) by the Koutecky-Levich equation, independently of the electrolyte, indicating that the rate determining step of the ORR does not include a proton transfer in the mass transport limited regime of the ORR. Similar findings were observed while using the Tafel method, thus confirming that, on the entire ORR potential range, the rate determining step is not proton-dependent. Additional experiments were carried out on the poly-Pt disk. Both Koutecky-Levich and Tafel analysis were used to evaluate KIE. Figures 2-9 to 2-12 show the raw and analyzed data for poly-Pt disk.

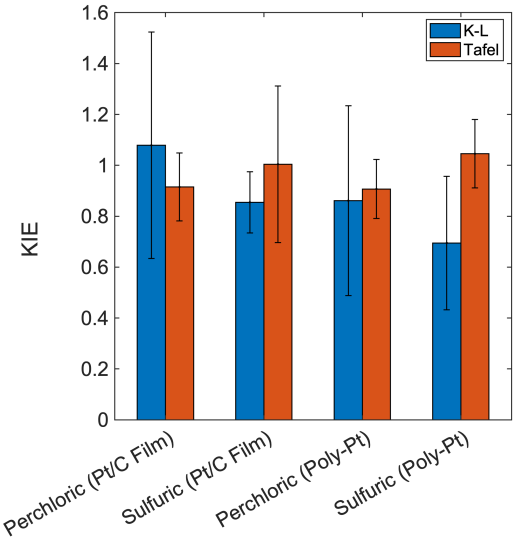


Figure 2-8 Comparison of KIE data obtained from Koutecky-Levich equation and Tafel plots in perchloric and sulfuric acid experimental cases for Pt/C catalyst film and Poly-Pt.

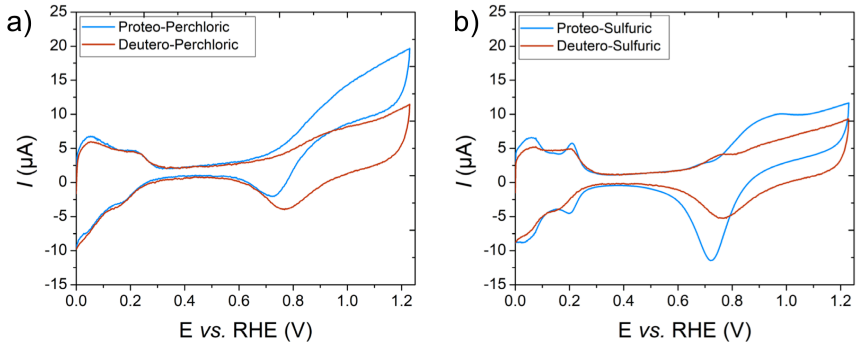


Figure 2-9 Cyclic voltammetry for poly-Pt in $N_2$-saturated electrolyte at scan rate of 20 mV $s^{-1}$ a) $H_2O$ + 0.1 M $HClO_4$ or $D_2O$ + 0.1 M $DClO_4$; b) $H_2O$ + 0.1 M $H_2SO_4$ or $D_2O$ + 0.1 M $D_2SO_4$.

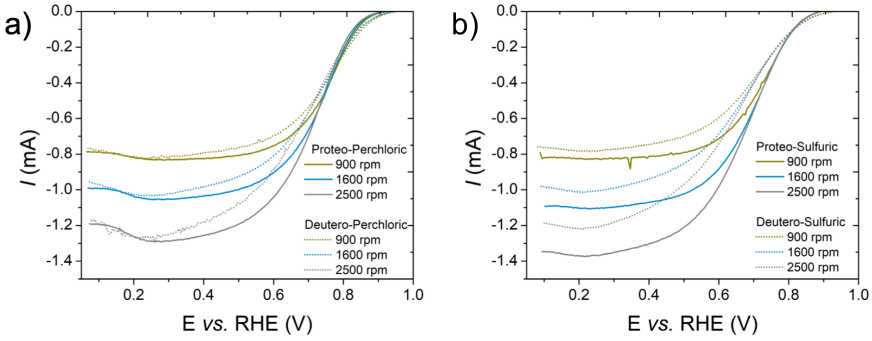


Figure 2-10 Cyclic voltammetry for poly-Pt in $O_2$-saturated electrolyte at 20 mV $s^{-1}$ scan rate, and rotation speed of 900 – 2500 rpm. a) $H_2O$ + 0.1 M $HClO_4$ or $D_2O$ + 0.1 M $DClO_4$; b) $H_2O$ + 0.1 M $HClO_4$ or $D_2O$ + 0.1 M $DClO_4$.

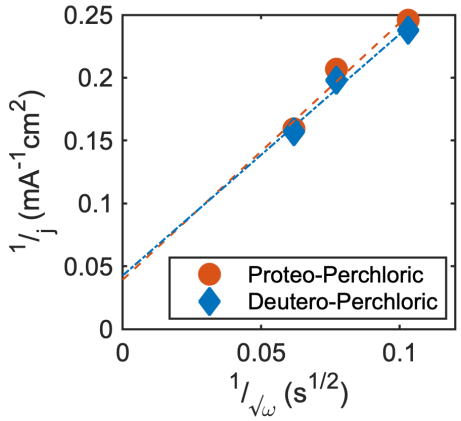


Figure 2-11 Example of Koutecky-Levich plots for poly-Pt (in perchloric-based electrolyte).

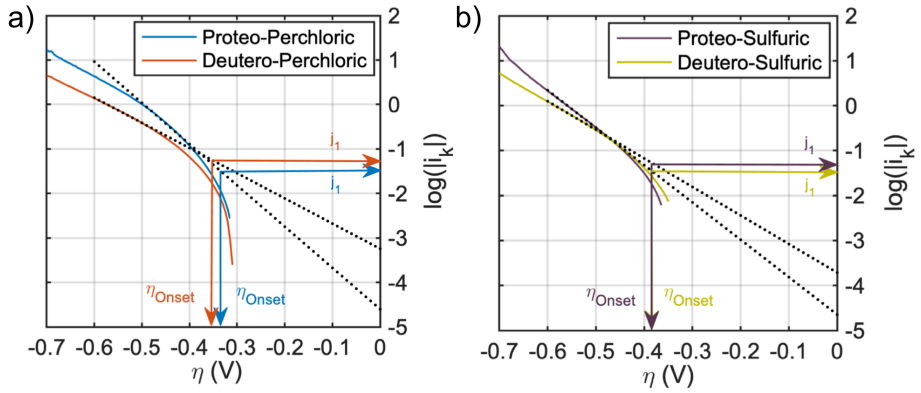


Figure 2-12 Tafel plots for the different electrolytes investigated in this work, on poly-Pt (HiSPEC 4000).

Figure 2-8 also summarizes the results of the KIE poly-Pt disk. Based on these observations, both high loading, commercial Pt/C electrocatalysts and Pt polycrystalline extended surface exhibit KIE of *ca.* 1, thus showing that protons do not participate in the rate-determining step of the ORR.

## 3.3. Summary

Kinetic isotope effect (KIE) is the ratio of kinetic currents measured in electrolyte with protons *vs.* that with deuterium ions. The ratio of *ca.* 1 indicates that protons do not participate in the reaction rate determining step. In this study, the KIE was applied to study oxygen reduction reaction (ORR) on 40 wt% Pt/C (HiSPEC 4000) and poly-Pt disc. KIE was calculated using (i) the Koutecky-Levich equation, which incorporates a hydrodynamic model for a rotating disk electrode and uses currents measured in the mass transport limited potential regime of the ORR and (ii) Tafel approximation to Butler-Volmer equation extrapolated to low-magnitude overpotentials where the reaction is kinetically limited. In all cases, the values were showed to be approximately 1. The calculated KIE are similar in perchloric and sulfuric acids. Although sulfonate anions poisoning of the platinum catalyst is far more important (as evidenced by the shift in half-wave potential

from perchloric to sulfuric based electrolytes), this effect is consistent for the proteo-sulfuric and deutero-sulfuric cases and should therefore not impact the ratio that determines KIE. A KIE of unity indicates that the rate determining step of the ORR reaction does not include a proton transfer. As the ORR rate determining step is known to be, on Pt surfaces and nanostructure, the $O_2 + H^+ + e^- \rightarrow OOH_{ads}$ step, it indicates that the limiting elementary step should either be the oxygen adsorption ($O_2 \rightarrow O_{2,ads}$) or an electron transfer without a coupled proton transfer ($O_{2,ads} + e^- \rightarrow O_{2,ads}^-$). The result is in agreement with previous studies of ORR kinetic isotope effect on platinum, such as Yeager's original work in phosphoric acid[58] and Gewirth's group more recent work.[62] While the kinetic isotope effect under these specific conditions is defined, future work will investigate low platinum loading electrocatalysts, where inter-particle spacing, and support interactions can be relevant.

# Chapter 3

# Ionic Liquids in Polymer Electrolyte Fuel Cells: New State-of-the-art in the Oxygen Reduction Reactivity and Durability

## 3.1 Introduction

Various strategies exist to develop high-performing cathode CLs including nitrogen-functionalized supports [78,79,80,81,82] and modification of electrocatalysts with promising additives to enhance the catalytic activity [83,84,85,86] emerged as a key approach [87,88]. In this way, catalyst layers with ultra-low Pt loadings can be designed without relinquishing the long-term durability as cost and durability are the two major barriers for commercialization of fuel cell electric vehicles.

It has been shown that the carbon support on which the Pt nanoparticles are dispersed plays a role on both stability and performance of the catalyst layer by affecting the porosity, corrosion rate, and mass transport properties[89]. High surface area carbon support is considered to be a great candidate for fuel cell application owing to its high internal mesoporosity. It can host up to 75% of Pt active surface area within the wide mesopores with size between 5.5 and 14 nm. Pt nanoparticles present in the internal pores are not in contact with ionomer, reducing ionomer's sulfonate groups adsorption that generally impedes Pt's kinetic activity [21,22]. Although HSA Pt-based catalysts have substantial ORR activity, they tend to show high proton resistance within the catalyst layer's ionic network. This along with high oxygen mass transport resistance contribute to significant voltage loss, specifically at high current densities, where local transport restriction

become more pronounced and more protons and oxygen are required to drive the ORR reaction [90,20]. Because the ionomer cannot penetrate the micropores and smaller mesopores of HSA carbon supports due to size-exclusion[91], liquid water is responsible for proton transport to Pt reaction sites [92]. However, water's ionic conductivity is orders of magnitude smaller than ionomer and even in confined environments it is two orders of magnitude smaller than that of Nafion[93]. Therefore, filling the micropores and smaller mesopores with ionic liquids (ILs) with high ionic strength in a range between (2.77-5.3×$10^3$) mol $m^{-3}$ is an effective approach to provide sufficient proton delivery to the Pt active sites within the pores (Figure 3-1 (a)) [29,94]. ILs within the micropores and smaller mesopores induce local nanoconfinement that can promote ORR because: *i)* Knudsen diffusion of oxygen taking place in the nanopores increases the frequency of oxygen molecules collision with the catalyst surface sites rather than molecule-to-molecule collision, *ii)* electric double layers are thin for ILs|Pt interface compared to water|Pt interface[94]. At potentials above 0.23 V, Pt is positively charged and will expel protons from the micropores and mesopores if in contact with water because double layers are thick. However, when Pt is in contact with ILs, the ionic strength of ILs is high and therefore the double layers will be thin and thus electric field will be shielded within <0.5 nm from the surface of Pt and protons will not be impacted by positively charged Pt[94,95,96].

Various research groups have incorporated IL small molecules or IL-containing ionomers into the cathode catalyst layers and showed improved catalytic activity toward ORR. These studies will be discussed in the background section (3.2) which was most often attributed solely to higher oxygen solubility and suppressed adsorption of nonreactive oxygenated species. Recently, Huang et al.[97] and Yan et al.[98] indicated that sufficient proton conductivity in the catalyst layer can be responsible for facilitated ORR kinetics. They also have shown that increased solubility of oxygen in ILs

domains is compensated by poor diffusivity, as it is the product of these two that guides oxygen transport. However, they only relied on rotating disk electrode (RDE) studies to prove their hypothesis without translating it into membrane electrode assembly (MEA) fabrication and practical testing in fuel cell hardware.

In this chapter, we investigate in-depth electrochemical and physical properties of ILs integrated into HSA Pt/C catalyst and integrate these catalysts into MEAs to observe their behavior under fuel cell operation. Alkyl imidazolium bis-(trifluoromethanolsulfonyl)imide ILs have been chosen for this study because they met the criteria of suitable modifier for fuel cell catalyst design due to their high ionic conductivity and oxygen solubility, superior thermal and electrochemical stability under fuel cell tested temperature and voltage, low melting point, viscosity, and vapor pressure. They are also non-flammable and have high $\Delta pK_a$ value which is shown to be sufficient for satisfactory proton transfer [94,99,100,101]. The development of this criteria will be further discussed in section 3.3. Catalytic activity metrics, mass and specific activities of Pt/C-IL systems with optimized amount of IL were first pre-screened by RDE setup. Electrochemical impedance spectroscopy (EIS) was implemented to measure overall effective proton diffusion resistance ($R_{H^+}$) within IL-containing catalyst layer[97]. Then, MEAs with optimized ink recipes were fabricated and rigorously tested within PEFC hardware. The extensive *in-situ* metrics including MA, SA, ECSA, $H_2$/air polarization curves, ionic conductivity determined by EIS, oxygen mass transport resistance, and CO displacement provided an insight into the effect of IL on the cell performance under harsh testing conditions. *Ex-situ* characterizations such as TEM, X-ray photoelectron spectroscopy (XPS), nitrogen physisorption, zeta potential and water uptake measurements were also performed to determine the physiochemical properties, microstructure of the catalyst layer, understanding the fundamental interaction between IL molecules and Pt surface, as well as the

underlying mechanism for performance improvement. Finally, the durability of the cells was assessed by accelerated stress tests (ASTs) including potential cycling between two potentials to induce accelerated degradation of the catalyst layer[102]. These characterizations brought the understanding of a new method of catalyst layer integration with ILs in which not only the loading of Pt can be decreased without exacerbating degradation, but also an improved ORR activity can be bundled with a superior durability.

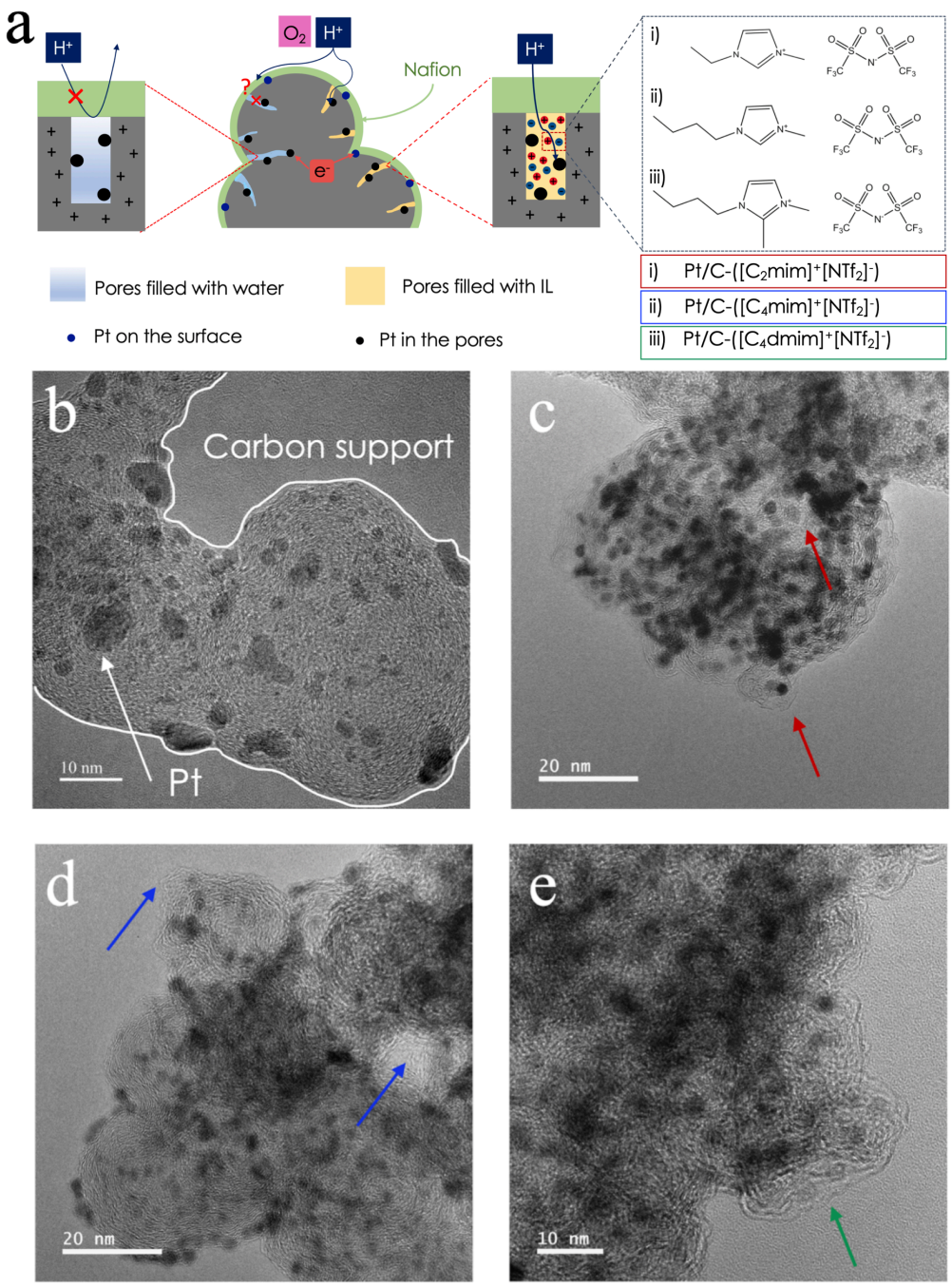


Figure 3-1. a) Schematic of HSA Pt/C catalysts with micropores filled with either water or imidazolium-derived ILs, TEM images of b) pristine 40 wt.% HSA Ketjenblack Pt/C obtained from Fuel Cell Store, c) Pt/C-($[C_2mim]^+[NTf_2]^-$), d) Pt/C-($[C_4mim]^+[NTf_2]^-$), e) Pt/C-($[C_4dmim]^+[NTf_2]^-$). Arrows show the ionic liquids.

## 3.2 Background

This section summarizes prior published key papers on Pt electrocatalyst interface design for fuel cell application. In these studies, different LSA and HSA Pt/C electrocatalysts with various loading of Pt are modified with ILs and other small molecules. Then, the effect of these modifications on electrochemical activity was characterized by various electrochemical techniques including CV, LSV, EIS. A detailed explanation of the techniques is provided in the experimental section of this proposal.

Zhang et al.[103] developed solid catalyst with ionic liquid layer (SCILL) by synthesis of IL-modified Pt/C samples with different ILs including [MTBD][$NTf_2$]. They used commercial LSA 20 wt.% Pt/C catalyst and studied the performance in the half-cell electrolyte set up. They also studied the effect of pore-filling degree and IL layer thickness on the ORR performance of Pt/C-[MTBD][$NTf_2$] system. As summarized in Figure 3-2 and Figure 3-3, there is a slight suppression and negative shift to lower potentials in the $H_{UPD}$ peak in Pt/C-SCILL systems compared to pristine Pt/C. They suggested that the suppression in $H_{UPD}$ is due to the selective occupation of Pt active sites by some IL molecules, and weakening of the Pt−H bonding strength through a ligand effect. Therefore, with only 2% of IL pore filling degree (α), the electrochemical surface area (ECSA) decreased from 99.1 to 87.5 $m^2\ g_{Pt}^{-1}$. Further addition of IL (α >10%), did not change the ECSA noticeably (Figure 3-2 (b)). It is also shown that the surface oxidation of Pt is suppressed by IL molecules preserving the active sites from non-reactive oxygenated species ($OH_{ad}$).

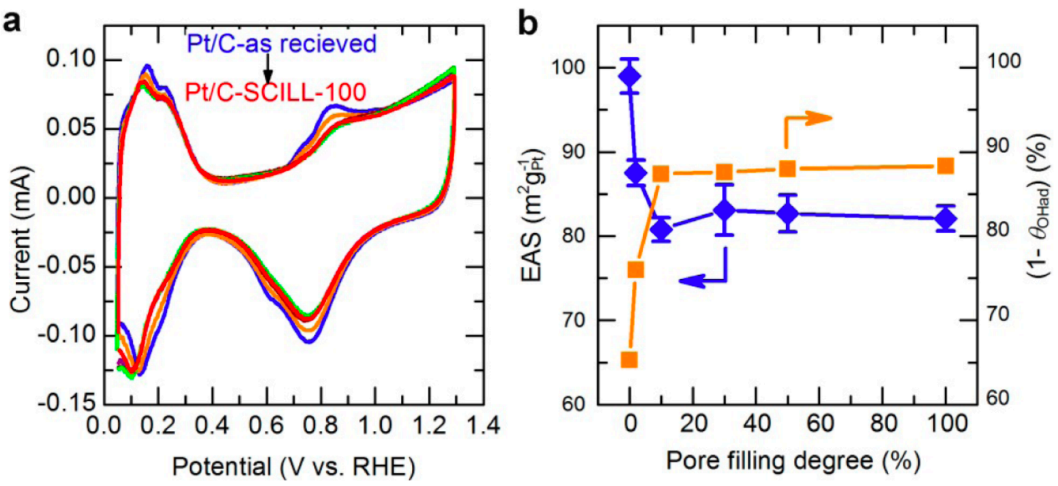


Figure 3-2 Electrochemical characterization: a) Cyclic voltammetry curves of Pt/C-[MTBD][$NTf_2$] systems in $N_2$-saturated 0.1 M $HClO_4$ solution at a scanning rate of 20 mV $s^{-1}$. b) ECSA (blue) and free Pt sites (1-$\theta_{OHad}$) @0.9 V (orange) as a function of the pore filling degrees for Pt/C-SCILL materials[103].

Polarization curves in Figure 3-3 (a) illustrated that the half-wave potential increased to higher potential with IL pore filling degree accelerating ORR kinetics. Zhang et al. proposed that the improvement is due to the lower $\theta_{OH\text{-}ad}$ and higher oxygen concentration. Specific activity at 0.9 V shows a volcano-shape dependence on α, indicating that at low α-values, a certain percentage of Pt surface is not in contact with $O_2$-enriched layer of IL and the ORR kinetics is not fully boosted. However, a high α-value leads to the formation of a thick IL layer that limits the $O_2$ mass transport from the electrolyte to Pt active sites. Therefore, an optimal SCILL system with an α-value of 50 combines an increased $O_2$ availability by fully covered platinum particles, while not fully flooding the pores that limits the $O_2$ mass transport. The SCILL-50 showed a high mass activity of 0.56 A $mg_{Pt}^{-1}$ at 0.9 V, which is above the mass activity target set by the US Department of Energy for Pt electrocatalyst.

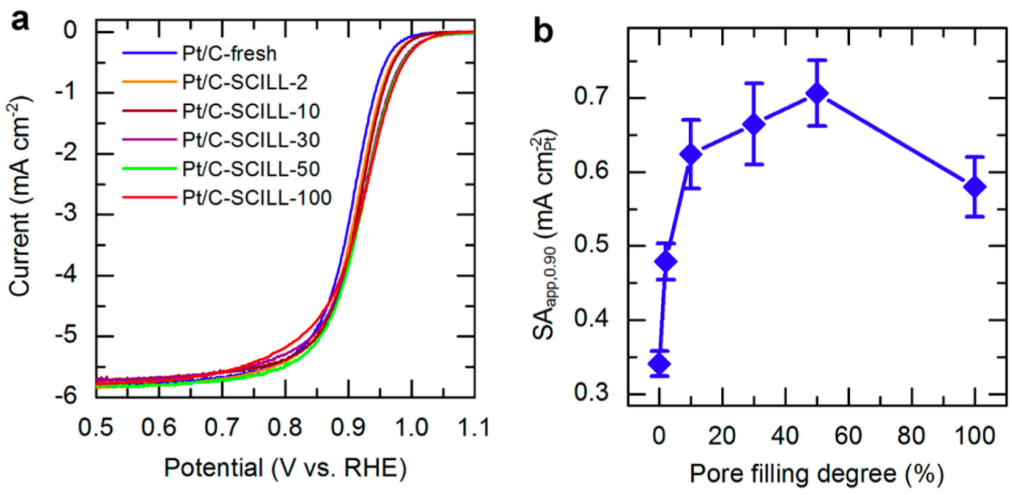


Figure 3-3 Oxygen reduction reaction on Pt/C and Pt/C-[MTBD][$NTf_2$] systems. a) ORR polarization curves of Pt/C-[MTBD][$NTf_2$] systems compared to commercial Pt/C recorded in $O_2$-saturated 0.1 M $HClO_4$ solution at a scanning rate of 10 mV $s^{-1}$. b) Correlation between the specific activity and the pore filling degree of the IL at 0.90 V[103].

In another study, Zhang et al.[104] modified LSA 20 wt.% Pt/C samples by 1-methyl-3-alkylimidazolium bis (trifluoromethanesulfonyl)imides ([$C_nC_1$im][$NTf_2$], n = 2−10) with various alkyl chain lengths in imidazolium cations and achieved final pore filling degree of 10 %. As summarized in Figure 3-4, 3-5, and 3-6, electrochemical properties, electrocatalytic activity, and CO-stripping behavior are dependent on the cationic chain length of the ILs. When the cationic chain length of ILs is elongated from $C_2$ to $C_4$, ECSA value stay comparable to that of the baseline Pt/C catalyst, and the specific activity increases. By elongation of the chain length from $C_6$ to $C_{10}$, the specific activity is improved; however, the ECSA and mass specific activity drop significantly. It can be seen from ORR polarization curves in Figure 3-5(a) that the $E_{1/2}$ is positively shifted for all the samples except for the Pt/C-[$C_{10}C_1$im][$NTf_2$] where the curve is negatively shifted to lower potential instead.

ILs with long alkyl chains (n>6), form a lipid-/micelle-like rigid bilayer structure due to the aggregation of their nonpolar cationic chain. This can lead to the repelling of the water molecules from Pt active sites protecting them from being oxidized; therefore, $\theta_{OHad}$ decreases. On the other hand, IL molecules can interact and block terrace sites of Pt, decreasing the catalytic activity toward ORR.

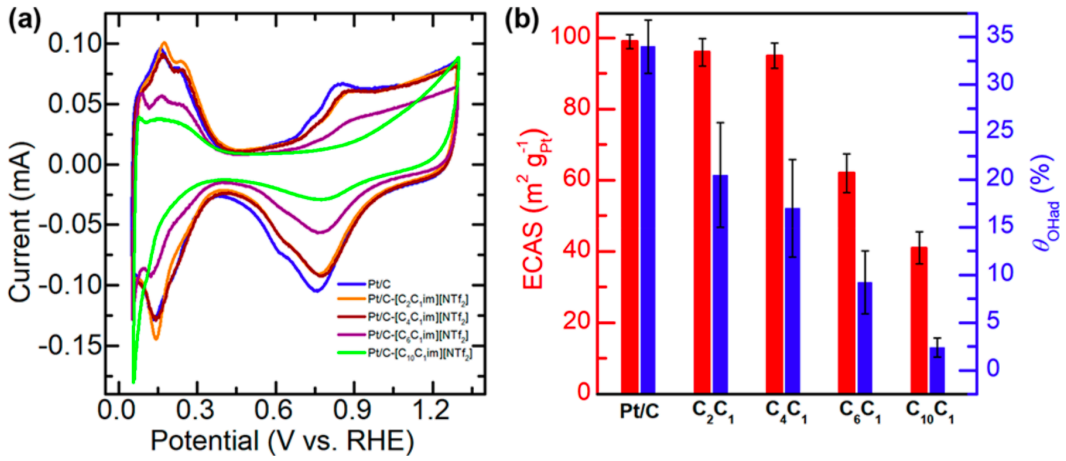


Figure 3-4 A) Cyclic voltammetry curves of IL-modified Pt/C catalysts recorded in $N_2$-saturated 0.1 M $HClO_4$ solution at a scan rate of 20 mV $s^{-1}$. b) ECSA $\theta_{OHad}$ calculated from CV curves on the Pt/C catalysts with and without IL modification[104].

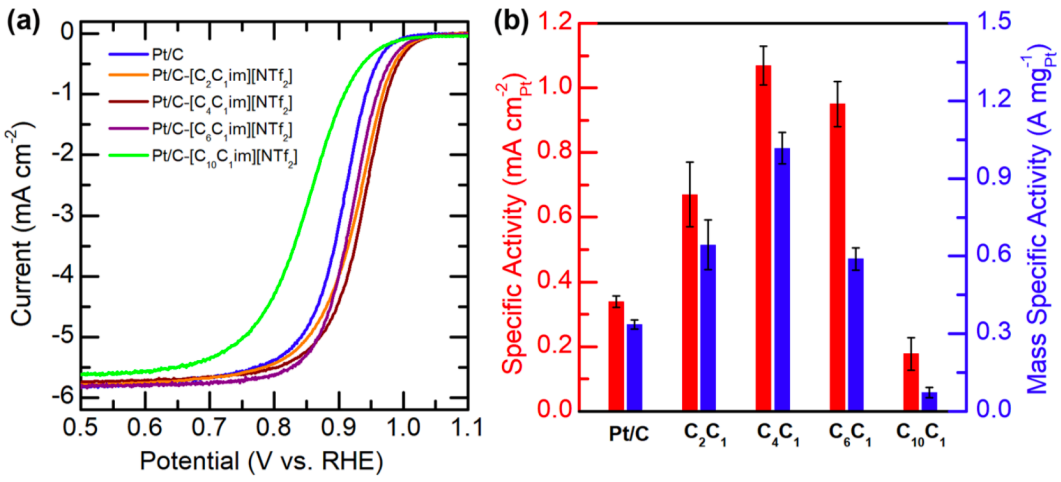


Figure 3-5 a) ORR polarization curves of IL-modified Pt/C catalysts and the pristine Pt/C recorded in $O_2$-saturated 0.1 M $HClO_4$ electrolyte at a scan rate of 10 mV $s^{-1}$. b) Comparisons MA and SA at 0.9 V on the pristine and IL-modified Pt/C catalysts[104].

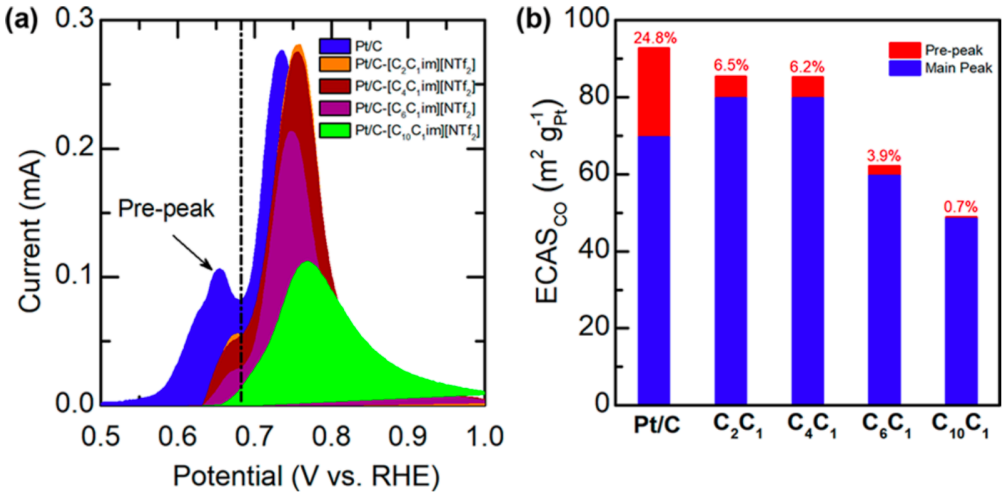


Figure 3-6 a) Background subtracted CO-stripping curves and b) summary of ECSA calculated based on CO-stripping peaks and the proportion of ECAS contributed to the pre-peaks[104].

Huang et al.[97] synthesized and explored a number of [MTBD]-based ILs with different anion structure. They impregnated HSA Pt/C catalyst (46.4 wt%, TEC10E50E) with these ILs and investigated the ORR activity in RDE setup. The optimum IL/C ratio was shown to be 2.56. Figure 3-7 shows the chemical structure of the cation and anions in IL.

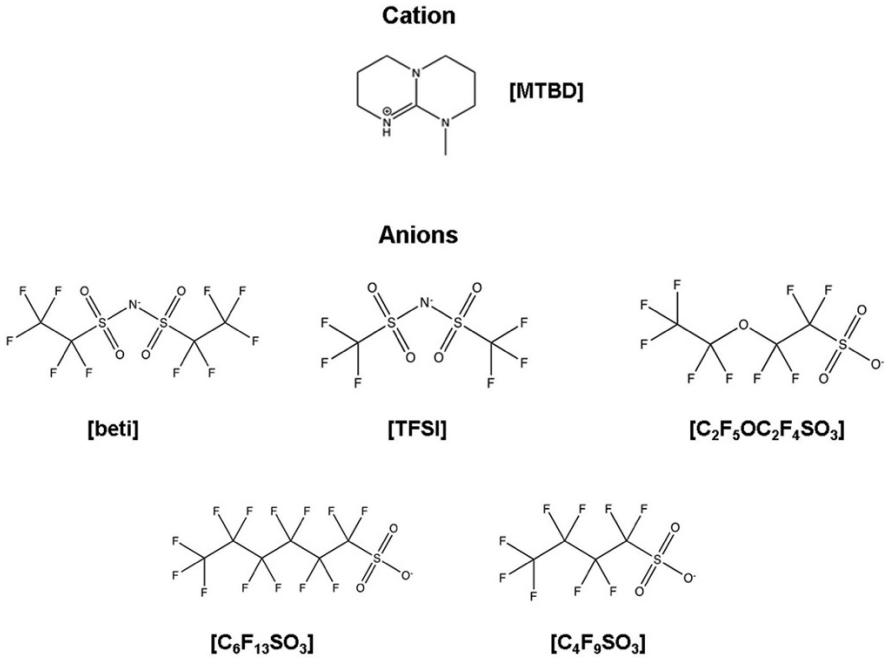


Figure 3-7 ILs chemical structure[97].

Figure 3-8 presents the electrochemical characterization of Pt/C-IL systems with optimum IL/c ratio. Most of Pt/C-ILs showed moderate ECSA loss of about 10-13%; however, [MTBD][$C_4F_9SO_3$] suffered the biggest ECSA loss of 28%. This is considered to be because of competitive adsorption of IL ions with hydrogen atom. On the other hand, Pt/C-[MTBD][$C_4F_9SO_3$] showed the best ORR performance reaching the MA of about 250 mA/$mg_{Pt}$ and SA of more than 400 μA/$cm^2_{Pt}$. Pt/C-[MTBD][beti] showed even higher MA compared to [MTBD][$C_4F_9SO_3$], but the specific activity is smaller although the ECSA loss was very less significant. Meanwhile, they revealed that the specific activity of the modified Pt/C catalyst has a linear relationship with the

availability of Pt active sites ($1-\theta_{OH}$), confirming that inhibition of Pt oxidation and less adsorption of non-reactive species leads to an enhancement in the ORR activity.

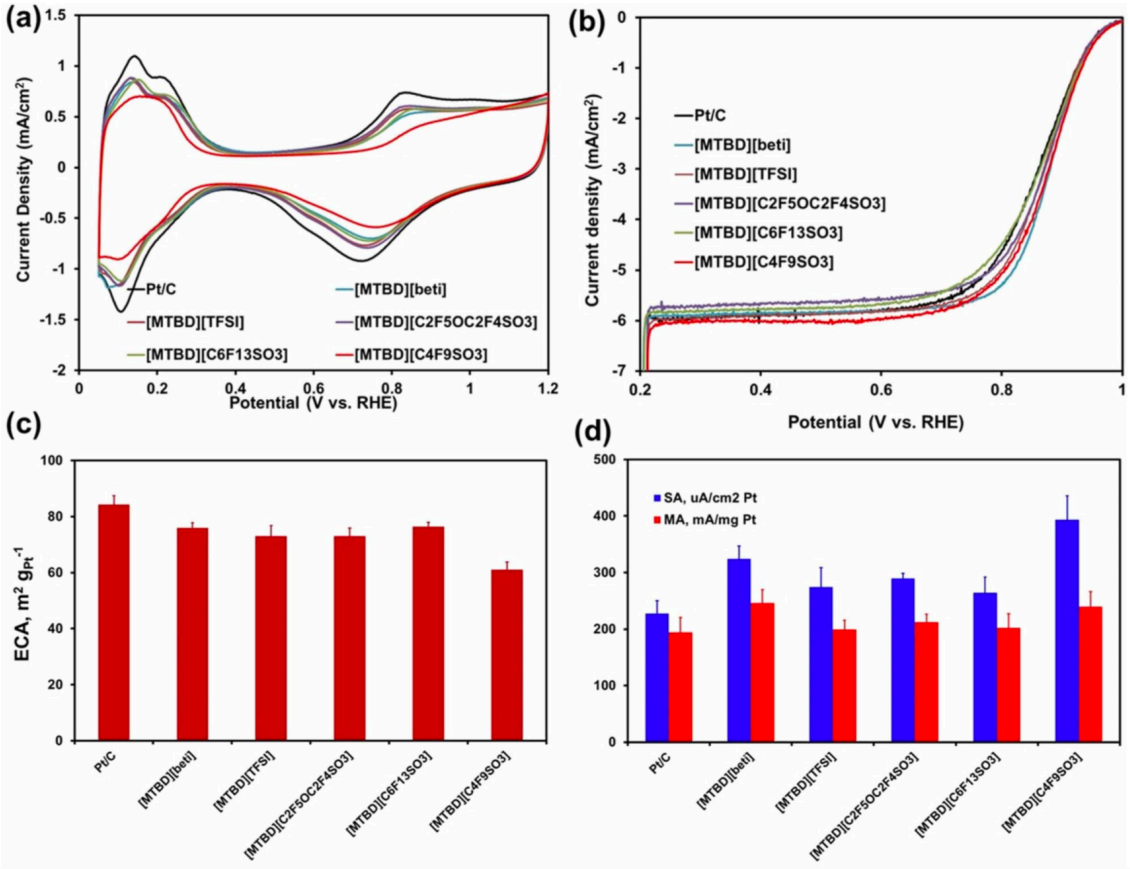


Figure 3-8 Electrochemical characterization of Pt/C and Pt/C-IL systems in Huang et al. work: a) CV curves in $N_2$-saturated 0.1 M $HClO_4$. b) Polarization curves in $O_2$-saturated 0.1 M $HClO_4$ at a rotation speed of 1600 rpm. c) ECSA of Pt/C-ILs. d) Mass activity and Specific activity measured at 0.9 V. The IL/C ratio is 2.56 for all Pt/C-ILs[97].

Electrochemical impedance spectrum displayed in Figure 3-9 was used to evaluate the proton conductivity in the catalyst layer. As can be seen, proton diffusion resistance ($R_{H^+}$) for IL-containing catalyst layer is slightly bigger in lower frequency compared to Nafion only. However,

when a mixture of Nafion and IL is used a more uniform catalyst layer in the co-presence of IL and Nafion increases the proton diffusion.

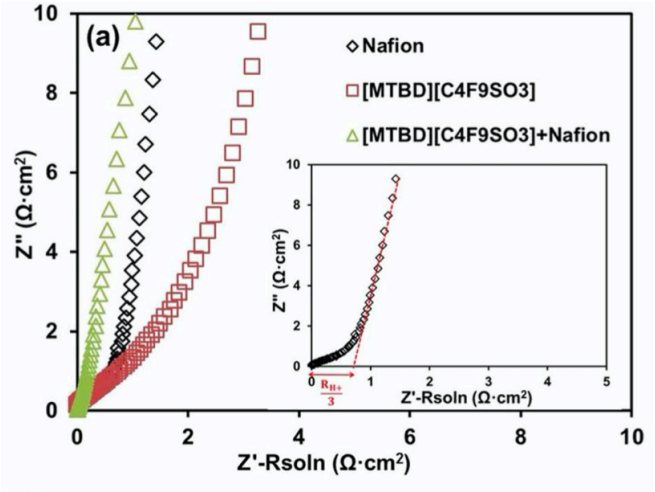


Figure 3-9 Nyquist plots of impedance spectra measured in saturated 0.1 M $HClO_4$ for (a) Catalyst layer blended with Nafion only, [MTBD][$C_4F_9SO_3$] only and a mixture of Nafion and [MTBD][$C_4F_9SO_3$][97].

Yan et. al[98] reported a new approach in electrocatalyst design by replacing Nafion with copolymer-containing IL segments or Poly(ionic liquid) as the proton conductor and binder. They synthesized poly(DMVBA$_n$-TfO-co-St$_m$) with average molecular weight of $10^4$ g mol$^{-1}$ illustrated in Figure 3-10. Copolymer compositions design was n/m=3:7, 5:5, and 7:3 where n/m is the fraction of the ionic segment to styrene block which is responsible for the rigid structure of the polymer.

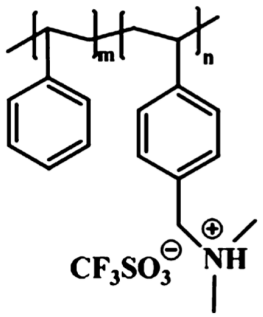


Figure 3-10 Chemical structure of the synthesized poly(IL)[98].

Electrochemical characterization of the poly(IL) ionomers are summarized in Figure 3-11. ECSA increase with decrease in the ionic segment of the PI, however still lower than the Nafion-Pt/C catalyst. Adsorption of oxygenated species was suppressed 22.8% for $DMVBA_3$-TfO-co-$St_7$ due the protection layer formed through the electrostatic interaction between ionic moieties on ionomers and Pt (Figure 3-11a). ORR performance increased with the increase in the styrene segment fraction as the hydrophobicity of the ionomer prevents the non-reactive species formation, and aromatic ring-induced rigid structure can facilitate oxygen transport to the surface of Pt. Comparison of the $E_{1/2}$ confirms the faster ORR in PIL containing samples compared to Nafion-Pt/C (Figure 3-11c)

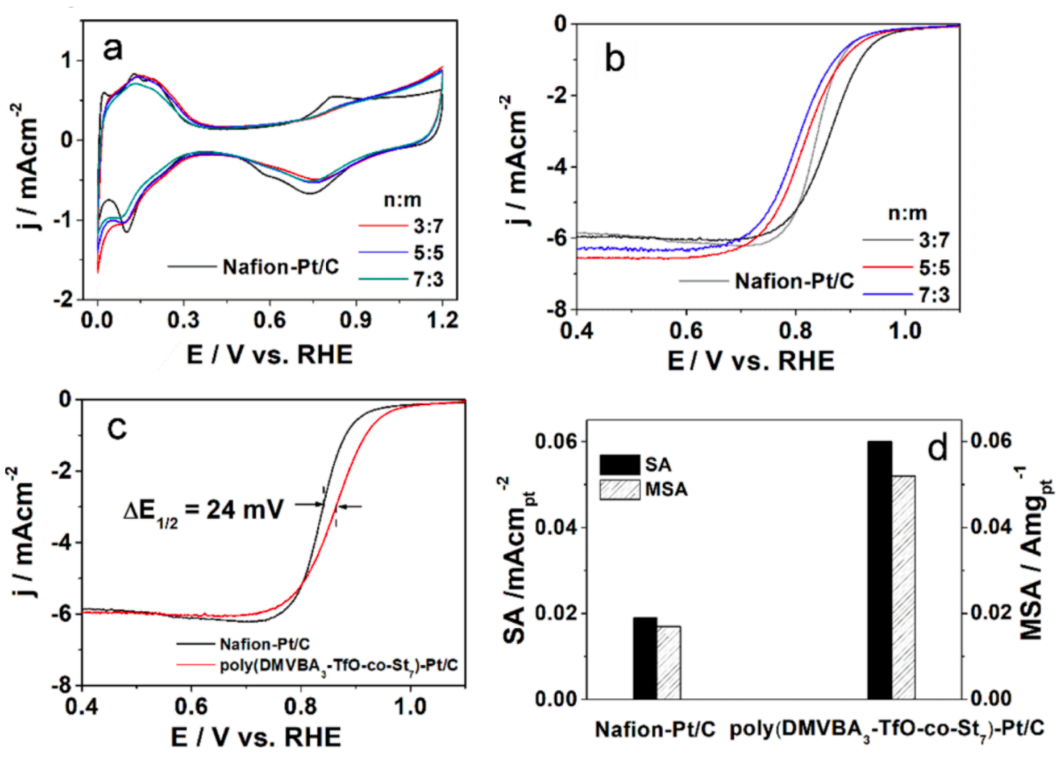


Figure 3-11 a) CV curves poly($DMVBA_n$- TfO-co-$St_m$)−Pt/C and Nafion−Pt/C in $N_2$-saturated 0.1 M HClO4 solutions at a scan rate of 20 mV $s^{-1}$. b) LSV curves of poly($DMVBA_n$- TfO-co-$St_m$)−Pt/C recorded in $O_2$-saturated 0.1 M $HClO_4$ solution at a scan rate of 20 mV $s^{-1}$ under a rotating speed of 1600 rpm. c) LSV curves and d) the calculated SA at 0.9 V for poly($DMVBA_3$-TfO-co-$St_7$)−Pt/C and Nafion−Pt/C recorded in $O_2$-saturated 0.1 M $HClO_4$ solution at a scan rate of 20 mV $s^{-1}$ under a rotating speed of 1600 rpm[98].

EIS results in Figure 3-12 also showed that by replacing Nafion with PILs $R_{H^+}$ decreased with the increase in the ionic fraction of the copolymer.

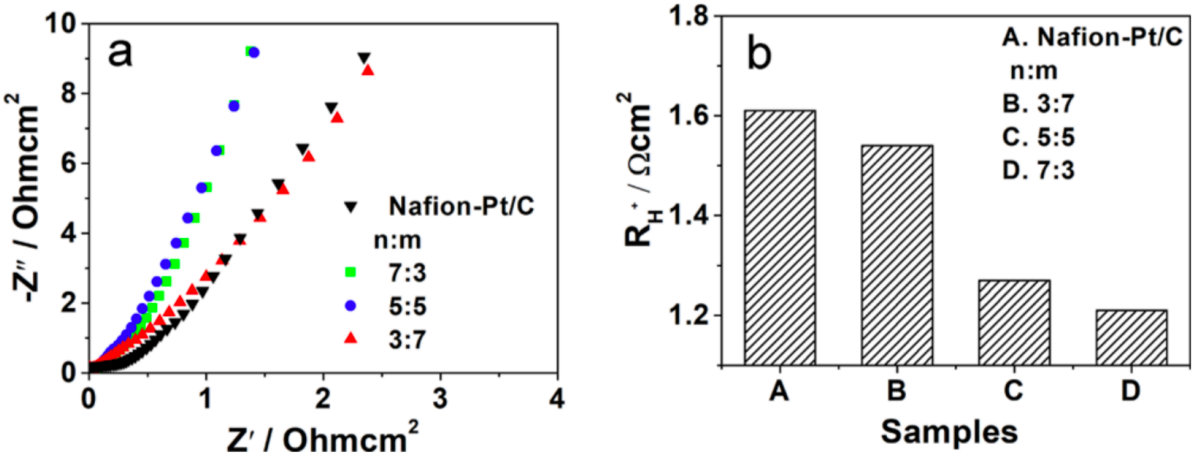


Figure 3-12 a) Nyquist plots of impedance spectra normalized to the electrode area measured under $N_2$-saturated 0.1 M $HClO_4$ for different catalyst layers. b) Proton resistance $R_{H^+}$ of different catalyst layers calculated from a)[98].

Durability studies are illustrated in Figure 3-13. ECSA decrease after 3000 cycles was 67.4 % and 58.1 % for Nafion-Pt/C and PIL-Pt/C samples, respectively. PIL-Pt/C showed much higher coverage of oxygenated species after cycling compared to Nafion-Pt/C samples confirming a drastic change in the micro-environment of the PIL-Pt/C catalyst. However, the ORR performance of PIL-Pt/C is still slightly higher than Nafion-Pt/C which is considered to be due the retention of the ECSA by the aggregation of the Pt nanoparticles. TEM images show that initial average size of the Pt nanoparticles is about 2.3 nm for both Nafion-Pt/C and PIL-Pt/C. After 3000 cycles, the average size of Pt nanoparticles increased to 5.01 and 3.58 for Nafion-Pt/C and PIL-Pt/C, respectively, indicating that he major factor of ORR performance decay is not the aggregation of the Pt nanoparticles. The authors suggested that the responsible factor for the significant change

in the micro-environment of PIL-Pt/C is the cycle-induced degradation of the hydrocarbon main chain of the polymer. Remaining PILs can protect the Pt nanoparticles form aggregation and provide sufficient proton conductivity.

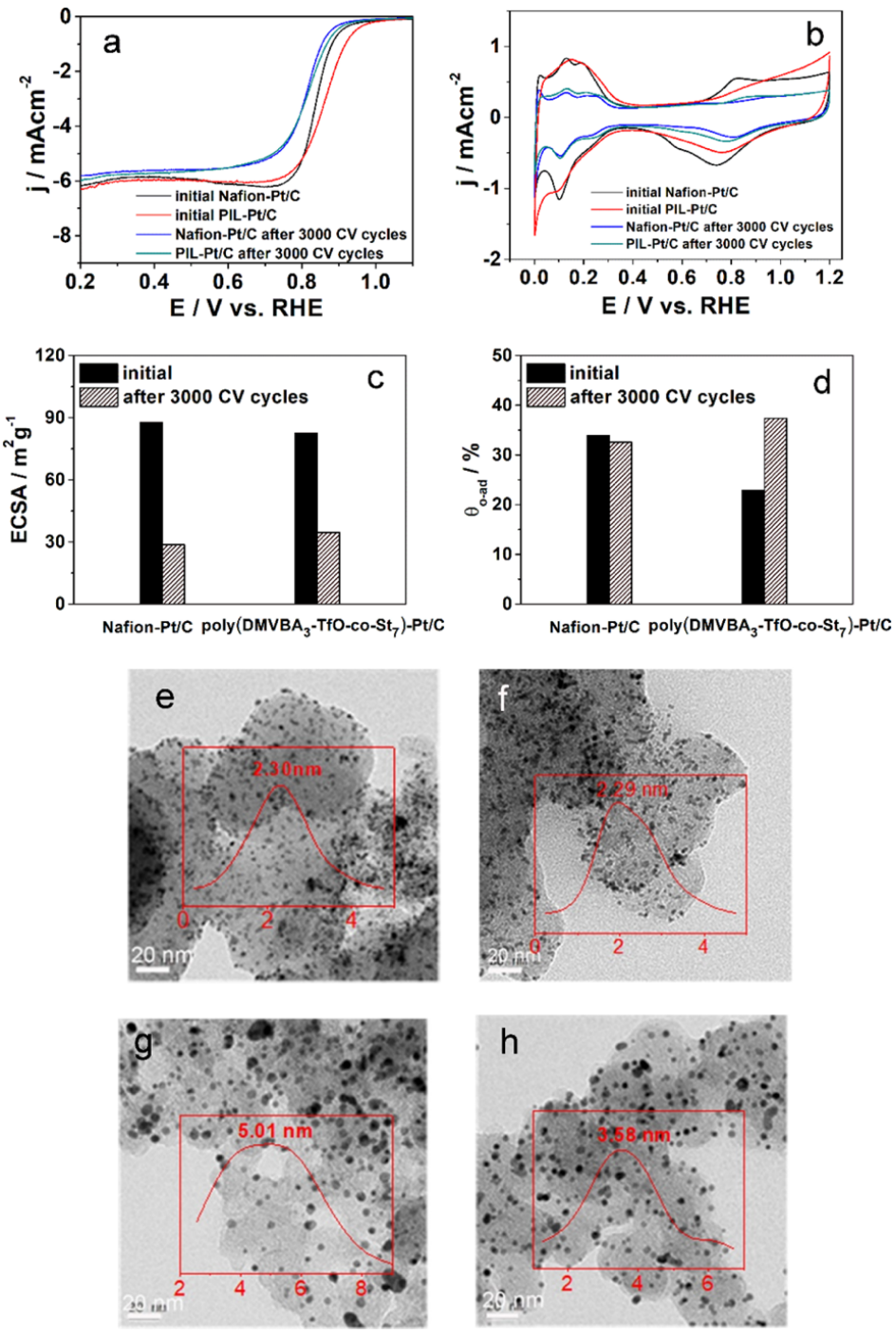


Figure 3-13 a) LSV curves, b) CV curves, c) ECSA values, d) and coverage of oxygenated species of PIL−Pt/C and Nafion−Pt/C before and after 3000 CV cycles in oxygen-saturated 0.1 M $HClO_4$ solution at a scan rate of 50 mV $s^{-1}$. e) Initial TEM images of Nafion− Pt/C f) and PIL−Pt/C. g) TEM images of Nafion−Pt/C, h) and PIL−Pt/C after 3000 CV cycles[98].

Li et al.[105] optimized the local ionomer electrocatalyst interface by developing a mixed ionomer system, Nafion/sulfonated poly (ionic liquid) block copolymer ionomer (SPILBCP). They used 47.7 wt% Pt/Vu (TKK, TEC10V50E), and tested a sample with Nafion as the only ionomer and Naion:C ratio of 0.6, three SPILBCP samples with different loadings of 0.3, 0.6, and 0.8, and a sample containing a mixture of Nafion and SPILBCP. The structure of the SPILBCP is shown in Figure 3-14. The tested samples include 0.6 Nafion:C, 0.3 SPILBCP:C, 0.6 SPILBCP:C, 0.8 SPILBCP:C, and 0.3 SPILBCP:C+0.3 Nafion:C. Cathode electrode loading was 0.07 $mg_{Pt}/cm^2$, and anode electrode was PtCo/HSC, with ionomer to carbon ration of 0.9, and loading of 0.03 $mg_{Pt}/cm^2$.

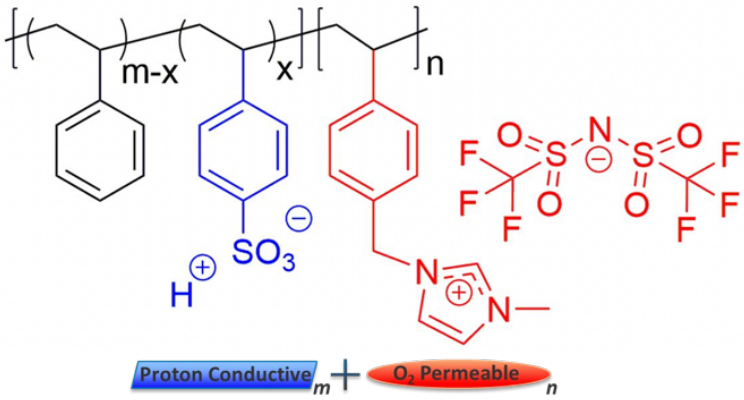


Figure 3-14 Sulfonated SPILBCP as ionomers for PEM fuel cells[105].

In order to reach the peak mass activity and power density, 2-3 voltage recovery cycles were performed for Nafion-containing MEAs, and 8 voltage recovery cycles for MEAs with SPILBCP (Figure 3-15). All loadings of the SPILBCP promotes kinetic performance compared to MEA with Nafion only; however, 0.6SPILBCP:C MEA showed doubled MA and SA at 0.9V compared to 0.6Nafion:C MEA in $H_2/O_2$ environment.

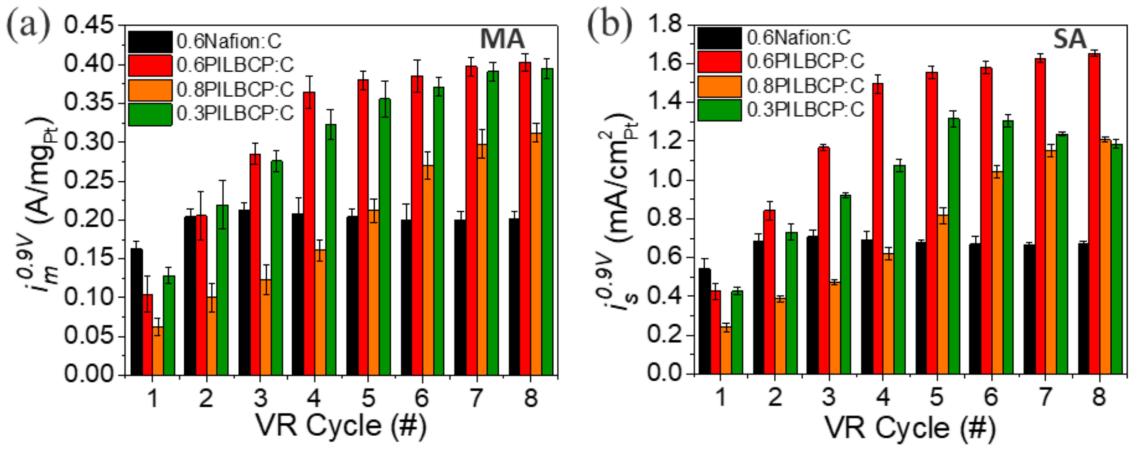


Figure 3-15 MA and SA of Pt/Vu MEAs from $H_2/O_2$ performance at 150 kPa, 80 °C, and 100% RH with indicated I/C[105].

Figure 3-16 summarizes the fuel cell testing results in $H_2$/air, including polarization curves, oxygen transport resistances for fully conditioned MEAs, and normalized ECSA calculated from CO stripping at a given RH relative to total ECA measured at 100% RH. There is no performance improvement in H2/air for MEAs containing SPILBCP only, even for 0.6 SPILBCP:C. SPILBCP MEAs showed over 70% NECA loss and much higher $R_{nf}$ both at dry and wet condition compared to Nafion-only MEA. On the other hand, when the mixture of Nafion and SPILBCP was used, lower $R_{nf}$ and identical NECA to Nafion-only membrane in wet condition were observed. 0.6SPILBCP:C+0.3Nafion:C MEA showed similar performance Nafion-only MEA in dry condition because the enhanced kinetic activity is offset by the reduced NECA. However, it showed improved performance in wet condition across the kinetic and mass transport-limited regions. This is considered to be because of the complex intramolecular interactions between side chains of SPILBCP which limits the formation of well-connected proton pathways. Integration of Nafion along with the SPILBCP, can facilitate the bridging of SPILBCP isolated aggregates while

establishing a connected ionomer network that helps the proton conductivity. As a result, catalyst layer developed with this method showed enhancement factor of about 2 in specific activity.

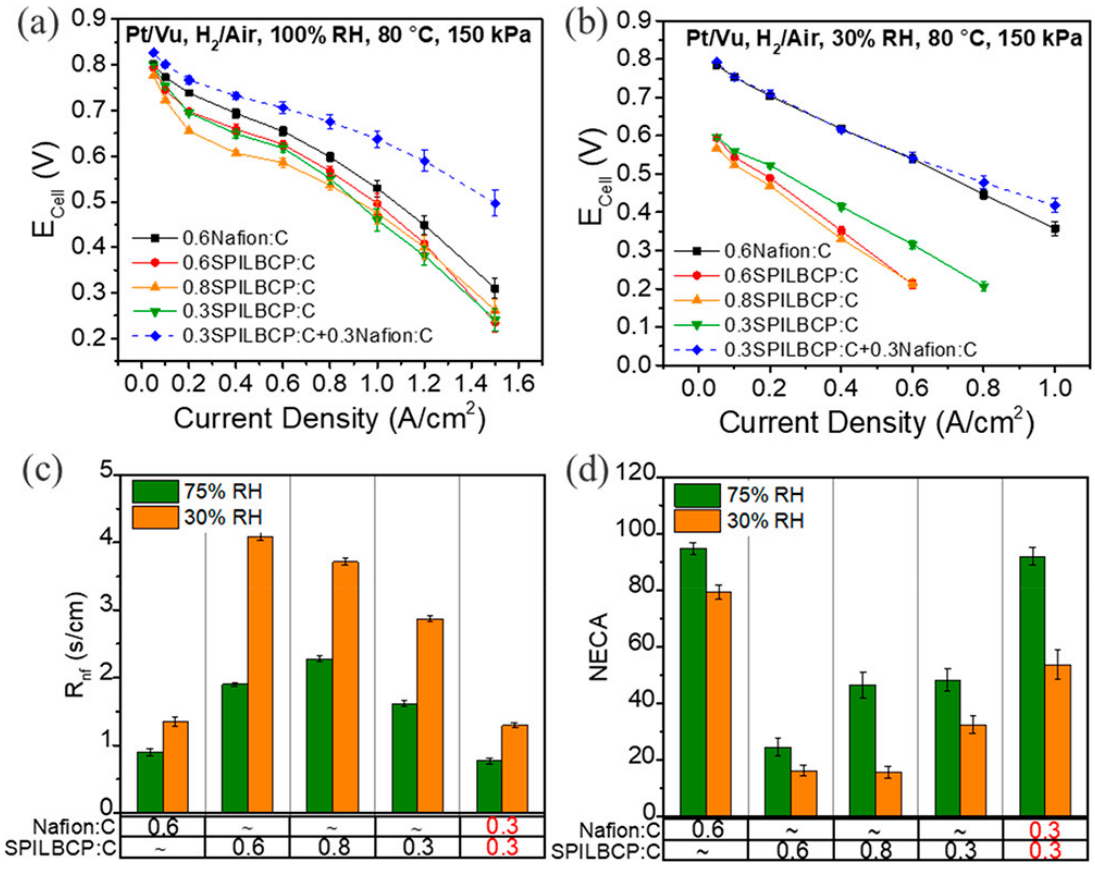


Figure 3-16 $H_2$/air performance at 80 °C, 150 kPa, and a) 100% RH and b) 30% RH. c) oxygen mass transport resistances, $R_{nf}$, d) Normalized ECA of fully conditioned Pt/Vu MEAs determined by CO stripping at 80 °C and indicated RH[105].

Small molecules can also serve similar role in enhancing specific activity of Pt electrocatalyst by disturbing local micro-environment of oxides formation. Melamine and melamine-formaldehyde polymer (PMF) are the novel materials reported for the modification of Pt electrocatalysts. In one study, Asahi et. al [83] reported the stable adsorption of poly(melamine-co-formaldehyde) or PMF polymer on commercial Pt/C catalyst, and enhancement of ORR activity. Nafion was not used in

this work to eliminate the effect of the ionomer. PMF was coated on Pt/C catalyst and then the electrochemical properties of the PMF-modified Pt/C catalyst were evaluated and compared to melamine-modified Pt/C. ECSA decrease in Figure 3-17 showed that 50 % and 30 % of Pt surface is covered with PMF and melamine, respectively. The $OH_{ad}$ peaks were suppressed and shifted to higher potential for both, but more significantly in case of PMF. It was suggested that protonated melamine motifs in acidic media can create hydration shells and destabilize the oxygenated species adsorption by preventing the formation of $OH_{ad}$-water network which leads to ORR improvement. By comparing the shift in the onset potential of ORR in LSV curves, it was suggested that the improved ORR performance of PMF-modified catalysts is due to the melamine segment of the copolymer not the formaldehyde (Figure 3-18).

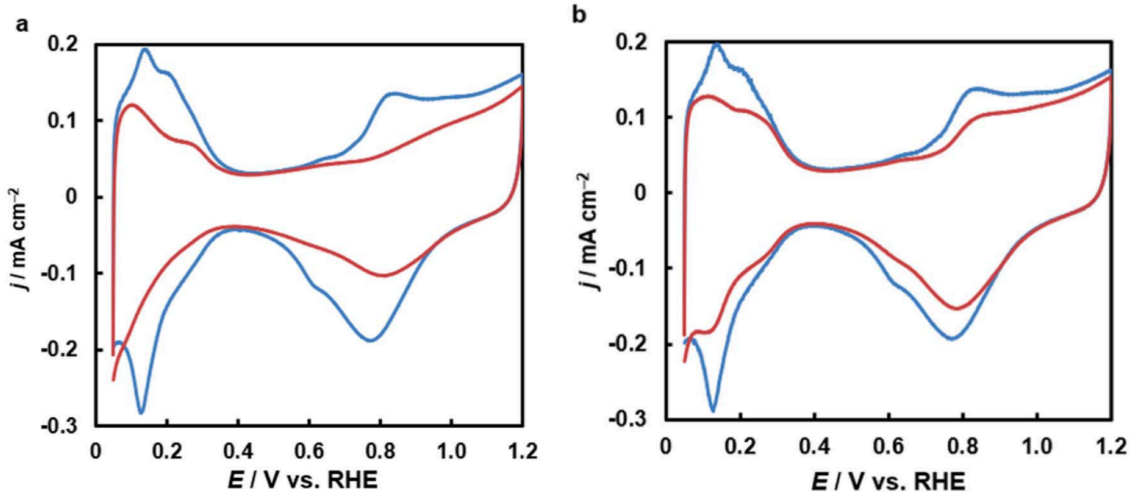


Figure 3-17 Cyclic voltammograms of a) PMF-modified b) melamine-modified Pt/C catalysts under argon in 0.1M $HClO_4$ at scan rate 100 mV $s^{-1}$ [83].

Adsorption stability of the compound were evaluated by additional potential test showing that polymer can adsorb more strongly to the surface of the Pt/C catalyst due to the higher molecular

weight and multiple melamine segments that can attach to the surface. On the other hand, melamine monomer is a small molecule that detaches from Pt surface more easily.

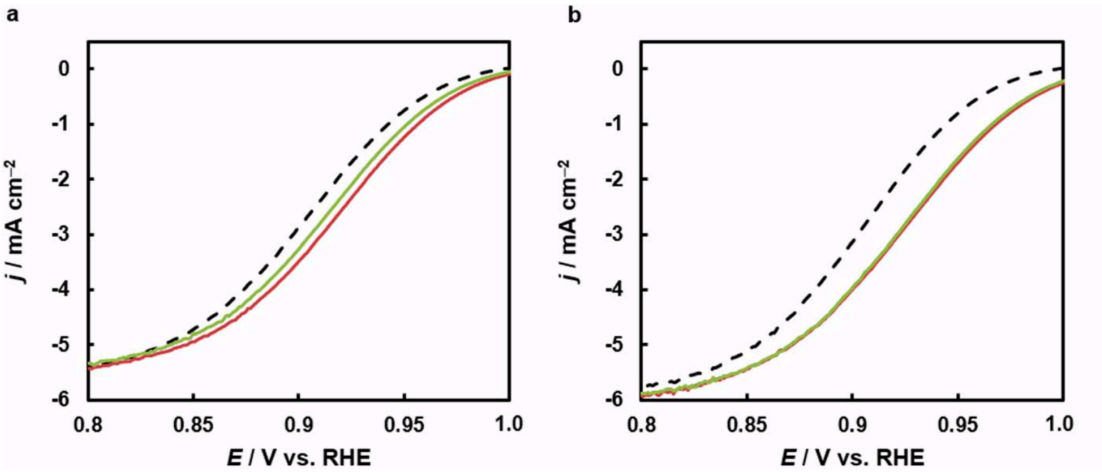


Figure 3-18 LSV voltammograms of in $O_2$-saturated conditions of a) melamine-modified and b) PMF-modified Pt/C catalyst before (red) and after (green) 150 potential cycles under argon at 100 mV $s^{-1}$ at 25°C. The black broken line shows the original curve for unmodified Pt/C catalyst[83].

Figure 3-19[106] shows the findings from electrochemical characterization of HSA and LSA Pt/C catalysts modified with various ILs, melamine small molecule, and low molecular weight PMF modifiers and compares the optimum systems mentioned above.

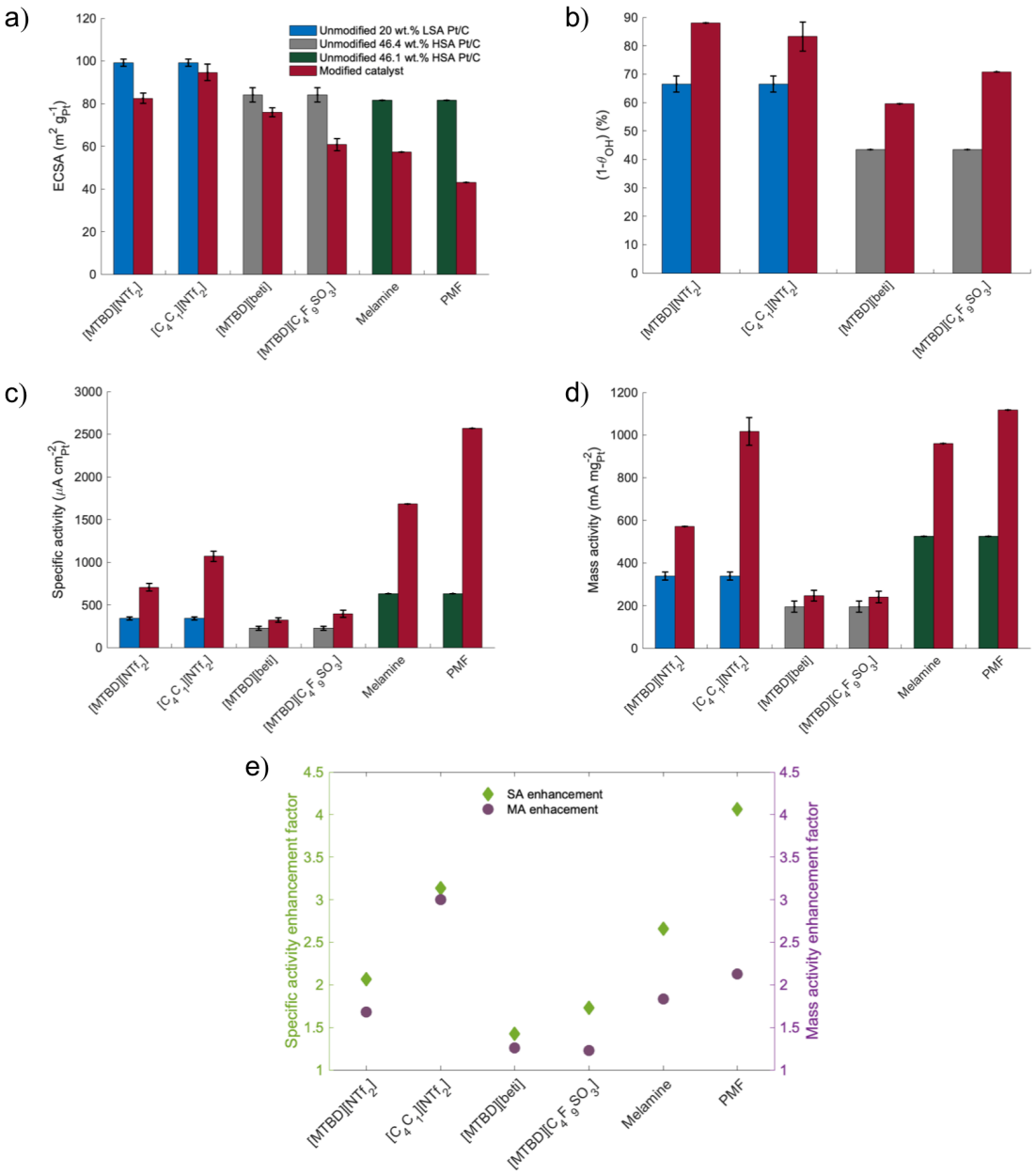


Figure 3-19 Comparison of electrochemical properties including a) ECSA, b) 1-$\theta_{OH}$ , c) specific and d) mass activity at 0.9 V on unmodified and modified LSA 20wt.% Pt/C catalyst with [MTBD][$NTf_2$] from Zhang et al. [103], unmodified and modified LSA 20wt.% Pt/C catalyst with [$C_4C_1$][$NTf_2$] from Zhang et al. [104], unmodified and modified HSA 46.4wt.% TKK catalyst with [MTBD][beti] and [MTBD][$C_4F_9SO_3$] ILs adapted from Huang et al.[97], unmodified and modified

HAS 46.1wt.% TKK catalyst with melamine molecule and low molecular weight PMF polymer modifiers[83]. e) Surface activity and mass activity enhancement factors for selected ionic liquids and two molecular modifiers.

## 3.3 Ionic liquid Selection Criteria for Fuel Cell Application

ILs are known to be self-dissociative molten salts that are composed entirely of ions. The criteria for choosing the suitable ionic liquid for the fuel cell application is as follows:

1- *Low melting point.*
2- *High thermal stability.* The IL should be thermally stable in the fuel cell application temperature range which is up to 80°C in the case of PEFCs.
3- *High electrochemical stability under the tested voltage range.* The cathode of fuel cell operates from 1.2 V to 0.1 V. It also operates under humidified conditions and oxygen environment.
4- *Low vapor pressure.*
5- *Non-flammable.*
6- *Hydrophobic.* Water management that has a large impact on the performance of the fuel cell depends on the wettability of the catalyst layer consisting of the Pt/C electrocatalyst, IL, and the binder. IL material should be hydrophobic so that the water molecules from the product would be repelled out of the pores, and due to Le Chatelier's principle the IL molecules remain in the pores by the capillary forces[84]. In addition, the hydrophobic microenvironment created by IL molecules prevents the Pt active sites from being oxidized or the formation of $OH_{ad}$[85].

7- *Minimal interaction of the IL with Pt surface.*

8- *Low viscosity.* The IL should be easy to process in order to be able to fill the micro- and meso- pores of the catalyst. In addition, the diffusion coefficient (D) of $O_2$ in the IL can be calculated by Stokes-Einstein equation relating D to the viscosity of the solvent ($\eta$). $K_B$ is the Boltzmann constant, T is the temperature, and $\alpha$ is the hydrodynamic radius of the oxygen. Very high viscosity leads to low $O_2$ diffusion and concentration in the IL.

$$D = \frac{K_B T}{6\pi\eta\alpha} \qquad [3\text{-}1]$$

9- *High $\Delta pK_a$ value*[107]. It has been shown that satisfactory proton transfer can be achieved by $\Delta pK_a > 10$. $\Delta pK_a$ is the difference between the $pK_a$ of the constituent acid and protonated base. In the study by Muhammed Shah et al.[107], bis(trifluoromethanesulfonyl)amide acid ($H[NTf_2]$) was chosen since it is a super strong acid with the very low $pK_a$ of -10, and then they compared the properties of different ILs containing different amines as the base including tertiary amines DBU, pyrazine (Pyra), pyridine (Pyri), 1-ethylimidazole (EIm), diethylmethylamine (dema), 5-methyl- isoxazole (MIox); and secondary amines pyrrolidine (Pyrr), morpholine (Morp), and 1,2,4-triazole (TZL). Chemical structures and corresponded $\Delta pK_a$ values are summarized in Figure 3-19 and table 2. For the ILs with high ΔpKa, complete proton transfer from the Bronsted acid to the base is assumed due to the fast kinetics [108]. According to thermogravimetric analysis, all the $H[NTf_2]$-based ILs exhibited superior thermal stability.

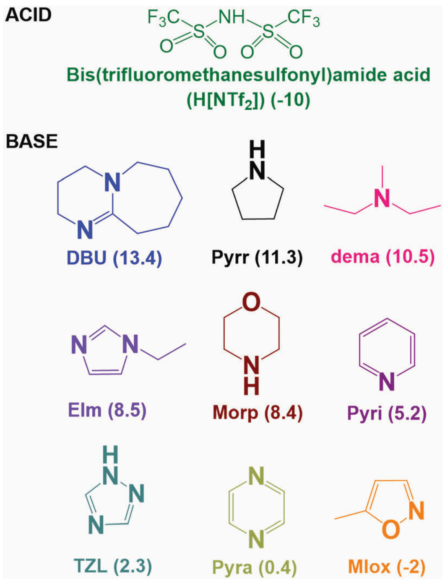


Figure 3-20 Chemical structure of the ILs[107].

Table 3-1. $\Delta pK_a$ values[107].

| ILs | $\Delta pK_a$ |
|---|---|
| [MIox][$NTf_2$] | 8.0 |
| [Pyra][$NTf_2$] | 10.4 |
| [TZL][$NTf_2$] | 12.3 |
| [Pyri][$NTf_2$] | 15.2 |
| [Morp][$NTf_2$] | 18.4 |
| [EIm][$NTf_2$] | 18.5 |
| [dema][$NTf_2$] | 20.5 |
| [Pyrr][$NTf_2$] | 21.3 |
| [DBU][$NTf_2$] | 23.4 |

The temperature dependence of the ionic conductivity and viscosity are also shown in Figure 20 and 21. The viscosity values follow the order based on the cations: $[TZL]^+$ > $[Morp]^+$ > $[Pyra]^+$ > $[DBU]^+$ > $[Pyri]^+$ > $[EIm]^+$ ~ $[Pyrr]^+$ > $[dema]^+$, and ionic conductivity values follow the order: $[dema]^+$ > $[Pyrr]^+$ ~ $[EIm]^+$ > $[Pyri]^+$ > $[Pyra]^+$ > $[DBU]^+$ > $[TZL]^+$ > $[Morp]^+$. As the operating temperature for PEFC is 80°C and values show the same trend at this temperature, it can be concluded that pyrrolidinium, Imidazolium, and quaternary ammonium IL systems, are the best candidates in terms of viscosity and conductivity.

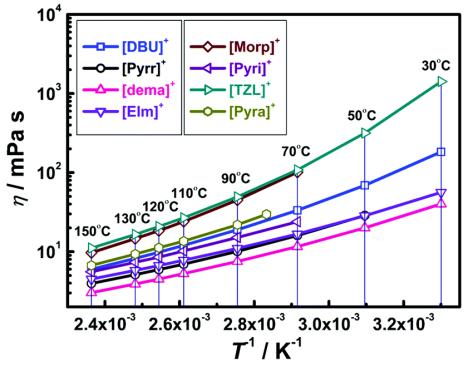


Figure 3-21 Viscosity as a function of the temperature for $[NTf_2]$-based ILs[107].

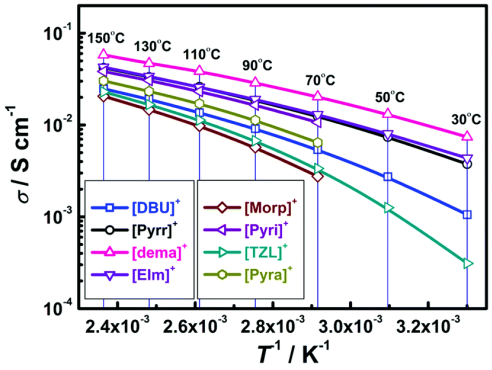


Figure 3-22 Ionic conductivity as a function of the temperature for $[NTf_2]$-based ILs[107].

*High oxygen solubility to facilitate $O_2$ transfer to the catalyst.* An IL with a higher $O_2$ solubility compared to aqueous media will increase the $O_2$ residence time within the pores filled with IL due to the confinement effect reported by Snyder et. al[84,86]. As the $O_2$ molecule diffuses into pores, it is chemically biased to stay there, so the increased interaction frequency with the catalyst will decrease the ORR overpotential.

From the diffusion coefficient and $O_2$ concentration information provided in the Table 3-2, it can be concluded that imidazolium-based cations paired with $N(Tf)_2$ anion have the potential of providing enough oxygen solubility while maintaining an acceptable range of viscosity and ionic conductivity.

Table 3-2. Diffusion coefficient and concentration of oxygen in ionic liquid[101].

| System | $10^6 D_{O_2}$ ($cm^2 s^{-1}$) | $C$ (mol $cm^{-3}$) | $\eta$ (mPa s) | Temperature (°C) |
|---|---|---|---|---|
| Imidazolium | | | | |
| $[C_2mim][N(Tf)_2]$ | 7.3 | 3.9 | 32.1 | 20 |
| $[C_2mim]BF_4$ | 17 | 1.1 | 37 | 25 |
| $[C_3mim]BF_4$ | 13 | 0.97 | 103 | 25 |
| $[C_4mim]BF_4$ | 12 | 1.1 | 180 | 25 |
| $[C_4mim]PF_6$ | 2.2 | 3.6 | 312 | 25 |
| Quaternary ammonium | | | | |
| $[N_{2226}][N(Tf)_2]$ | 1.48 | 11.6 | 220 | 20 |
| $[N_{2226}][N(Tf)_2]$ | 3.2 | 8.9 | 220[a] | 35 |
| Pyrrolidinium | | | | |
| $[C_4mpyr][N(Tf)_2]$ | 1.8 | 13.6 | 89 | 25 |
| $[C_4mpyr][N(Tf)_2]$ | 5.2 | 6.1 | 95[a] | 35 |
| Quaternary phosphonium | | | | |
| $[P_{66614}][N(Tf)_2]$ | 7.5 | 6.0 | – | 35 |
| $[P_{66614}]FAP$ | 6.1 | 7.8 | – | 35 |
| $[P_{66614}]TPTP$ | 9.5 | 8.0 | – | 25 |
| $[P_{66614}][N(Tf)_2]$ | 1.7 | 9.8 | 369 | 20 |
| $[P_{66614}][N(CN)_2]^-$ | 2.1 | 9.1 | 474 | 20 |

[a]Measured at 20 °C

*10- High proton conductivity.* IL should be capable of transferring protons to the Pt surface. It has been shown that Imidazolium/H[$NTf_2$] composition and $H_2$ are electroactive with Pt as the following equilibrium occurs[109]:

$$2HIm^+ + 2e^- \leftrightarrow 2Im + H_2 \quad [3\text{-}2]$$

$HIm^+$ acts as a proton carrier in the system and ORR can be expressed as the 4-electron pathway described as follows:

$$O_2 + 4HIm^+ + 4e^- \rightarrow 2H_2O + 4Im \quad [3\text{-}3]$$

Proton migration can occur by mixed Grotthuss and vehicular mechanisms[109]. Additionally, conformational flexibility of $[NTf_2]^-$, distributed negative charge, and multiple N and O atoms as H-bond acceptor sites in the structure of the anion, along with the parallel π-π stacking in the structure of imidazole-derived ILs facilitate the hydrogen bonding. Therefore, protons can transfer fast by Grotthuss mechanism through the formed hydrogen-bonded network between IL molecules and hydronium anions [107,99,110].

Their unique characteristics such as high ionic conductivity, presence of protons in the cationic structure, negligible vapor pressure, thermal and electrochemical stability make them a promising additive to enhance the ORR in the cathode electrode of PEFCs [111,99]. They should also have low viscosity in order to be able to fill the pores without restricting $O_2$ diffusion. They should also possess high $\Delta pK_a$ value so that satisfactory proton transfer from the Bronsted acid to the base can be achieved due to the fast kinetics [107,108].

Finally, IL material should be hydrophobic as the increased $O_2$ solubility will facilitate the attraction of the reactants; therefore, the hydrophobic nature of ILs would help repulse the produced water out of the pores due to Le Chatelier's principle[84]. In addition, the hydrophobic

microenvironment created by IL molecules prevents the Pt active sites from being oxidized and suppress the formation of oxygenated species. Therefore, the IL molecules protect the Pt active sites from being occupied by non-reactive species accelerating the ORR kinetics because strong Pt-O bonding is known to slow ORR[112].

## 3.4 Materials and Methods

### 3.4.1 Materials

The Pt/C electrocatalyst was 40 wt.% platinum on high surface area Ketjenblack obtained Fuel Cell Store (College station, Texas, United States). $HClO_4$ (70%), 2-Propanol BioReagent (99.5%) were purchased from Millipore Sigma (Burlington, Massachusetts, United States). Imidazolium-derived ILs including 1-ethyl-3-methylimidazolium bis(trifluoromethylsulfonyl)imide ($[C_2mim]^+[NTf_2]^-$), 1-butyl-3-methylimidazolium bis(trifluoromethylsulfonyl)imide ($[C_4mim]^+[NTf_2]^-$), and 1-butyl-2,3-dimethylimidazolium bis(trifluoromethylsulfonyl)imide ($[C_4dmim]^+ [NTf_2]^-$) were obtained from Solvionic Co., (Toulouse, France). All the reagents were used as received without further purification.

### 3.4.2 Pt/C Modification with ILs

The ILs impregnation method into the catalyst powder was adopted from Ref [97]. 9.5 mg of the Pt/C electrocatalyst was first placed in a vial and wet by 0.5 ml of DI water. Based on the desired ratio of IL/C, IL solution with the concentration of 5 mg/ml was prepared. A solution of the imidazolium-derived ILs in IPA was prepared with 5mg $ml^{-1}$ concentration. Then, the IL solution was mixed with the wetted Pt/C electrocatalyst, and ultrasonicated for 20 min. The mixture was

then stored on a magnetic hotplate stirrer at 45°C and the solvents were evaporated slowly into the ambient atmosphere while continuously mixed with a magnetic stir bar. The obtained powder was further dried under vacuum at room temperature overnight. This impregnation method was used to integrate Imidazolium-derived ILs into Pt/C catalyst with different IL/C ratios of 0.64, 1.28, and 2.56.

### 3.4.3 Rotating Disk Electrode (RDE)

#### 3.4.3.1 Ink Preparation and Deposition on RDE Electrode

In order to achieve final Pt loading of 40 $\mu g_{Pt}\ cm^{-2}_{geo}$ on the disk, 5 mg of the impregnated catalyst was mixed with 996.5 µl of MilliQ $H_2O$:IPA (24 wt.% IPA), and 8.12 µl of a 5 wt.% Nafion solution. To promote the uniform distribution of the catalyst, the ink was ultrasonicated for 1.5 h. The ultrasonic bath temperature was maintained below 40°C by adding ice to preserve Nafion structure [113]. A 10µl aliquot of the catalyst ink was pipetted in two parts (5µl each) on glassy carbon tip mounted on an inverted rotator shaft while rotating at 60 rpm. Then, the rotation gradually increased to 500 rpm, and the ink dried under ambient conditions while rotating.

#### 3.4.3.2 Electrochemical Cell Preparation

The electrochemical cell glassware is custom-made for the purposes of these experiments by Adams & Chittenden (Berkeley, California, United states). References electrode is connected to the main body of the cell by a salt bridge, to avoid any contamination [113]. To obtain reproducible measurements and absolute values of activities, glassware must be cleaned thoroughly of organic impurities; therefore, before each experiment, the electrochemical cell and the glassware were

soaked in piranha solution (solution of concentrated $H_2O_2$ and $H_2SO_4$ with equivalent volumes) overnight. Then, they were all washed thoroughly with MilliQ water (18.2 MΩ) and boiled for 2 min to remove adsorbed $H_2SO_4$ from Piranha. To obtain a uniform catalyst layer, the glassy carbon electrode was polished using alumina slurry (5 μm, 0.3 μm and then 0.05 μm), followed by excessive cleaning with acetone, ethanol, and MilliQ water. All the electrochemical measurements were performed by a Gamry potentiostat (1010E interface), using the surface mode. The electrolyte was 0.1M $HClO_4$ prepared with MilliQ water (18.2 MΩ). A Hydrogen reference electrode (Hydroflex, Gaskatel, Kassel, Germany) and a Pt wire were used as reference electrode and counter electrode, respectively. All potentials in this work are reported against a reversible hydrogen electrode (RHE).

### 3.4.3.3 Electrochemical Characterization

The electrochemical characterization was performed as follows. The cell was first pre-conditioned by purging with $N_2$ for 20 min. To clean the surface of the electrocatalyst, activation CV was performed by sweeping the potential between 0.05 V and 1.23 V vs. RHE at 500 $mV.s^{-1}$ for 100 cycles. Then, five stable CVs were recorded in the same potential range at 20 $mV.s^{-1}$. EIS was performed at 0.40 V vs. RHE, from 2 MHz to 1 Hz to measure ohmic resistance and protonic resistance ($R_{H^+}$). A LSV was also recorded under $N_2$-saturated condition at 1600 rpm between 0.05 and 1.05 V vs. RHE at 20 $mV.s^{-1}$ for background correction. Then, the cell was purged with $O_2$ for 20 min. ORR activity was evaluated by LSV at 5 $mV.s^{-1}$ toward an anodic scan (0.1 V-1.05 V vs. RHE) at 400, 900, and 1600 rpm.

### 3.4.4 MEA Fabrication and Assembly

#### 3.4.4.1 Preparation of Catalyst Ink

Modified and unmodified Pt/C catalyst were weighed and dispersed in a mixture of DI water and 1-propanol resulting in a final concentration of 0.003 g/ml. Optimum cathode inks were moderate-water content ink with 51 wt.% water in solvent. The D521 Nafion™ Dispersion - Alcohol based 1100 EW at 5 wt% ionomer was then added to the ink solution to get ionomer to carbon I/C of 0.8. Then, the ink was ball milled along with $ZrO_2$ balls for 18 h and wet film applicator with 200 µm thickness was used to coat on fiber reinforced Teflon substrate (250 µm thick) using tape casting machine (13 mm $sec^{-1}$). Coated decal was hot pressed on Nafion XL membrane (27.5 µm) at 155°C for 3 min at ~ 0.1kN $cm^{-2}$ of force. Weight of decal was measured before and after hot pressing to calculate the final Pt loading. The composition of MEAs and Pt loading were then confirmed with X-ray fluorescence (XRF) spectroscopy to be in a range of 0.13±0.02 mg $cm^{-2}$. Catalyst coated membranes were then fitted into 5$cm^2$ active area (1.35 cm x 3.7 cm) by impermeable PET subgaskets (8um thickness) to precisely span 14 parallel channels over 3.7 cm of DOE flow-field for differential condition as PET gaskets inhibited cross-channel convection. The CCMs were sandwiched between two Freudenberg H23C6 GDLs at 20 % compression. The CCMs, GDLs, and polytetrafluoroethylene gaskets (27.5 µm PTFE and 120 µm fiber reinforced PTFE) were then placed between the flow fields, and the bolts were tightened at a torque of 13.5 N.m.

### 3.4.5 In-situ Fuel Cell Characterization

Scribner 850e fuel cell test stand with maximum current load of 50 A from Scribner Associates, Connecticut, USA was used for performing accelerated stress test (AST) and measuring performance metrics such as polarization curve and mass activity, oxygen transport resistance. AST was performed in $H_2/N_2$ environment at 80°C and 100% relative humidity (RH) using a square-wave potential profile from 0.6 to 0.9 V with 3s hold at each potential. VSP-BioLogic 4A potentiostat was used for recording CV, LSV, and EIS.

The cell was first heated up to 60°C and 100 % relative humidity. MEAs were conditioned by potential holds of 30s at 0.8, 0.6, and 0.3 V until constant current was achieved. It usually took about 200 cycles to reach this point. Voltage recovery was performed at 0.2 V under $H_2$/air environment at 40°C and 150 % RH for 2 h. Polarization curves preceded with a voltage recovery step to retrieve all the recoverable losses. I-V curves generated under differential condition by holding the cell at constant currents for 3 mins at 80 °C and 150 kPa total pressure with 100% RH. Polarization curves were stepped from high current densities to low current densities. The corresponding potentials at multiple points were measured and averaged over 3 mins. Oxygen mass transport resistance was measured at 80 °C and 75 % RH, with inlet dry mole fraction of $O_2$ in $N_2$ maintained at 1,2, and 4 %. The outlet pressure was controlled at 100, 125, 150, 200, $kPa_{abs}$. The limiting current was measured at constant voltages of 0.30, 0.24, 0.18, 0.12, and 0.06 V and held for 3 min. The details of this procedure is discussed previously by Baker et al [114]. The transient current response (I−t) resulting from the introduction of CO to an equilibrated electrode held at 0.35 V was measured as the adsorbed anions and cations will be displaced with CO through oxidation and reduction processes. Displacement charge will show the amount of charged surface species at 0.35 V. Potentiostatic EIS was performed at 80°C under fully

humidified $H_2/N_2$ environment. The DC potential was kept at 0.2 V with an AC amplitude of 5% of the DC potential, from a frequency of 10,000 Hz to 0.1 Hz. For the catalyst layer ionic conductivity calculations, EIS data was used. The impedance spectra from EIS data showed a 45° line in the high to medium frequency region where real and imaginary parts are equal, followed by a straight vertical line, representing a capacitive region. A physical impedance model, transmission line model (TLM), was used to fit the EIS data at high frequencies to measure the proton conductivity of the cathode catalyst layer [115].

### 3.4.6 Ex-situ Characterization

#### 3.4.6.1 Experimental Parameters for $N_2$ Physisorption

Nitrogen gas physisorption was conducted with *Micromeritics 3Flex* Adsorption Analyzer to study the porosity and hydrophobicity of the Pt/C and PtC-IL samples. The samples were first degassed at 150 °C for 12 h before analysis. Nitrogen physisorption was performed at 77 K between a relative pressure ($P/P_0$) of 0 and 0.995, wherein a low pressuring dosing (2 $cm^3 g^{-1}$ STP) mode was used below 0.01 ($P/P_0$) for the microporous structure. The specific surface area was estimated by Brunauer–Emmett–Teller (BET) Model, and t-plot model was used to estimate the micropore volume/area and mesopore surface areas. The pore size distribution (PSD) above 2 nm was calculated with BJH model by using the adsorption isotherm. The PSD below 2 nm was estimated by non-linear DFT model assuming a slit pore geometry.

### 3.4.6.2 Transmission Electron Microscopy

Aberration corrected-TEM was performed on a JEOL JEM-ARM300CF microscope operated at 80 keV to minimize the beam damage to the sample. TEM samples were prepared by dispersing powders in the mixture of Millipore water and IPA through ultrasonication. A drop less than 5μL was then placed onto holey carbon-coated copper grids and further dried before placing into the TEM.

### 3.4.6.3 Water Uptake and Contact Angle Measurements

Samples for this measurement were also prepared using the same recipe explained earlier. The catalyst inks were coated evenly on both sides of an Ethylene Tetrafluoroethylene (ETFE) substrate. After having the ink coated on the substrate, the film was then cut into a 3×2 cm rectangle and was subjected to external contact angle measurement in order to evaluate the wetting properties using a Krüss K100 force tensiometer. The technique by which these experiments were performed is developed by Abbou et al[116]. Each sample was suspended from the top of the instrument microbalance and the glassware vessel containing DI water was placed on top of the motorized platform. The sample was then immersed into the DI water for 1 cm at a constant rate of 10 cm $min^{-1}$. After having been submerged for 900 seconds in water, the vessel was removed causing a sudden increase in the mass detected by the microbalance. Using Wilhelmy equation ([3-4]) and the changes in the mass of each sample when it was removed from the water at 900s, the external contact angle was calculated. $\Delta m$ is the changes in the mass of the catalyst layer after being removed from the water, $\rho_l$ is water's density, $V_i$ is the fraction of the sample immersed into the water and can be calculated by $V_i = Led$.

$$\theta = cos^{-1}\left(\frac{-\Delta m.g+\rho_l g V_i}{2(L+e)\gamma}\right) \quad [3\text{-}4]$$

Details of the exact experimental details can be found in Ref. [117]. The amount of water uptake shown in Table 1 is calculated based on the difference between the initial weight of the sample and its weight after water absorption at 900s before being removed from water vessel.

### 3.4.6.4 Zeta Potential Measurement

The IL-modified electrocatalysts were used to prepare ink solutions for zeta potential measurements. Ink samples were prepared by adding 0.1 wt. % C in solution using a 5:5 weight ratio of IPA and DI water. The samples were then sonicated for roughly 30 minutes or until a homogenous mixture was obtained. For ink dispersions containing ionomer, a constant I/C of 0.8 was maintained using Nafion Dispersion D521. Zeta potential measurements were performed using Horiba SZ-100 and a count rate of 100 kCPS to ensure the samples were sufficiently dilute for electrophoretic measurements. In order to avoid bubbles interfering with the measurements during pipetting the ink solution into the electrode cell, the cell was tilted or tapped slowly to force the bubble out. Once the electrode was sufficiently filled with the sample, parameters including refractive index, viscosity and dielectric constant were specified within the software for the given dispersion medium.

### 3.4.6.5 X-ray Photoelectron Spectroscopy

XPS was performed on a Kratos AXIS Supra spectrometer with a monochromatic Al Kα source. For CO (MATHESON HG G1918775, ultra-high purity) dosing experiment, samples were moved to a chamber at the back of the Surface Science Station (SSS) inside the Kratos AXIS Supra spectrometer. The pressure of the chamber is the same as the pressure in the SSS. Before dosing the CO gas, gas lines were vacuumed to at least 6 x $10^{-9}$ Torr. CO flowed into the chamber until the pressure reached 2 x $10^{-5}$ Torr. When all the valves were closed (no gas exchange with outside), and the sample sited in the chamber. for10 minutes. the chamber was vacuumed to at least 5 x $10^{-8}$ Torr, and samples were transferred to the Specimen Analysis Chamber (SAC) for measurement. Residual Gas Analyzer (MKS, e-Vision 2) was used to monitor the gas. The powder samples were mounted on copper tape, and the MEA samples were mounted on carbon tape.

CasaXPS software was used to analyze the data. All spectra calibrated based on the $sp^2$ carbon (284 eV). 70% Gaussian / 30% Lorentzian setup was used for all data but $sp^2$ carbon. An asymmetric 80% Gaussian / 20% Lorentzian setup was applied for $sp^2$ carbon.

## 3.5 Results

### 3.5.1 TEM Images

Figure 3-23 represent the TEM images of pristine and IL-modified Pt/C catalysts. The arrows show IL layer and lumps.

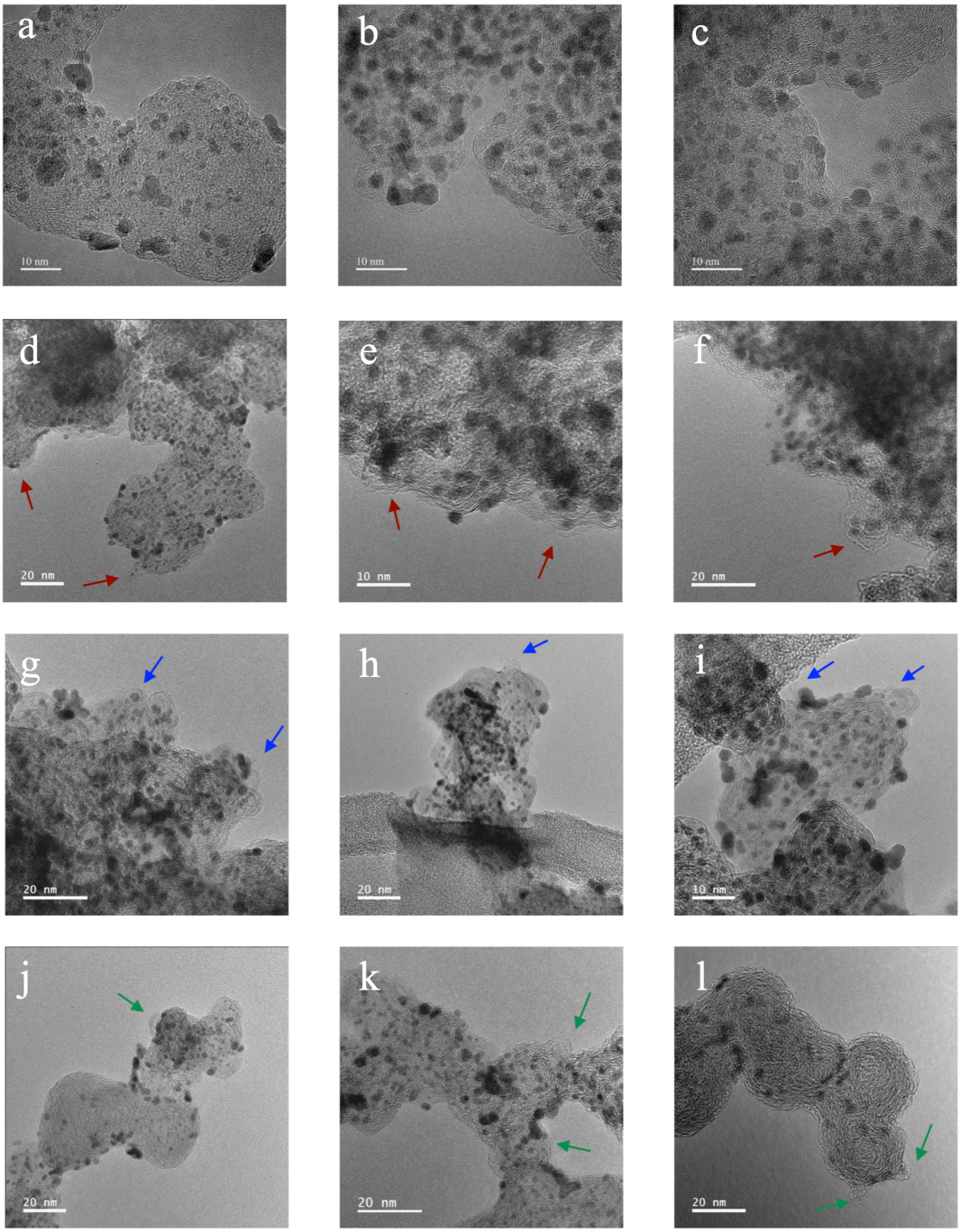


Figure 3-23 TEM images of a, b, c) Baseline (pristine) 40 wt. % Pt/C obtained from Fuel Cell Store, IL-modified Pt/C catalysts with d, e, f) Pt/C-($[C_2mim]^+[NTf_2]^-$), g, h, i) Pt/C-($[C_4mim]^+[NTf_2]^-$), and j, k, l) Pt/C-($[C_4dmim]^+[NTf_2]^-$). Arrows show the ionic liquids lumps.

### 3.5.2 Physical Characterization of IL-modified Samples

This study is focused on three types of ILs: 1-ethyl-3-methylimidazolium bis(trifluoromethylsulfonyl)imide ($[C_2mim]^+[NTf_2]^-$), 1-butyl-3-methylimidazolium bis(trifluoromethylsulfonyl)imide ($[C_4mim]^+[NTf_2]^-$), and 1-butyl-2,3-dimethylimidazolium bis(trifluoromethylsulfonyl)imide ($[C_4dmim]^+$ $[NTf_2]^-$). These imidazolium-derived ILs were selected because of their favorable ionicity, transport properties, stability. The anion structure for all three ILs is the same, but the cation is varied with the length of the alkyl chain. The difference between 1-butyl-3-methylimidazolium bis(trifluoromethylsulfonyl)imide and 1-butyl-2,3-dimethylimidazolium bis(trifluoromethylsulfonyl)imide is that the latter one has an additional methyl group in cation chemical structure. Here we want to compare the effect of alkyl chain length and the additional anchoring methyl group on the physical and electrochemical properties of the catalyst. Figure 3-1b, c, d, e, and 3-23 show the TEM images of HSA Ketjenblack Pt/C catalysts modified with these three ILs. Figure a demonstrates the nitrogen physisorption isotherms for baseline Pt/C and all IL-modified samples with IL/C of 1.28, at 77 K.

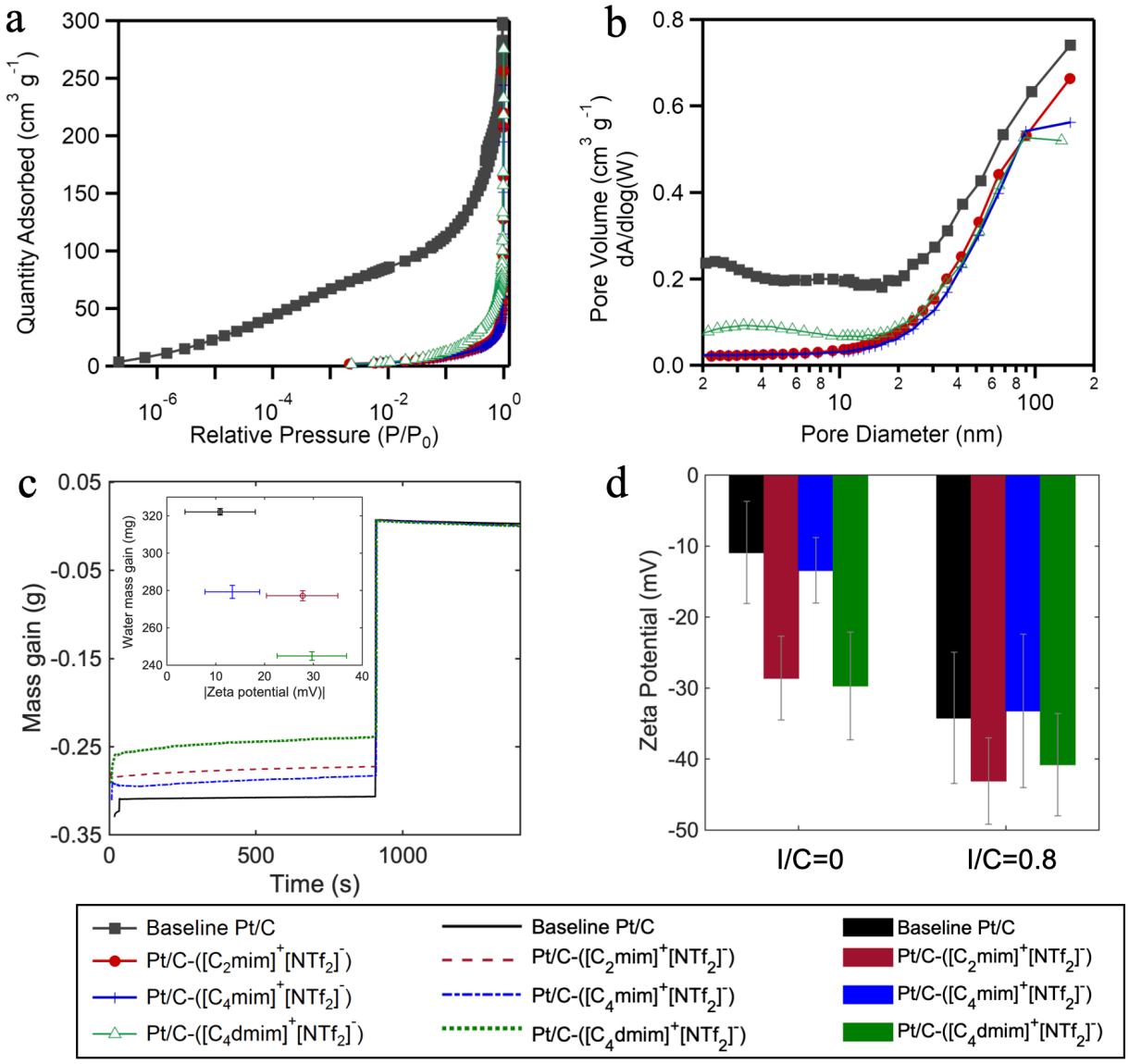


Figure 3-24 a,b) Nitrogen physisorption at 77 K, c) mass evolution of catalyst layers containing various ILs with IL/C ratio of 1.28 measured using capillary penetration method,. d) zeta potential measurements for pristine and IL-modified Pt/C with and without Nafion.

Unlike Pt/C baseline isotherm with a significant nitrogen uptake of ~100 cm$^3$ g$^{-1}$, all three IL-modified samples showed near zero nitrogen uptake at relative pressure below 0.01 (p/p0<0.01).

However, at high relative pressure (p/p0>0.9), their sorption isotherm curves showed similar shape to that of the pristine Pt/C sample as indicated in Figure 3-24a. As illustrated by the log-scale isotherm in Figure 2a, the nitrogen uptake starting points for IL-modified samples were around 0.01 $P/P_0$, indicating a complete filling or blocking of sub-micropores below 1nm. Pore size distribution as a function of pore diameter is shown in Figure 4b in order to assess the filling degree and IL coverage of the IL-containing Pt/C powders. For pores with diameter above 50 nm, almost no difference was observed between the pore volume of the baseline and three IL-modified samples indicating that the macropores of the modified powders are not filled with ILs. For pores between 2 nm to 50 nm, the pore volume decreased at least 50% showing that all IL molecules have partially filled mesopores. On the other hand, over 90% drop in the pore volume is observed for micropores between 1nm and 2nm indicating that the micropores are fully impregnated with ILs. This is in agreement with the significantly reduced nitrogen uptake below 0.2 $P/P_0$ indicated in Figure 2a. For the pore size between 2 nm and 20 nm, Pt/C-($[C_4dmim]^+[NTf2]^-$) samples showed non-negligible difference as compared to the other two IL-modified samples (Figure 3-24b), where its pore volume was still well below the Pt/C baseline but higher than that of its Pt/C-($[C_2mim]^+[NTf2]^-$) and -($[C_4mim]^+[NTf2]^-$) counterparts. This is partially due to the more complex structure of the $[C_4dmim]^+$, as it has both butyl and methyl cationic chains, higher free volume, and less packing of the molecules in the pores as a result. For interface modification in this work, the small mesopores are of more relevance as Pt most likely cannot be deposited into micropores and the ionomer cannot access small mesopores below <20 nm. From BET observations and TEM images in Figure 3-23, one can conclude that most of the Pt nanoparticles were well covered by the ILs.

Figure 3c shows the time evolution of water mass gain for baseline and IL-modified Pt/C coated films. By comparing the amount of water absorbed by the samples during the first 900s while they are immersed into the water, it can be concluded that baseline Pt/C coated catalyst layer shows the least amount of water uptake of about 18 mg compared to all IL-containing samples. On the other hand, all IL-containing catalyst layers show higher amount of water adsorption indicating that all Pt/C-IL-Nafion films are more hydrophilic compared to baseline. For instance, Pt/C-($[C_4dmim]^+[NTf_2]^-$)-Nafion catalyst layer has the highest water uptake amount of all (57 mg); hence, it is the most hydrophilic catalyst layer. Here we can illustrate with a schematic the potential intramolecular interactions between the IL molecules and Nafion domains (Figure 3-25). IL molecules are prone to induce a hydrophobic microenvironment that repels the $SO_3^-$ groups of Nafion to the outer surface resulting in more water absorption to the catalyst layer. Therefore, one can assume that the more hydrophobic the IL molecules are, the more hydrophilic the catalyst layer together with the Nafion would be.

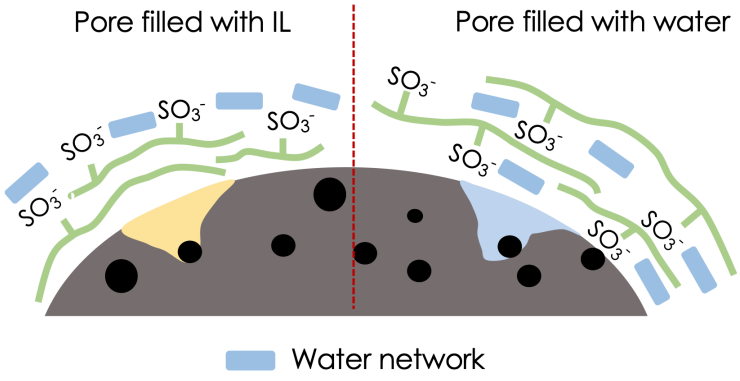


Figure 3-25 Nafion orientation near pores filled with IL vs. water.

External contact angles shown in Table 3-3 were calculated using Wilhelmy equation and sudden increase in the water mass gain after each sample was removed from the water ($\Delta mg$). The details

of experiment can be found in the Materials and Methods section of this paper. Pt/C-([$C_4$dmim]$^+$[$NTf_2$]$^-$)-Nafion film exhibited the smallest external contact angle of 137° and the highest amount of water uptake of 57 mg among all IL-containing samples. This indicates that ([$C_4$dmim]$^+$[$NTf_2$]$^-$) IL molecule itself is the most hydrophobic IL of all three and induced the strongest electrostatic repulsion on $SO_3^-$ groups of Nafion to reorient to the outer surface.

Table 3-3 Water uptake and external contact angel catalyst layers containing various ILs with IL/C ratio of 1.28 measured by Krüss tensiometer.

| **Sample** | Water uptake During first 900 s (mg) | $\Delta mg$ at 900s (mg) | External contact angel |
|---|---|---|---|
| **Pt/C-Nafion** | 18.2±5.1 | 322.2±1.8 | 164.3±1.8 |
| **Pt/C-([$C_2$mim]$^+$[$NTf_2$]$^-$)-Nafion** | 34.2±5.8 | 277.2±2.7 | 147.3±0.9 |
| **Pt/C-([$C_4$mim]$^+$[$NTf_2$]$^-$)-Nafion** | 33.1±3.4 | 279.3±3.5 | 148.0±3.3 |
| **Pt/C-([$C_4$dmim]$^+$[$NTf_2$]$^-$)-Nafion** | 57.2±6.8 | 244.9±2.3 | 136.8±0.7 |

These results are in agreement with zeta potential measurements in which hydrophobic interactions between the IL molecules and Nafion's PTFE backbone possibly dictate the conformational structure of the Nafion polymer chains. A stronger electrostatic repulsion between the molecules of ILs and Nafion's PTFE backbone results in a higher local charge density at the interface, and larger zeta potential (Figure 3c and 3-23d). From tensiometry results, we observed that Pt/C-([$C_4$mim]$^+$[$NTf_2$]$^-$)-Nafion catalyst layer has the largest external contact angel of 148° and the least water uptake of about 33 mg; therefore, it is the most hydrophobic catalyst layer compared to the other two IL-containing catalyst layers. Hence, ([$C_4$mim]$^+$[$NTf_2$]$^-$) IL molecule itself induces the least hydrophobic microenvironment compared to the other two ILs and has the smallest electrostatic repulsion with Nafion chains confirmed by zeta potential measurements.

Figure 3d and Table 3-4 represent the zeta potential of the suspensions containing Pt/C and IL-modified Pt/C in water/IPA solutions with 51 wt.% water content in presence of Nafion and without Nafion.

Table 3-4 Zeta potentials measurements for pristine and IL-modified Pt/C with and without Nafion.

| Sample | Zeta potential (mV) | Sample | Zeta potential (mV) |
|---|---|---|---|
| **Pt/C** | -10.9±7.2 | **Pt/C + Nafion** | -34.2±11.3 |
| **Pt/C-($[C_2mim]^+[NTf_2]^-$)** | -27.8±7.4 | **Pt/C-($[C_2mim]^+[NTf_2]^-$) + Nafion** | -43.1±7.1 |
| **Pt/C-($[C_4mim]^+[NTf_2]^-$)** | -13.4±5.6 | **Pt/C-($[C_4mim]^+[NTf_2]^-$) + Nafion** | -33.2±12.4 |
| **Pt/C-($[C_4dmim]^+[NTf_2]^-$)** | -29.7±7.1 | **Pt/C-($[C_4dmim]^+[NTf_2]^-$) + Nafion** | -40.8±7.2 |

Both groups of samples (with and without Nafion), exhibit similar trend with higher negative zeta potential when ILs are introduced to the system because of their higher ionic strength, specifically in the case of Pt/C-($[C_2mim]^+[NTf_2]^-$) and Pt/C-($[C_4dmim]^+[NTf_2]^-$). Generally speaking, a zeta potential smaller than the agglomeration threshold, $|\xi| < 15mV$, indicates the instability of the nanoparticles, which was only observed for pristine Pt/C suspension[118] without Nafion. Impregnating the carbon support with IL, significantly increased the absolute value of zeta potential. This indicates that ILs stabilized the Pt/C suspension and prevented it from agglomeration. Because ILs are charged, the electrostatic repulsion between Pt/C with ILs will be stronger than for pristine Pt/C [119]. Water uptake and zeta potential for Pt/C with ILs scale linearly. Pt/C catalyst layer has the least water uptake and least absolute value of zeta potential (-11 mV), whereas Pt/C-($[C_4dmim]^+[NTf_2]^-$) has the largest water uptake and the largest absolute value of zeta potential (-29 mV). When Nafion was added, zeta potential values for all the samples increased in absolute value to the range of -32 to -44 mV. Since the concentration of Nafion was

high, I/C of 0.8, the electrostatic interactions between the Nafion chains can also help promote aggregate structure and higher local surface charge density[120]. Consequently, larger negative zeta potential was observed for Nafion-containing inks.

### 3.5.3 RDE Prescreening and IL/C Ratio Optimization in MEA

Baseline and IL-modified Pt/C inks were prepared with optimized amount of IPA and water, Nafion/C and IL/C ratio of 51 wt. %, 0.3 and 2.56, respectively. Catalyst films were then deposited with the procedure described Materials and Methods section (3.4.3) and final Pt loading of 40μg/cm$^2_{geo}$. The electrochemical properties of all the catalyst layer films are provided in Table 3-5. Cyclic voltammograms of baseline and IL-modified Pt/C samples in Figure -26a showed no extra faradaic processes other than those generally happening on Pt/C, with HUPD peak observed between 0 and 0.4 V vs. RHE, and surface-oxygenated species (OHad and $O_{ad}$) beyond 0.6 V vs. RHE. By the addition of all three ILs to the Pt/C catalyst, the ECSA decreased because of blocking effect of ILs by their selective occupation of the Pt active sites, competition adsorption of their ions with hydrogen, and suppression of Pt-H bonding strength due to the direct ligand effect [84,97,121,103]. The ECSA loss observed for Pt/C-($[C_2mim]^+[NTf_2]^-$), Pt/C-($[C_4mim]^+[NTf_2]^-$), and Pt/C-($[C_4dmim]^+[NTf_2]^-$) were 5.5 %, 9.2 %, and 8.3%, respectively. The onset potential of the Pt-oxide formation was also shifted to higher potentials and the area under $OH_{ad}$ and $O_{ad}$ peak decreased indicating that the formation of oxygenated species was suppressed resulting in lower coverage of Pt surface. IL molecules potentially protected the Pt active sites from being occupied by non-reacting oxygenated species; thus, facilitating the ORR kinetics as strong Pt-O bonding is known to slow ORR [112]. The suppression of Pt-oxide formation was more dominant when Pt/C-

($[C_4dmim]^+[NTf_2]^-$) was utilized, as it showed super hydrophobic properties and repelled water molecules from Pt active sites protecting them from being oxidized [104]. In addition, it has been shown that ORR activity enhancement using ILs is also attributed to the interfacial hydrogen-bonding between IL's cation and adsorbed intermediate oxygenated species of ORR ($O_{ad}$ and $OH_{ad}$). In this study, $N\text{-}H^+$ bonds of the imidazolium cation form hydrogen-bonding with $OH_{ad}$; therefore, it enables faster proton tunneling from IL to Pt active sites through intermediate species ($N\text{-}H^+ + OH_{ad} + e^- \rightarrow H_2O + N$). Hydrogen-bonding structure can regulate the exchange current density of ORR and reaction rate constant based on the vibrational features of the intermediates[122].

Polarization curves performed at room temperature are also displayed in Figure -26b. Only Pt/C-($[C_4mim]^+[NTf_2]^-$) catalyst film demonstrated slightly improved ORR kinetics, as the half-wave potential (E1/2) is positively shifted toward higher potential. Mass and specific activities at 0.9 V improved by 6.1 % and 8.3 % compared to baseline Pt/C, respectively. There have been extensive investigations in the literature to show ORR improvement in IL-modified Pt/C catalysts using RDE[94]. Huang et al.[97] indicated MA enhancement factor of about 1.2 for both [MTBD][beti] and $[MTBD][C_4F_9SO_3]$-modified high surface area Pt/C. These samples improved SA by a factor of 1.4 and 1.7. The degree of performance enhancement is in a great agreement with our observations in which the MA and SA enhancement factors for high surface area Pt/C-($[C_4mim]^+[NTf_2]^-$) were 1.2 and 1.7, respectively. Zhang et al.[104] explored the ORR enhancement on low surface area Pt/C using imidazolium based ILs and obtained MA enhancement factor of about 3 for their best performing IL that has similar chemical structure to ($[C_4mim]^+[NTf_2]^-$) and has the same cationic alkyl chain length. Yan et. al [98] also reported up to three-fold enhancement in MA and SA of Pt/C catalyst by replacing Nafion with a poly(ionic liquid) in which the IL segment acts as a proton conductor. Figure -26c compares the Nyquist plots of baseline and IL-modified Pt/C catalyst

layers. The linear portion of the Nyquist plot data at intermediate frequencies is used for the calculation of the effective catalyst layer protonic resistance. The fitted line's intercept on the x-axis is considered to be $R_{H^+}/3$ [123]. Baseline Pt/C (in presence of Nafion) showed a noticeably higher proton diffusion resistance of 3.27 $\Omega.cm^2$ when compared to the catalyst layers with the mixture of Nafion and IL. The values for $R_{H^+}$ can be found in Table 3-5. Specifically, Pt/C-($[C_2mim]^+[NTf_2]^-$) and Pt/C-($[C_4mim]^+[NTf_2]^-$) expressed superior proton conductivity making them a great candidate for investigating the role of proton conduction in improving ORR catalytic activity when nanoconfinements are induced by ILs.

Table 3-5 Electrochemical properties of the Pt/C and Pt/C-IL samples evaluated by RDE.

| | **Baseline Pt/C** | **Pt/C-($[C_2mim]^+[NTf_2]^-$)** | **Pt/C-($[C_4mim]^+[NTf_2]^-$)** | **Pt/C-($[C_4dmim]^+[NTf_2]^-$)** |
|---|---|---|---|---|
| **Mass Activity ($A\ g^{-1}_{Pt}$)** | 280 | 149 | 297 | 122 |
| **Specific Activity ($\mu A\ cm^2_{Pt}$)** | 326 | 196 | 353 | 148 |
| **ECSA ($m^2\ g^{-1}$)** | 86 | 81.3 | 78.1 | 78.9 |
| **$R_{H^+}$ ($\Omega\ cm^2$)** | 3.27 | 0.39 | 0.48 | 2.34 |

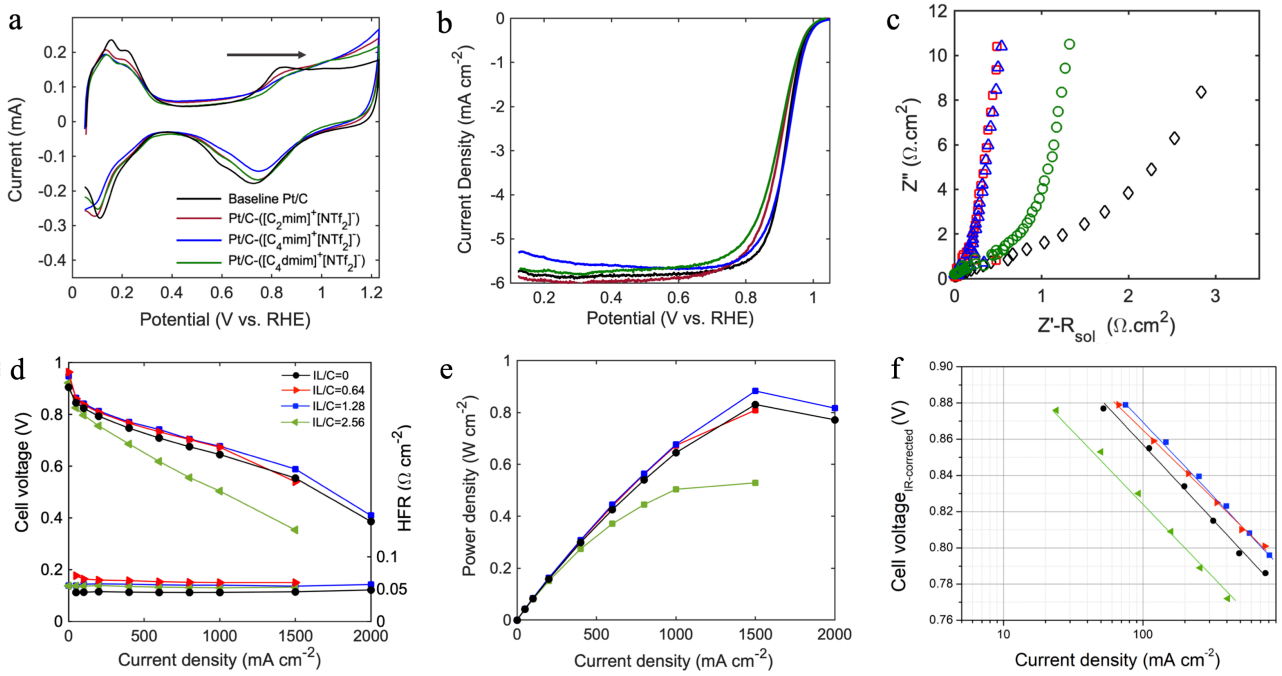


Figure 3-26 Comparison of electrochemical characterization for baseline Pt/C and imidazolium modified Pt/C systems a) Cyclic voltammograms in $N_2$-saturated 0.1 M $HClO_4$, b) Polarization activity in $O_2$-saturated 0.1 M $HClO_4$ at a rotation speed of 1600 rpm. c) Nyquist plots of impedance spectra under $N_2$-saturated 0.1 M $HClO_4$ for Pt/C-Nafion and Pt/C-IL-Nafion catalyst layers. Electrochemical characterization for MEAs containing various IL/C ratios evaluated at 80°C and 100% RH: d) $H_2$/air polarization curves and e) power density obtained at 150 $kPa_{abs}$ total pressure, f) $H_2/O_2$ Tafel plots measured at 150 $kPa_{abs}$ total pressure in 5 $cm^2$ differential cells, cathode: HSA Pt/C or HSA Pt/C-IL, anode: LSA Pt/C.

As Pt/C-($[C_4mim]^+[NTf_2]^-$) with IL/C ratio of 2.56 expressed a potential in improving the catalytic activity in RDE level, we introduced various loadings of this IL to the catalyst layer and tested them in fuel cell hardware in order to optimize MEA level performance. In order to prepare the ink for MEA fabrication, impregnated powders were redispersed in the Nafion solution in water and IPA. The ink suspension was then coated, dried, and hot-pressed on Nafion membrane for

MEA manufacture as described in Materials and Methods section 3.4.4. To investigate the Pt/C-ILs interface evolution during MEA preparation, we performed a complementary experiment.

### 3.5.3.1 Evolution of Pt/C-IL Interface During MEA Fabrication Procedure

100 mg of pristine Pt/C and all three Pt/C-IL powders were mixed with 2 ml of IPA and DI water and ultrasonicated for 30 mins. 100 mg of IL-impregnated powder with IL to C ration of 1.28 contains about 43.75 mg of IL. In the next step, we centrifuged the suspensions at 30000 rpm for 15 mins until the powder separated completely from the solvents as can be seen in Figure 3-27. Solvents were then removed from the centrifuge tubes and remaining powders dried overnight. The weight difference between the original IL-impregnated powders and the ones after the procedure can be attributed to the ILs that dissolved in the solution as all three ILs are soluble in the mixture of IPA and water.

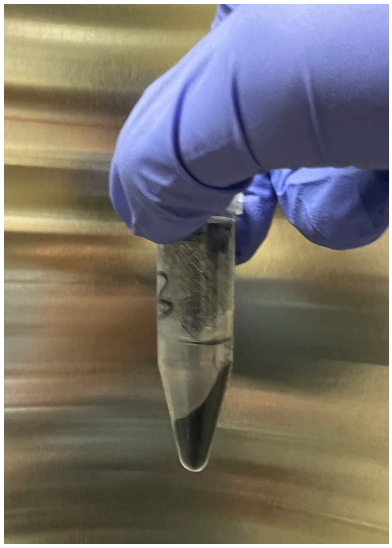

Figure 3-27 Separation of Pt/C-IL powder from solution after centrifuge.

This weight difference for Pt/C-($[C_2mim]^+[NTf_2]^-$), Pt/C-($[C_4mim]^+[NTf_2]^-$), and Pt/C-($[C_4dmim]^+[NTf_2]^-$) powders, were 18.1, 22.1, and 24.8 mg, respectively. This procedure was also

performed on a control sample in which we saw about 10.6 mg weight loss. This loss is due to the potential error in the experiment as we remove the separated solution from the precipitated powder. Therefore, the weight of Pt/C-($[C_2mim]^+[NTf_2]^-$), Pt/C-($[C_4mim]^+[NTf_2]^-$), and Pt/C-($[C_4dmim]^+[NTf_2]^-$) powders decreased about 17, 26, and 32 wt.% that is attributed solely to the IL dissolved in the IPA and water mixture and got separated from the powder. This means that a part of the ILs in the impregnated powders redispersed in the solution and redeposited together with Nafion. We believe, IL molecules on catalyst surface, in the macropores and bigger mesopores would dissolve faster compared to the ones in the smaller mesopores and micropores. This observation is in great agreement with the IL molecules chemical structures and BET results. As can be seen, the ILs dissolution in IPA and water increases with elongation in alkyl chain length. For example, ($[C_4dmim]^+[NTf_2]^-$) showed the highest dissolution (about 30wt.%) in IPA and water and has the most complex structure of all three ILs, as it has both butyl and methyl cationic chains, and less packing of the molecules in the pores. Therefore, the more complex the structure of IL is, the less it fills the pores and easily get redispersed in the solution. We believe depending on the IL chemical structure and pore filling degree, a portion of the impregnated IL in the catalyst powder would redissolve in ink's Nafion solution as IL is soluble in the mixture of water and IPA. Then, it deposits along with Nafion during coating and drying. One can assume that IL molecules on the surface, in the macropores and larger mesopores would dissolve faster in the Nafion solution compared to the ones packed in the micropores and smaller mesopores. Figure -26d and Figure -26e represent the polarization curve and power density of the MEAs with various loadings of ($[C_4mim]^+[NTf_2]^-$). The electrochemical properties of the MEAs are summarized in Table 3-6.

Table 3-6 Electrochemical properties of Pt/C-IL MEAs containing various loadings of IL.

| | **IL/C=0** | **IL/C=0.64** | **IL/C=1.28** | **IL/C=2.56** |
|---|---|---|---|---|
| **OCV (V)** | 0.905 | 0.963 | 0.948 | 0.922 |
| **Peak power density ($W\ cm^{-2}$)** | 0.831 | 0.809 | 0.909 | 0.566 |
| **Mass Activity at 0.9 V ($A\ g^{-1}_{Pt}$)** | 288 | 173 | 347 | 110 |
| **Specific Activity at 0.9 V ($\mu A\ cm^{2}_{Pt}$)** | 399 | 509 | 697 | 491 |
| **ECSA ($m^2\ g^{-1}$)** | 72.1 | 60.6 | 49.7 | 22.4 |
| **Local $O_2$ mass transport resistance ($s\ cm^{-1}$)** | 0.175 | 0.256 | 0.268 | 0.258 |

In order to reach the optimum performance, MEA with IL/C ratio of 2.56 had to undergo 8 voltage recovery cycles, where the cell was held at low potential and oversaturated condition (150% RH) to remove excess surface-blocking species including sulfates. The maximum current density obtained from this cell was only 1.5 A $cm^{-2}$ confirming there was a thick layer of IL causing 69% ECSA loss and a high mass transport resistance at high current densities. Although the SA at 0.9 V increased compared to the baseline, the MA was only 110 A $g_{Pt}^{-1}$. By cutting the amount of IL into half, IL/C ratio of 1.28, MEA showed enhanced performance across all current densities, with optimum peak power density of 0.909 W $cm^{-2}$. MA and SA obtained from the Tafel plot at 0.9 V in Figure -26f increased to 347 A $g_{Pt}^{-1}$ and 697 μA $cm^{2}_{Pt}$, respectively. The amount of ($[C_4mim]^+[NTf_2]^-$) was then reduced to half, causing the MA and SA at 0.9 V drop to 173 A $g_{Pt}^{-1}$ and 509 μA $cm^{2}_{Pt}$. Although the ECSA loss in this case was only 16%, the amount of IL was insufficient to improve proton conductivity efficiently in the smaller mesopores, specifically at

high current densities where the cell current was limited to a maximum of 1.5 A $cm^{-2}$ as a result. All three IL-containing MEAs showed similar local oxygen mass transport resistance within the range of 0.261±0.006 s $cm^{-1}$ expressing that local mass transport resistance depends on the chemical nature of the IL rather than its loading (Table 3-5 and Figure 3-28).

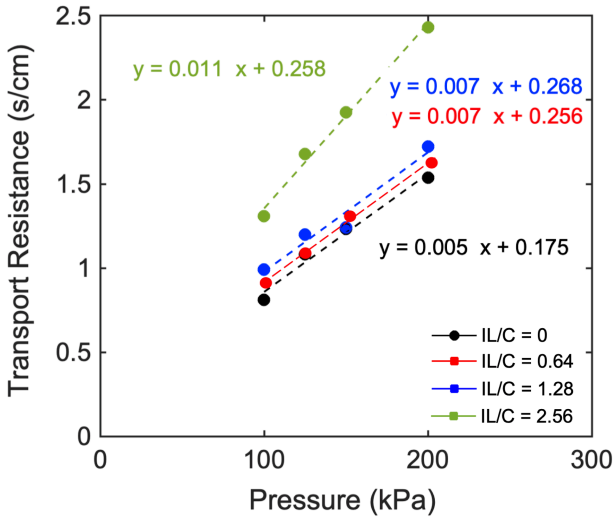


Figure 3-28 Mass transport resistance plots of Pt/C and Pt/C-($[C_4mim]^+[NTf_2]^-$) with various loadings of IL obtained at 75% RH, at 100, 125, 150, 200 $kPa_{abs}$ total pressure in 5 $cm^2$ differential cells.

The reason we believe IL/C ratio of 1.28 is the optimum ratio for MEA fabrication is that based on our study in section 2.2.1, less than 30% of the IL is covering the surface or is in the bigger pores. Therefore, about 70% of the IL is deposited in the micro and smaller mesopores. This portion of IL would not dissolve as fast as the ones on the surface and would stay in the smaller pores facilitating proton transfer. One the other hand, at high IL loadings (IL/C=2.56), there is a layer of IL covering the whole surface that would redeposit with Nafion in the catalyst layer causing high ionic resistance.

### 3.5.4 In-situ MEA Characterization of Baseline Pt/C vs IL-modified catalysts

Figure 3-29, Figure 3-30 and Table 3-7 show the electrochemical characteristics of baseline Pt/C and all three IL-modified MEAs with optimized IL/C ratio of 1.28. Figure 3-29a displays the optimal polarization curves obtained after two and three voltage recovery cycles for baseline Pt/C and IL-modified MEAs, respectively. Pt/C-($[C_4mim]^+[NTf_2]^-$) showed a significant improvement across all current densities, while MEA containing ($[C_2mim]^+[NTf_2]^-$) showed similar polarization curve to the baseline with slightly enhanced potential in current densities between 400 and 1500 mA $cm^{-2}$. Neither Pt/C-($[C_2mim]^+[NTf_2]^-$) nor Pt/C-($[C_4dmim]^+[NTf_2]^-$) promoted the performance in kinetic and mass transport-limited regions. Additionally, all the IL-containing MEAs showed higher OCV than that of the baseline which can be attributed to the exposure of Pt to ILs' imidazolium ions, structural changes of the electric double layer (EDL), interfacial electron exchange between IL and the surface of carbon that led to positive shift in the OCV [94,124,125]. Furthermore, Pt/C-($[C_2mim]^+[NTf_2]^-$) and Pt/C-($[C_4mim]^+[NTf_2]^-$) MEAs reached peak power densities of 0.856 and 0.909 W $cm^{-2}$ at 61.2% and 63.9% voltage efficiencies, while baseline's peak power density was only 0.831 (Figure 3-29b and Table 3-7). As displayed in Figure 3-29c, cyclic voltammograms confirmed that the presence of all three IL-layers protect the Pt surface from formation of non-reactive oxygenated species by shifting the peak to higher potentials. ECSA loss for modified catalysts in MEA-level measurement was 26.8%, 31.1%, 48.3% for Pt/C-($[C_2mim]^+[NTf_2]^-$), Pt/C-($[C_4mim]^+[NTf_2]^-$), and Pt/C-($[C_4dmim]^+[NTf_2]^-$), respectively. As discussed before in the RDE section, this could be related to the molecular structure of the ILs and the interaction of the cationic alkyl chain with Pt terrace site. In correlation with previously reported observations [104], increase in the number of alkyl chains, as well as their length can increase the interaction with Pt sites. In addition, MEA level measurements revealed much higher ECSA

losses compared to RDE set-up. RDE experiments are carried out in aqueous environment in which all the Pt within the pores is accessible by protons through adsorbed water films. On the other hand, ECSA measurement in MEAs occur at 100% RH where IL molecules are expected to have different interactions with Pt compared to fully aqueous environment.

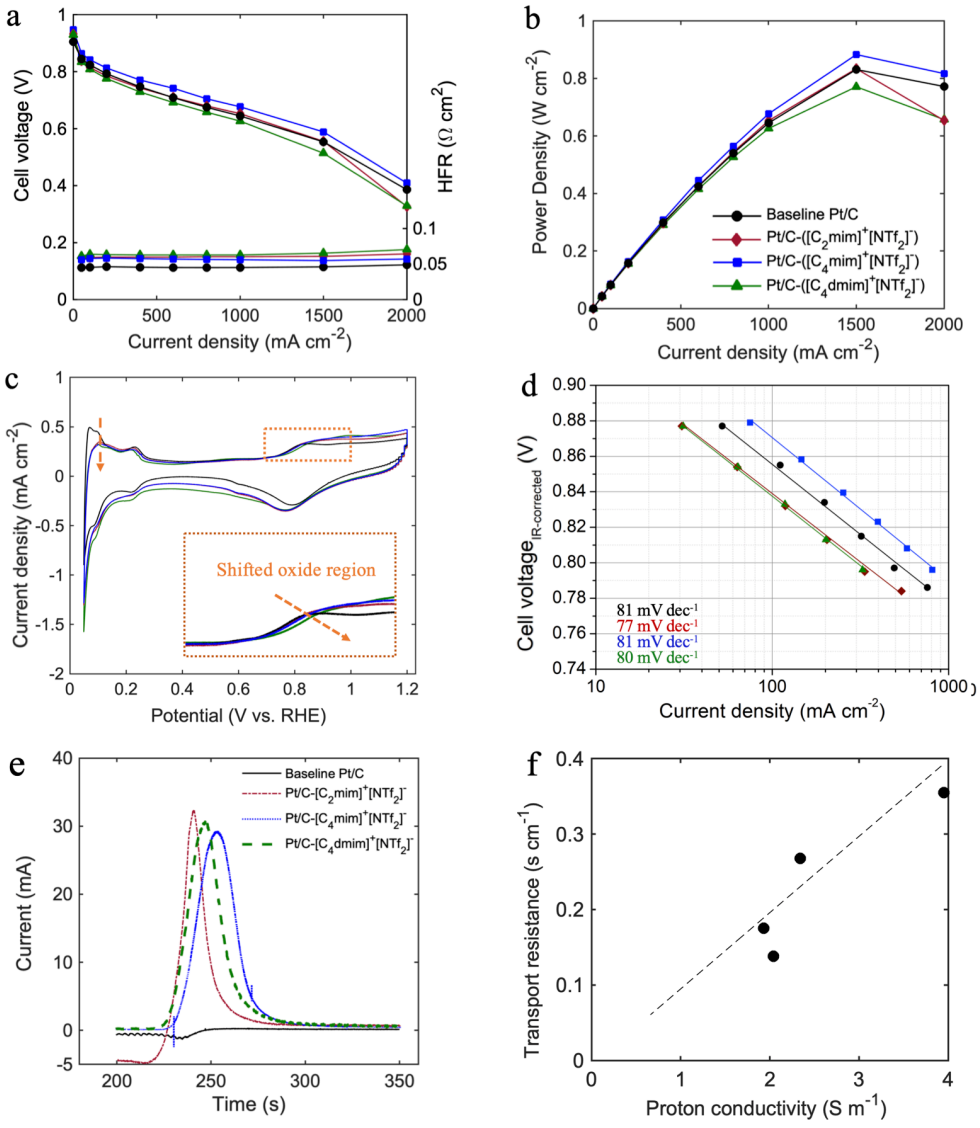


Figure 3-29 Electrochemical characterization of IL-containing MEAs obtained after three voltage recovery cycles vs. baseline Pt/C after two voltage recovery cycles evaluated at 80°C and 100% RH: a) $H_2$/air polarization curves, b) power density at 150 $kPa_{abs}$ total pressure, c) cyclic

voltammograms recorded in $H_2/N_2$ and 100 $kPa_{abs}$ total pressure, d) $H_2/O_2$ Tafel plots at 150 $kPa_{abs}$ total pressure, e) CO-displacement at 0.35 V at 100 $kPa_{abs}$ and 40°C, f) Correlation between local oxygen mass transport resistance and proton conductivity in 5 $cm^2$ differential cells, cathode: HSA Pt/C or HSA Pt/C-IL, anode: LSA Pt/C.

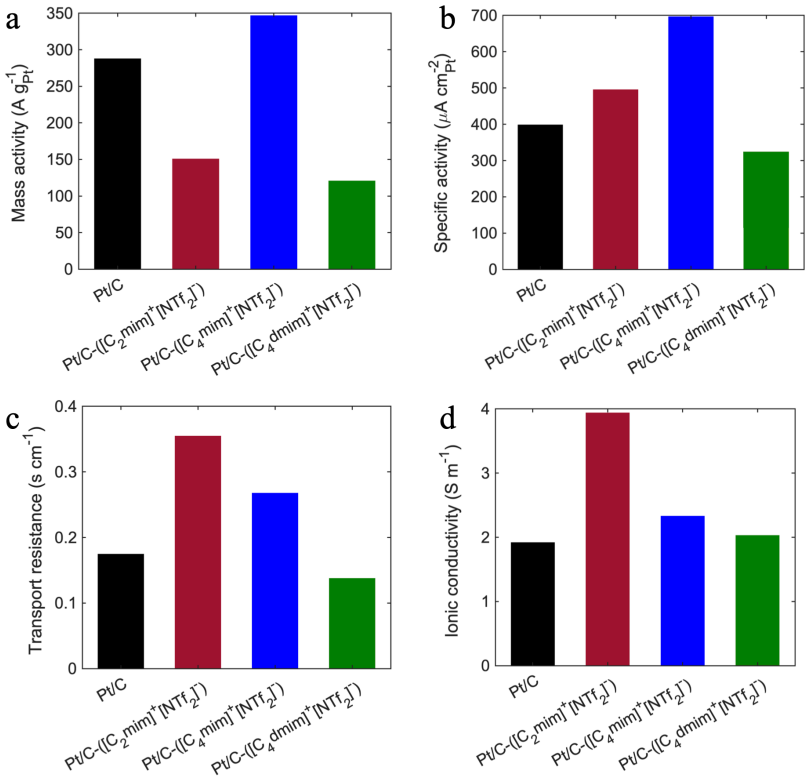


Figure 3-30 Electrochemical characterization of IL-containing MEAs obtained after three voltage recovery cycles vs. baseline Pt/C obtained after two voltage recovery cycles evaluated at 80°C: a) mass and b) specific activities at 0.9 V, 150 $kPa_{abs}$ and 100% RH, and c) local oxygen transport resistance measured at 75% RH, and d) ionic conductivity at 100% RH.

Table 3-7 Electrochemical properties of baseline Pt/C MEA obtained after two voltage recovery cycles and Pt/C-IL MEAs obtained after three voltage recovery cycles in fuel cell set-up.

| | **Baseline Pt/C** | **Pt/C-($[C_2mim]^+[NTf_2]^-$)** | **Pt/C-($[C_4mim]^+[NTf_2]^-$)** | **Pt/C-($[C_4dmim]^+[NTf_2]^-$)** |
|---|---|---|---|---|
| **OCV (V)** | 0.905 | 0.933 | 0.948 | 0.929 |
| **Cell potential @ 0.8 A $cm^{-2}$** | 0.675 | 0.680 | 0.705 | 0.658 |
| **Peak power density (W $cm^{-2}$)** | 0.831 | 0.856 | 0.909 | 0.804 |
| **Mass Activity at 0.9 V (A $g^{-1}_{Pt}$)** | 288 | 151 | 347 | 121 |
| **Specific Activity at 0.9 V (μA $cm^2_{Pt}$)** | 399 | 496 | 697 | 324 |
| **ECSA ($m^2$ $g^{-1}$)** | 72.1 | 52.8 | 49.7 | 37.3 |
| **Proton Conductivity (S $m^{-1}$)** | 1.93 | 3.95 | 2.34 | 2.04 |
| **Local $O_2$ mass transport resistance (s $cm^{-1}$)** | 0.175 | 0.355 | 0.268 | 0.138 |

The EIS data fitting at high frequencies (Figure 3-31) illustrates that Pt/C-($[C_2mim]^+[NTf_2]^-$) and Pt/C-($[C_4mim]^+[NTf_2]^-$) catalyst layers in the presence of Nafion have significantly enhanced

proton conductivity as high as 3.95 and 2.34 S $m^{-1}$, while Pt/C-($[C_4dmim]^+[NTf_2]^-$) shows similar proton conduction to the baseline (Figure 3-30d).

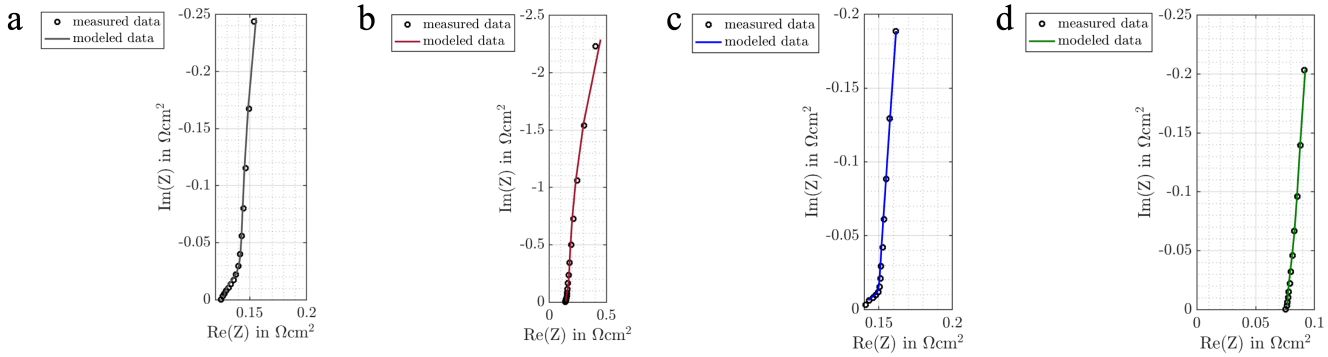


Figure 3-31 Nyquist plots measured at 80°C, 100% RH, and 100 $kPa_{abs}$ total pressure in 5 $cm^2$ differential cells for a) baseline Pt/C, b) Pt/C-($[C_2mim]^+[NTf_2]^-$), c) Pt/C-($[C_4mim]^+[NTf_2]^-$), d) Pt/C-($[C_4dmim]^+[NTf_2]^-$) MEAs.

Moreover, as it is summarized in Figure 3-30c and 3-30d, modified MEAs with $[C_2mim]^+[NTf_2]^-$ have ca. ×2 higher local oxygen mass transport resistance than that of baseline, which is offset by the enhanced high ionic conductivity (also ca. ×2 ) resulting in a similar polarization curve to the baseline except in the mass transport-limited region where oxygen mass transport resistance become more critical. The similar trend is also observed for Pt/C-($[C_4dmim]^+[NTf_2]^-$), where the lower ionic conductivity compared to the baseline is offset by the lower local oxygen mass transport resistance due to its lower filling degree. However, in this case, the notable loss in the active area is responsible for the significant drop in the catalytic activity as the MA obtained at 0.9 V decreased to 121 A $g_{Pt}^{-1}$ (Table 3-7 and Figure3-30a). Although ($[C_4dmim]^+[NTf_2]^-$) expressed the lowest transport resistance compared to all other samples and is more capable of suppressing Pt-oxide formation, the interplay of significant ECSA loss, lower ionic conductivity and filling degree, makes it insufficient in promoting catalyst ORR activity. Local oxygen mass transport

resistance for all four MEAs summarized in Figure 3-30c was obtained from y-intercept of mass transport resistance line as a function of total pressure presented in Figure 3-32. Mass and specific activities at 0.9 V summarized in Figure 3-30a and 3-30b were also calculated from Tafel plots presented in Figure 3-29d.

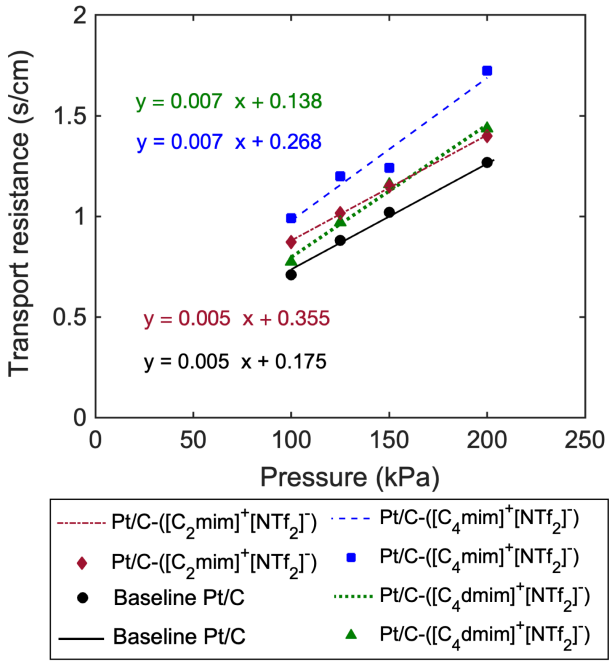


Figure 3-32 Mass transport resistance plots of Pt/C and Pt/C-IL MEAs obtained at 75% RH, at 100, 125, 150, 200 $kPa_{abs}$ total pressure in 5 $cm^2$ differential cells.

In contrast, Pt/C-($[C_4mim]^+[NTf_2]^-$) showed superior electrochemical properties that highlights the importance of how optimized molecular structure and induced hydrophobic nanoconfinement can alter the activity of the catalyst toward ORR. As illustrated in Figure 3-30a and 3-30b and Table 3-7, Pt/C-($[C_4mim]^+[NTf_2]^-$) showed enhanced mass activity and specific activity at 0.9 V of approx. 350 A $g_{Pt}^{-1}$ and 700 ($\mu A\ cm^2_{Pt}$) which is 20% and 75% higher than that of the baseline. As previously shown in this work, ($[C_4mim]^+[NTf_2]^-$) is capable of filling the pores sufficiently and its optimal hydrophobicity is effective enough to protect the Pt active sites from

Pt-oxides while the ECSA loss is only 31%. On the other hand, it can form a well-connected proton pathway with Nafion as the zeta potential measurement showed there is a small repulsion between Nafion chains and IL molecules. From the chemical structure point of view, enhancement in the ionic conductivity can also be attributed to an interplay of various mechanisms: i) $[NTf_2]^-$ serving as proton defects (hopping site) and carrier, ii) proton migration through Grotthuss mechanism as the conformational flexibility of $[NTf_2]^-$, distributed negative charge, parallel $\pi - \pi$ stacking in the structure of imidazolium facilitate the hydrogen-bonding formation between H atoms of the imidazolium ring and N and O atoms of the $[NTf_2]^-$. Furthermore, since ($[C_4mim]^+[NTf_2]^-$) induces a minimal hydrophobic microenvironment, it can still retain some extent of water near Pt active sites promoting the proton conduction via both Grotthuss and vehicular mechanisms in form of $H_3O^+$ [99,107,126,127,110] Figure 3-33 compares the polarization curves of Pt/C-($[C_4mim]^+[NTf_2]^-$) in wet (100% RH) and dry conditions (75%, 50%, 30% RH) vs the baseline Pt/C. Earlier study showed dramatic loss of performance for MEA with IL under dry conditions[105]. Here, we see overall good performance of IL-filled Pt/C but not as high compared to the baseline at dry conditions.

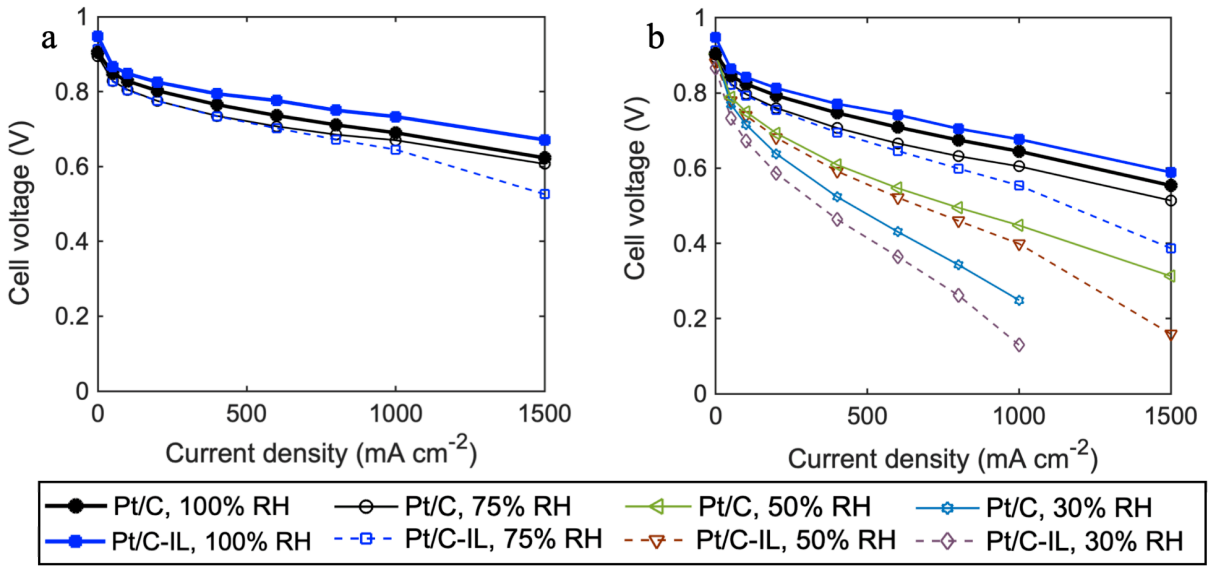


Figure 3-33 a) HFR-corrected $H_2$/air polarization curves of Pt/C and Pt/C-($[C_4mim]^+[NTf_2]^-$) at 75% and 100% RH and 150 $kPa_{abs}$ total pressure, b) $H_2$/air polarization curves of Pt/C and Pt/C-($[C_4mim]^+[NTf_2]^-$) measured at 100%, 75%, 50%, and 30% RH in 5 $cm^2$ differential cells.

At dry conditions for the baseline catalyst, most of Pt in contact with ionomer will be active and Pt inside the mesopores will not unless they are specifically engineered to condense water at these low RHs (30 and 50% RH). Since ionomer orientation near Pt with IL-filled layers is different, local hydrophobic environments that ILs induce are not favorable for performance in dry conditions. This is probably due to the fact that ILs' hydrophobic domains repel $SO_3^-$ groups and water molecules from IL|ionomer interface causing higher protonic resistance at the interface. Therefore, catalyst layers have to be further reengineered if dry operation is the target.

Another important observation shown by Figure 3-29e is the CO-displacement plots for the baseline and IL-modified Pt/C. Baseline catalyst layer shows a reduction peak when CO is introduced at 0.35 V indicating that CO is displacing $SO_3^-$ groups, as Pt is positively charged at this potential and $SO_3^-$ groups adsorb on positive surface. On the other hand, oxidation peak is

observed for all three catalyst layers with IL, indicating that CO is displacing a positive charge from the surface of Pt. This can be the imidazolium groups adsorbing on surface. Interestingly, XPS data summarized in Figure 3-34 and Table 3-8 showed no substantial chemical changes in Pt and Pt-oxide states after the ex-situ XPS CO dosing confirming that IL molecules had no adverse interactions with Pt surface. These ex-situ experiments were not performed under applied potentials and most likely Pt does not strongly interact with the imidazolium groups at OCV. However, under applied potentials in the in-situ environment this might not be the case. The interesting finding indicates that ILs may effectively prevent $SO_3^-$ groups adsorption onto the surface of Pt, adding to its catalytic activity. Figure 4f reveals that there is a tradeoff between the proton conductivity and local oxygen mass transport resistance as a higher proton conductivity comes at the expense of larger oxygen transport resistance. Therefore, based on the MEA design needs, an optimal point should be selected which was the case for MEA containing ($[C_4mim]^+[NTf_2]^-$) in this work.

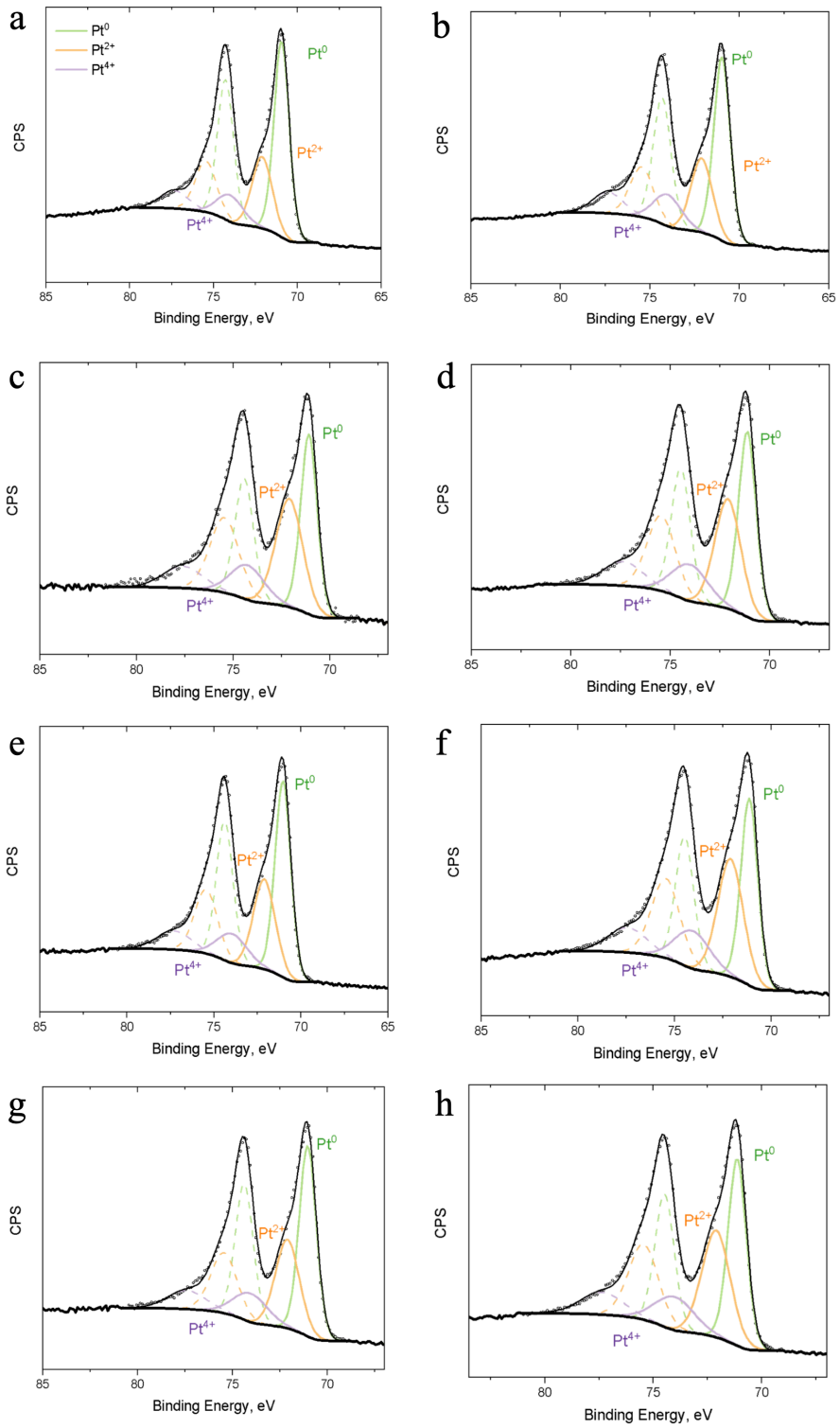
a
b
c
d
e
f
g
h
Pt0
Pt2+
Pt4+
CPS
Binding Energy, eV

Figure 3-34 XPS spectra of 40 wt. % Pt/C a) before CO introduction, b) after CO poisoning, IL-modified Pt/C catalysts including Pt/C-($[C_2mim]^+[NTf_2]^-$) c) before CO introduction, d) after CO-poisoning, Pt/C-($[C_4mim]^+[NTf_2]^-$), and j, k, l) Pt/C-($[C_4dmim]^+[NTf_2]^-$).

Table 3-8 Pt and Pt-oxides binding energies before and after introduction of CO.

| **%At. Con. (St.Dev.)** | | **$Pt^0$** | **$Pt^{2+}$** | **$Pt^{4+}$** |
|---|---|---|---|---|
| **Baseline Pt/C** | Before CO introduction | 58.6 (1.13) | 28.1 (1.34) | 13.3 (0.82) |
| | After CO poisoning | 55.3 (1.22) | 29.0 (1.25) | 15.7 (0.81) |
| **Pt/C-($[C_2mim]^+[NTf_2]^-$)** | Before CO introduction | 47.2 (4.66) | 38.5 (6.86) | 14.3 (2.61) |
| | After CO poisoning | 44.4 (3.35) | 38.1 (4.03) | 17.5 (2.25) |
| **Pt/C-($[C_4mim]^+[NTf_2]^-$)** | Before CO introduction | 52.5 (2.62) | 32.97 (4.08) | 14.57 (2.02) |
| | After CO poisoning | 42.3 (3.08) | 40.2 (4.02) | 17.5 (2.13) |
| **Pt/C-($[C_4dmim]^+[NTf_2]^-$)** | Before CO introduction | 51.4 (2.94) | 33.5 (5.23) | 15.1 (3.05) |
| | After CO poisoning | 44.4 (3.40) | 39.0 (4.06) | 16.6 (2.13) |

## 3.5.5 Durability Studies

In order to probe the degradation behavior of the modified catalysts, DOE-specified catalyst AST was conducted that involved load cycling in range of 0.6-0.95 V each for 3s and 30,000 cycles. Although HSA Ketjenblack Pt/C catalysts are generally electrochemically active due to the lower ionomer poisoning, they tend to lose their catalytic activity dramatically at 800 mA $cm^{-2}$ after only 30 h of accelerated testing[128]. Figure 3-35 and Table 3-9 show the evolution of electrochemical

properties for IL-containing MEAs versus baseline at the beginning of life (BOL) and end of life (EOL).

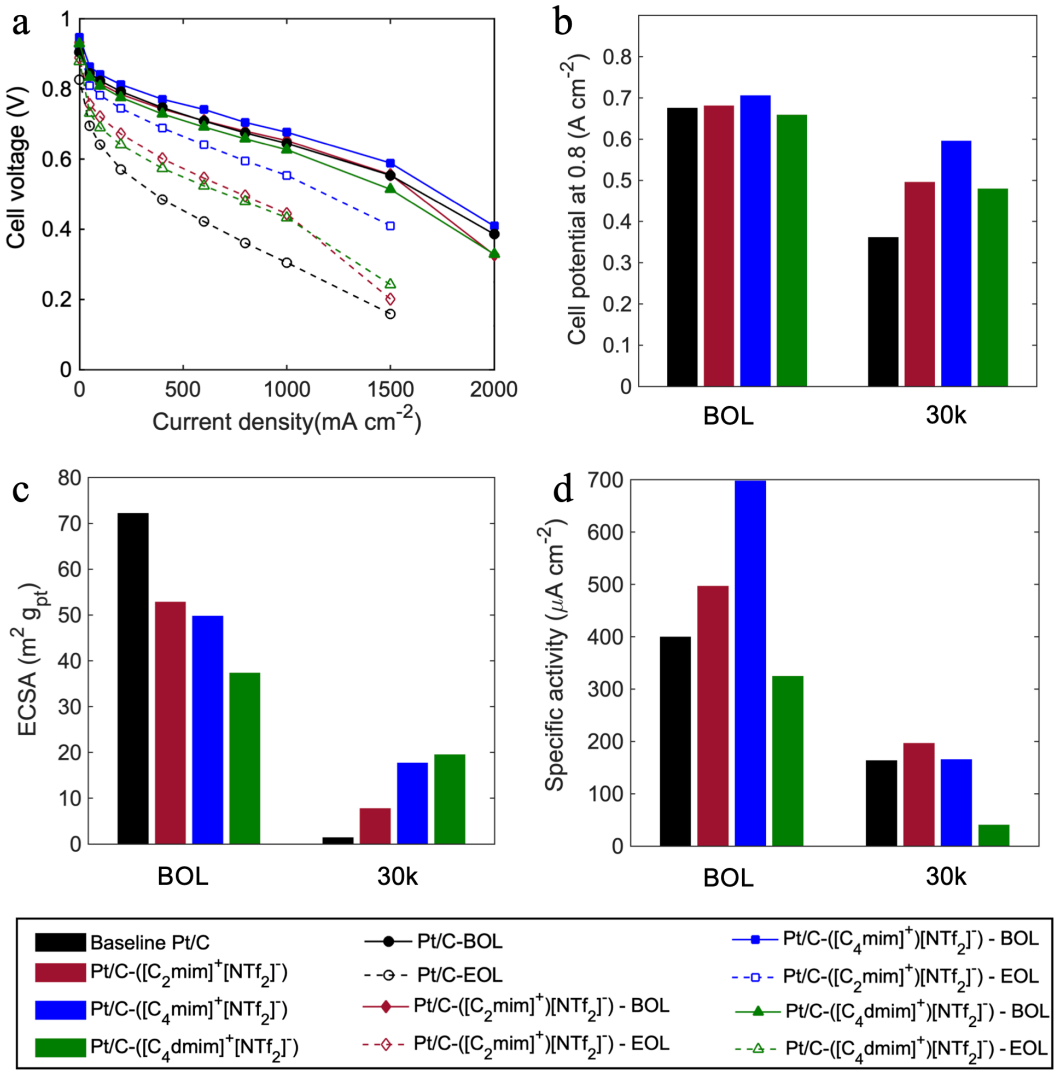


Figure 3-35 a) comparison of H2/air polarization curves at the beginning of life (BOL) and after 30,000 cycles for Pt/C baseline vs. Pt/C-($[C_2mim]^+[NTf_2]^-$), Pt/C-($[C_4mim]^+[NTf_2]^-$), and Pt/C-($[C_4dmim]^+[NTf_2]^-$) MEAs, comparison of b) cell potential at 0.8 A $cm^{-2}$, c) mass activities obtained at 0.9 V vs. RHE, and d) ECSA for all MEAs at BOL vs. EOL (after 30k cycles). BOL electrochemical properties were obtained after two and three voltage recovery cycles for baseline

and IL-containing MEAs, respectively. EOL properties were obtained after one voltage recovery cycle for all MEAs.

Table 3-9 Electrochemical properties of Pt/C and Pt/C-IL MEAs after AST.

| | **Baseline Pt/C** | **Pt/C-($[C_2mim]^+[NTf_2]^-$)** | **Pt/C-($[C_4mim]^+[NTf_2]^-$)** | **Pt/C-($[C_4dmim]^+[NTf_2]^-$)** |
|---|---|---|---|---|
| **Cell potential @ 0.8 A $cm^{-2}$** | 0.361 | 0.495 | 0.595 | 0.479 |
| **Peak power density** | 0.349 | 0.474 | 0.642 | 0.460 |
| **Mass Activity at 0.9 V (A $g^{-1}_{Pt}$)** | 21.6 | 15.1 | 29.17 | 7.83 |
| **Specific Activity at 0.9 V (μA $cm^{-2}$)** | 163 | 196 | 165 | 40 |
| **ECSA ($m^2$ $g^{-1}$)** | 1.32 | 7.69 | 17.63 | 19.45 |

All four MEAs showed performance loss over the course of 30,000 AST cycles which took about 50 h. The comparison of polarization curves at BOL and EOL (Figure 3-35a and Figure 3-36) reveals that all the ILs have significantly improved the durability of the cells. All the IL-containing

MEAs showed similar trend at the BOL and EOL, while baseline exhibits more severe loss in medium and high current density area.

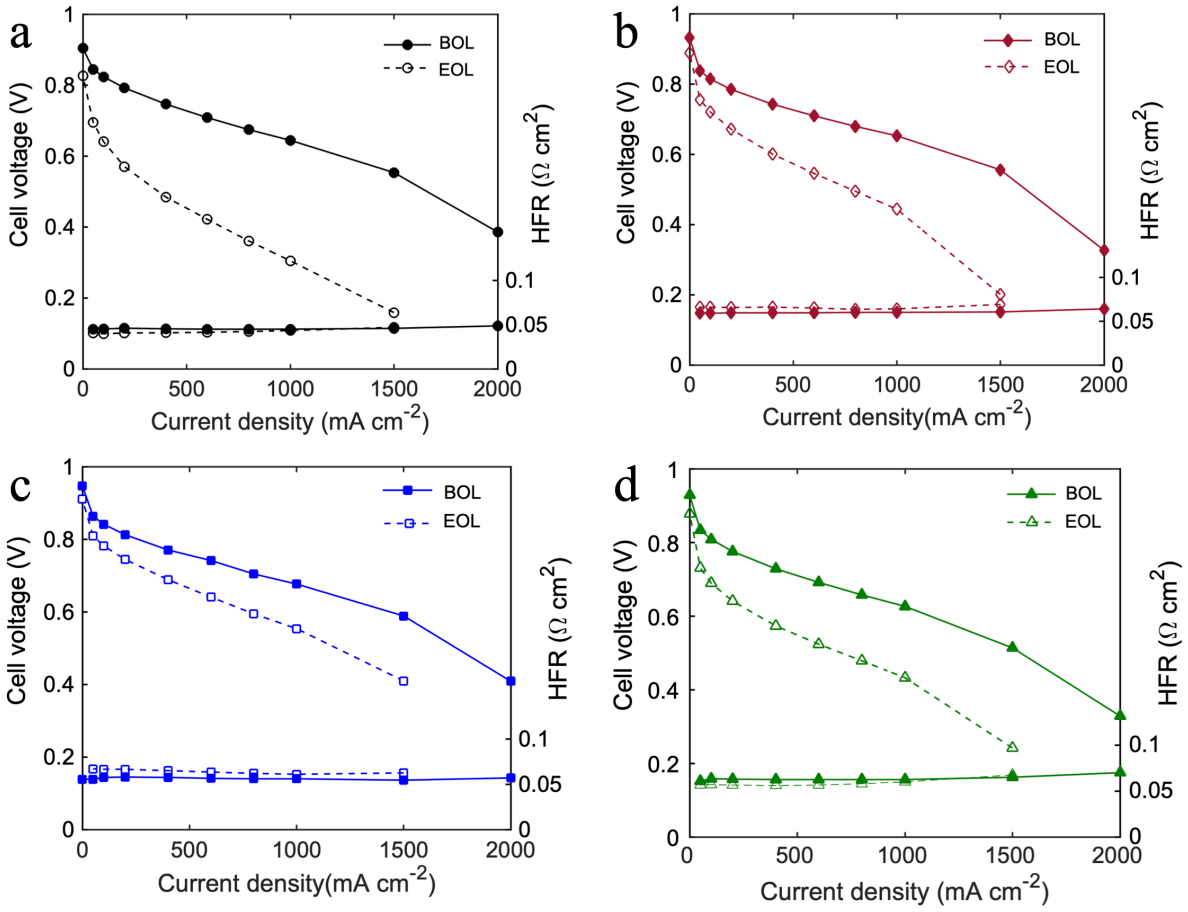


Figure 3-36 a) comparison of $H_2$/air polarization curves at the beginning of life and after 30,000 cycles for a) baseline Pt/C, b) Pt/C-($[C_2mim]^+[NTf_2]^-$), c) Pt/C-($[C_4mim]^+[NTf_2]^-$), d) Pt/C-($[C_4dmim]^+[NTf_2]^-$) MEAs.

As demonstrated in Figure 3-35b, baseline's potential at 0.8 A cm$^{-2}$ dropped from 0.675 to 0.361 V (reduced by 0.314 V); however, the potential decrease for Pt/C-($[C_4mim]^+[NTf_2]^-$) was only 0.11 V. Pt/C-($[C_2mim]^+[NTf_2]^-$) and Pt/C-($[C_4dmim]^+[NTf_2]^-$) both exhibited a potential decrease of 0.18 V. Figure 3-35c represents the ECSA of all the MEAs at BOL and EOL. As can be seen in Figure 3-35c, baseline experienced the most significant ECSA loss from 72.1 to 1.32 m$^2$ g$^{-1}$ and

retained only 2% of the initial ECSA. On the other hand, Pt/C-($[C_4mim]^+[NTf_2]^-$) and Pt/C-($[C_4dmim]^+[NTf_2]^-$) maintained 36%, and 48% of the ECSA, and exhibited surface area of 17.63 and 19.45 $m^2\ g^{-1}$ even after 30,000 cycles, respectively. Pt/C-($[C_2mim]^+[NTf_2]^-$) ECSA decreased from 52.8 to 7.60 $m^2\ g^{-1}$ maintaining 15% of the surface area. We can conclude that bigger IL molecules with longer alkyl chains and more complex chemical structure have more interactions with Pt and the support and are harder to be washed out of the pores; therefore, Pt in contact with ILs will be protected from coarsening. We previously have shown the same effect in HSA Pt/C in which the Pt in contact with ionomer was not affected by dissolution and Ostwald ripening phenomena[22]. Since most of the Pt nanoparticles are dispersed within the pores and are not in contact with ionomer, ILs' role become more dominant in preventing the redeposition of Pt ions. Additionally, ILs can limit the migration of Pt nanoparticles and further collision and coalescence. Figure 3-35d displays the trends in specific activities obtained at 0.9 V during the AST cycling. Both baseline and Pt/C-($[C_2mim]^+[NTf_2]^-$) lost 60% of the specific activity, but Pt/C-($[C_2mim]^+[NTf_2]^-$) still exhibits higher SA of 196 μA $cm^{-2}$ than that of baseline. Pt/C-($[C_4mim]^+[NTf_2]^-$) showed comparable specific activity to baseline although it showed higher roughness factor. These results confirm that catalysts containing ILs are more active toward ORR after 30,000 cycles due to i) higher ECSA retention and ii) sufficient proton conductivity of remaining IL molecules within the pores after the degradation of Nafion. Figure 3-37 represents the changes in peak power density for MEAs. While the peak power efficiency at 30,000 cycle

lifetime for the baseline was only 42%, it increased to 55%, 71%, and 57% for Pt/C-($[C_2mim]^+[NTf_2]^-$), Pt/C-($[C_4mim]^+[NTf_2]^-$), and Pt/C-($[C_4dmim]^+[NTf_2]^-$), respectively.

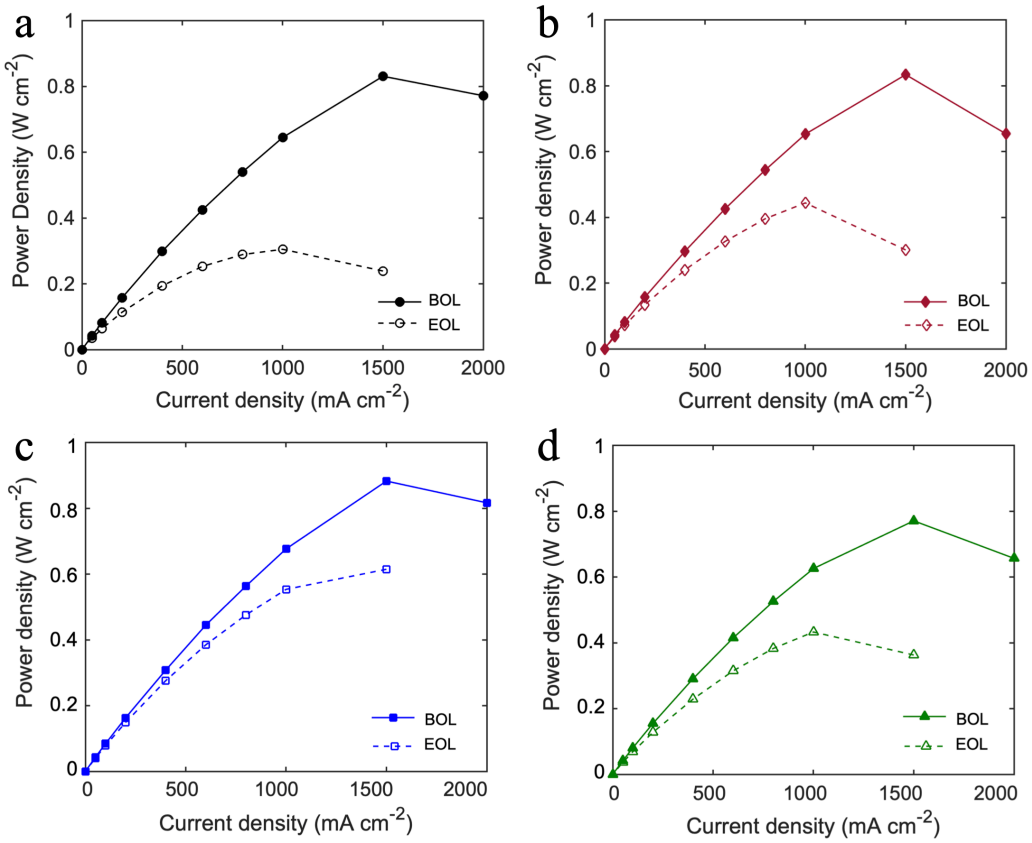


Figure 3-37 a) comparison of $H_2$/air peak power densities at the beginning of life and after 30,000 cycles for a) baseline Pt/C, b) Pt/C-($[C_2mim]^+[NTf_2]^-$), c) Pt/C-($[C_4mim]^+[NTf_2]^-$), d) Pt/C-($[C_4dmim]^+[NTf_2]^-$) MEAs.

## 3.6 Summary

In summary, we identified the design criteria for modification of catalyst layers by incorporation of Imidazolium-derived ILs. These criteria included high $\Delta pK_a$ value for sufficient proton transfer, high oxygen solubility, superior thermal and electrochemical stability, etc. Water uptake and zeta potential measurements brought an insight into the hydrophobicity degree of these ILs that dictates the conformational structure of the Nafion chains as they reorient near Pt surface and within the pores. In addition, the study of physical characterization and EIS fitting demonstrated that proton conductivity is proportional to pore filling degree which are the highest for Pt/C-($[C_2mim]^+[NTf_2]^-$). On the other hand, in-situ electrochemical measurements showed that higher proton conductivity comes at the expense of larger local oxygen transport resistance. Therefore, the best performing IL should be the one that achieved a tradeoff between these two. Moreover, based on the correlation between in-situ fuel cell testing and ex-situ physical characterization, we concluded that a hydrophobic IL with a minimal water uptake induces the least electrostatic repulsion on Nafion chains, while keeping the water layers near Pt surface that promotes the proton conductivity. More importantly, our CO displacement studies showed the predominant role of ILs in protecting Pt surface from $SO_3^-$ poisoning. Our ($[C_4mim]^+[NTf_2]^-$)-modified Pt/C catalyst with optimal hydrophobicity, proton conductivity, and oxygen transport resistance achieved a peak power density of 0.909 W $cm^{-2}$ and enhanced MA and SA by 20% and 75%, respectively. Under the DOE catalyst AST testing protocol, Pt/C-($[C_4mim]^+[NTf_2]^-$) achieved an outstanding durability compared to the baseline as the ILs principally protect Pt from coarsening. We believe that the design approach and concepts presented in this paper can provide a promising way to future design of highly durable and active Pt-based catalysts for PEMFC application.

# Chapter 4

# Investigation of Cathode Catalyst Layer Interfaces Evolution during Accelerated Stress Tests for Polymer Electrolyte Fuel Cells

## 4.1 Introduction

An extensive knowledge about most aspects of fuel cell durability is already present in the literature[129]. A review by Ren et al.[130] summarized most of the achievements done so far in the field and provided the current state-of-the-art research on various degradation aspects of the PEFCs. The degradation of the MEA in the fuel cell stems from the interplay of various mechanisms among which are the loss of catalyst electrochemical surface area, the corrosion of the carbon support, and the chemical and mechanical breakdown of polymeric membrane[131]. To assess the durability of a fuel cell without relying on real-time data, accelerated stress tests have been developed that involve voltage cycling relevant to automotive applications with intermittent performance evaluation standardized by the DOE. Because durability studies in the automotive field revolve particularly around Pt catalyst degradation and carbon-support corrosion, widely-used AST protocols target the degradation of an individual component of the MEA by varying a set of operation parameters[88,132].

Many of the studies focus on catalyst or support degradation[133], but very few focus on ionomer-catalyst interface or ionomer degradation. Ionomer is used in the catalyst layers for proton conduction but its distribution in the cathode catalyst layer dictates the Pt utilization and local oxygen transport at high current densities.[8]. While the influence of ionomer physical configuration on oxygen transport to the Pt catalyst surface has been extensively explored by both experimental[94,16,134] and molecular dynamics simulation[135,136] tools, solid understanding of how ionomer properties change as the cell degrades is currently missing. One work from Hiesgen group focused on the degradation of ionomer using AFM technique showing morphological modification in the ionomer film surrounding Pt agglomerates[137]. It has been shown that the sulfonate moieties ($SO_3^-$) in the side chains of the ionomer can poison Pt catalyst and slow down the oxygen reduction reaction kinetics[113] ; on the other hand, the proximity of sulfonic acid groups to the catalyst surface helps transport protons that are needed for the ORR.

Various approaches have been applied to improve ionomer coverage in the cathode catalyst layer such as introducing chemically modified carbon supports with tailored porosity[138] or nitrogen containing surface[139], designing novel ionomers[140,26], and proposing various electrode fabrication processes[141,142]. In these studies, demonstration of ionomer distribution is either qualitative or is limited to modeling efforts; however, two in-situ experimental methodologies are currently present in the literature that can provide quantitative ionomer coverage data in the PEFC catalyst layers. Iden and Ohma[143] developed a method based on the double layer capacitance collected in different experimental conditions to estimate ionomer and water contributions to the proton accessibility in the cathodes. Garrick et al.[144] also used a combination of CO displacement and CO stripping procedures to evaluate the surface of the platinum that is covered with Nafion's $SO_3^-$ groups. A work by Andersen[145] described the adsorption behavior of ionomer on platinized nano carbons and

amorphous carbon using Langmuir isotherms showing that stronger adsorption of ionomer results in better durability of the catalyst towards AST, but to the best of our knowledge no study explored ionomer coverage evolution during catalyst layer aging using in-situ experimental methods.

In this chpater, we utilized two analytical methods with a combination of testing protocols including catalyst AST under both stoichiometric and sub-stoichiometric reaction conditions, and carbon corrosion ASTs to investigate the evolution of ionomer and $SO_3^-$ groups' coverage in fuel cell cathode electrodes during cell ageing. The extensive characterization provided an insight into the changes in ionomer distribution during degradation and its influence on cell performance, ECSA loss, and ionic conductivity under harsh testing conditions. Ex-situ characterizations such as scanning electron microscopy (SEM) and X-ray photoelectron spectroscopy were also performed at the beginning and end of life to determine the microstructure and composition of the ionomer after degradation. This work brings understanding of ionomer-catalyst and ionomer-carbon interfaces with the hope to develop durable and high-performing fuel cell electrodes for the upcoming generation of heavy-duty vehicles.

# 4.2 Materials and Methods

## 4.2.1 Materials

Two types of MEA with 25cm$^2$ active area were manufactured by IRD Fuel Cells LLC, specifically designed for these experiments. MEAs 1 and 2 (see Table 4-1) featured cathode catalyst layers with standard high surface area carbon support. MEA 1 and 2 underwent catalyst and carbon corrosion ASTs, respectively. All MEAs had ionomer to carbon (I/C) ratio of 0.8. Catalyst AST was also performed under both stochiometric and sub-stoichiometric reactant gas condition, the later one termed as MEA 4. The MEA 3 cathode catalyst was supported on durable, graphitized

carbon support, and it was employed for the support AST studies. Both MEA types have 18µm PFSA membrane and are loaded with Pt catalyst and PFSA-based ionomer. The details about the tested MEAs are reported in Table 4-1.

Table 4-1: Parameters of the MEAs employed in this chapter.

| | Cathode Loading<br>mg $cm^{-2}$ | Anode Loading<br>mg $cm^{-2}$ | Durable Support<br>- | AST Type |
|---|---|---|---|---|
| MEA 1 | 0.6 | 0.2 | no | Catalyst (stoichiometric condition) |
| MEA 2 | 0.6 | 0.2 | no | Support |
| MEA 3 | 0.4 | 0.1 | yes | Support |
| MEA 4 | 0.6 | 0.2 | no | Catalyst (sub-stoichiometric conditions) |

### 4.2.2 Fuel Cell Testing and Characterization

Scribner 850e fuel cell test stand with maximum current load of 50A (Scribner & Associates Inc.) was used for performing AST and measuring performance metrics such as polarization curve and mass activity. ASTs were performed according to the DOE protocols. This work focuses on two AST protocols, namely the Nissan-FCTT Pt dissolution[132] and DOE carbon corrosion cycles.[146] Pt dissolution cycle was performed at 80°C, under fully humidified $H_2$/air at environment pressure[115] and 0.25/0.25 slpm gas flow-rates, with a square-wave potential profile from 0.6 to 0.95 V or OCV, whichever is smaller, with 3s hold at each step[133]. For the starved conditions the flow rates were 0.05/0.05 slpm instead. The total number of cycles was set to 30,000 with interruptions for in-situ electrochemical characterization including polarization curves, cyclic voltammetry, CO displacement/stripping, EIS for calculating double layer capacitance, and catalyst layer ionic

conductivity. Characterizations were performed at the BOL, 1,000$^{th}$, 5,000$^{th}$, 15,000$^{th}$, and 30,000$^{th}$ cycle.

Carbon corrosion AST was also performed at 80°C under fully humidified $H_2/N_2$, with gas flow-rates of 0.25/0.25 slpm. The potential was cycled using a triangular wave between 1 and 1.5 V with a sweep rate of 0.5 $Vs^{-1}$. Interruptions for the characterization were done at 100$^{th}$, 500$^{th}$, 1000$^{th}$, 2500$^{th}$, 5000$^{th}$ cycle under air environment[115]. In-situ electrochemical characterization included polarization curves, CV, CO displacement/stripping, EIS for calculating double layer capacitance, and catalyst layer ionic conductivity.

MEAs were conditioned at 80°C and 100% RH by potential holds at 0.8, 0.6 and 0.3V for 30s each until the values of the current density remains constant for at least 3 consecutive cycles. Polarization curves were performed in $H_2$/air environment with 1.5/1.8 stoichiometric flows at 80°C with 100% RH and 150 kPa absolute pressure. Corresponding cell voltage at each current density (0, 10, 25, 50, 100, 200, 400, 600, 800, 1000, 1200, 1400, 1600, 1800 mA $cm^{-2}$) was averaged over the 180 s current hold. CV was performed to assess the catalyst ECSA by sweeping the potential between 0.095 and 1 V at 20 $mVs^{-1}$. These measurements were performed using VSP-BioLogic 4A potentiostat, feeding the cell with fully humidified (100% RH) $H_2/N_2$ gas flows (0.25 slpm on each side). Cell temperature was set to 80°C with no backpressure applied.

Table 4-2. Summary of the testing protocol for the catalyst AST and characterization.

| | Tcell | H2 | 5%H2 | Air | N2 | CO | RH | DP | Pressure (a) | Flow A | Flow C |
|---|---|---|---|---|---|---|---|---|---|---|---|
| | C | - | - | - | - | - | % | C | kPa (a) | slpm | slpm |
| Conditioning | 80 | X | | X | | | 100% | 80 | 100 | 0.8 | 1.5 |
| Characterization | | | | | | | | | | | |
| Voltage Recovery | 40 | X | | X | | | 150% | 59 | 150 | 0.5 | 0.25 |
| POL Curve | 80 | X | | X | | | 100% | 80 | 150 | ST 1.5 | ST 1.8 |
| CV | 80 | X | | | X | | 100% | 80 | 100 | 0.25 | 0.25 |
| Crossover LSV | 80 | X | | | X | | 100% | 80 | 100 | 0.25 | 0.25 |
| EIS | 80 | X | | | X | | 100% | 80 | 100 | 0.25 | 0.25 |
| CO Displacement | 80 | | X | | | X | 100% | 80 | 100 | 0.5 | 0.8 |
| EIS | 80 | | X | | X | | 100% | 80 | 100 | 0.25 | 0.25 |
| CO Stripping | 80 | | X | | X | | 100% | 80 | 100 | 0.25 | 0.25 |
| CV Cleaning | 80 | X | | | X | | 100% | 41 | 100 | 0.25 | 0.25 |
| EIS | 80 | X | | | X | | 100% | 41 | 100 | 0.25 | 0.25 |
| CO Displacement | 80 | | X | | | X | 100% | 41 | 100 | 0.5 | 0.8 |
| EIS | 80 | | X | | X | | 100% | 41 | 100 | 0.25 | 0.25 |
| CO Stripping | 80 | | X | | X | | 100% | 41 | 100 | 0.25 | 0.25 |
| AST Cycle | | | | | | | | | | | |

BOL, 1000, 5000, 15000, 30000 cycles

### 4.2.2.1 Measurement of $SO_3^-$ Group Coverage Using CO

Evaluation of $SO_3^-$ groups coverage was performed following the method developed by Garrick et al.[144]. CO displacement was preceded under fully humidified 5% $H_2/N_2$ (0.25/0.25 slpm) on the anode and cathode, respectively. 2% CO in $N_2$ was introduced to the equilibrated cathode electrode after 2 min hold at 0.35 V. The potential was kept for 6 more min, while recording the current. The cathode was then purged with $N_2$ for 20 min and subsequently, CO stripping was performed by cycling the potential between 0.095 and 1 V at 20 mV $s^{-1}$. The procedure was repeated in dry conditions at 25% RH.

Current-time plot was corrected by subtracting the baseline current before and after the introduction of CO, and the CO displacement peak was integrated to obtain the displacement charge. Being greater than the potential of zero charge at Pt surface, which is ~0.23 V, the surface charge on the platinum displaced by the CO through oxidation is all attributed to the negatively charged $SO_3^-$ groups. The value of the stripping charge obtained from the CO stripping peak was

used for the calculation of the Pt electrochemical surface area with the assumption of 420 μC $cm^{-2}$ as the unit charge for integrated CO areas:

$$ECSA_{CO} = \frac{Q_{stripping}}{0.42 \times Pt\ loading} \quad [4\text{-}1]$$

where, $Q_{stripping}$ is the CO stripping charge. Finally, the $SO_3^-$ coverage was calculated from the ratio of the twice of the displacement charge, $Q_{displacement}$, to the stripping charge:

$$SO_3^- Coverage = \frac{2Q_{displacement}}{Q_{stripping}} \quad [4\text{-}2]$$

The measurement is carried out three times and only two last measurements are averaged to calculate the displacement charge and the first measurement is discarded.

### 4.2.2.2 Double Layer Capacitance and Catalyst Layer Conductivity

Double layer capacitance ($C_{dl}$) was investigated for all cells following the method described by Iden et al.[143] in which the catalyst layer is simplified as a Randles circuit. The imaginary part of the impedance at low frequency region is used for obtaining the $C_{dl}$. This method identifies four interfaces in the fuel cell catalyst layer that contribute to the total $C_{dl}$, including platinum/ionomer, platinum/water, carbon/ionomer and carbon/water. Potentiostatic EIS was performed at 80°C under fully humidified $H_2/N_2$ environment with gas flow-rates of 0.25/0.25 slpm on the anode/cathode, respectively. The DC potential was kept at 0.2 V with an AC amplitude of 5% of the DC potential, from a frequency of 10,000 Hz to 0.1 Hz. The measurements were repeated three times for each cell in four different conditions: (i) dry condition (25%RH) before CO poisoning, (ii) dry condition (25% RH) after CO poisoning, (iii) wet condition (100% RH) before CO poisoning, (IV) wet condition (100% RH) after CO poisoning; each representing a subset of interfaces that contribute to the total double layer capacitance. Wet conditions express the

contribution of platinum and carbon contacted by both ionomer and water, while the dry conditions represent only the fraction covered by ionomer. Measurements on the CO-poisoned electrodes allow for understanding of sole carbon contribution which can be further subtracted from the total value to calculate the double layer capacitance of single interfaces:

$$C_{tot,100\%RH} = C_{C/i} + C_{C/w} + C_{Pt/i} + C_{Pt/w} \quad [4\text{-}3]$$

$$C_{tot,25\%RH} = C_{C/i} + C_{Pt/i} \quad [4\text{-}4]$$

$$C_{100\%RH,poisoned} = C_{C/i} + C_{C/w} \quad [4\text{-}5]$$

$$C_{25\%RH,poisoned} = C_{C/i} \quad [4\text{-}6]$$

where, subscripts C/i, C/w, Pt/i and Pt/w indicate interfaces at carbon/ionomer, carbon/water, Pt/ionomer and Pt/water, respectively. Once all the interfaces are known, the ionomer coverage on platinum and carbon can be calculated:

$$\theta_{i,Pt} = \frac{C_{Pt/i}}{C_{Pt/i} + C_{Pt/w}} \quad [4\text{-}7]$$

$$\theta_{i,C} = \frac{C_{C/i}}{C_{C/i} + C_{C/w}} \quad [4\text{-}8]$$

For the catalyst layer ionic conductivity calculations, EIS data was used. The impedance spectra from EIS data showed a 45° line in the high to medium frequency region where real and imaginary parts are equal, followed by a straight vertical line, representing a capacitive region. A physical impedance model, transmission line model (TLM), was used to fit the EIS data at high frequencies to measure the proton conductivity of the cathode catalyst layer [147,148].

### 4.2.3 Ex-situ characterization

SEM cross-sectional images were taken from the pristine and aged cells. Samples were prepared by peeling off GDLs from the MEAs, and subsequently embedding small pieces into epoxy resin (Araldite 502 epoxy resin, SPI Chem.). Samples were cut with slow speed SiC circular saw (South Bay Technologies inc.) and the sections were polished with P800, P1500, P3000 grit sandpaper, and later with 30 μm and 0.5 μm alumina paste. Cross sections were contacted to SEM stubs using silver conductive in, and SEM images were collected using Hitachi Ultra-High-Resolution SEM Regulus 8230.

The XPS data were measured by Kratos AXIS Supra X-ray photoelectron spectrometer, with a monochromatic Al Kα operating at 225 W for survey spectra and 300 W for high-resolution spectra. The survey spectra were acquired using 160 eV pass energy, 1 eV step size, 100 ms dwell time, while the high-resolution spectra were acquired using 20 eV pass energy, 0.1 eV step size, and 100 ms dwell time. For each spectrum, the data were averaged by three random sample points and each sample point was averaged by specific cycles of scanning. All spectra were analyzed using CasaXPS software and fitted with 70 % Gaussian / 30 % Lorentzian line shape.

## 4.3 Results

### 4.3.1 Catalyst AST

Catalyst AST was performed on MEA 1, where the cell was cycled for 30,000 times. Pt underwent oxidation, dissolution and ripening. ECSA and ionomer coverage were recorded at defined

intermediate steps. The Nissan-FCTT Pt dissolution cycle is designed to trigger the dissolution and re-deposition of the catalyst. Figure a shows the polarization performance and high frequency resistance (HFR) of the cell at the BOL during the catalyst AST protocol. Most of the polarization loss occurred during the first 5,000 cycles in the kinetic and Ohmic regions. This is consistent with the changes in the ECSA, shown in Figure c, where a sharp decrease is observed for the first 5,000 cycles and then more gradual ECSA loss is observed with both CO-stripping and $H_{UPD}$ methods under wet conditions. Therefore, the polarization loss observed in kinetic and Ohmic regions is largely due to ECSA loss. Overall, after 30,000 cycles, MEA 1 lost 50 % of its ECSA, as measured in wet conditions. However, in dry conditions the ECSA did not change. Under dry conditions, one detects Pt in contact with ionomer but not with water. Pt that is in micro- and meso-pores is mainly in contact with water and under dry conditions there is no condensed water to conduct ions. The voltage at higher current densities than 1.5 A $cm^{-2}$ increase at 5,000 cycles and then decrease after 15,000 and 30,000 cycles. This is possibly due to improved wettability of the catalyst layer as shown by slightly reduced HFR at high current density for 5,000 and after, due to better accessibility to the catalyst or better oxygen transport. From the shape of the $H_{UPD}$ region displayed in Figure b, it can be shown that the first $H_{UPD}$ peak decreased more with the number of cycles. This is generally associated with the changes in the 110 and 111 facets, where the surface of the Pt is rearranging by the loss of high energy facets and the increasing amount of lower energy facets[149] caused by the dissolution/redeposition of Pt during AST protocol.

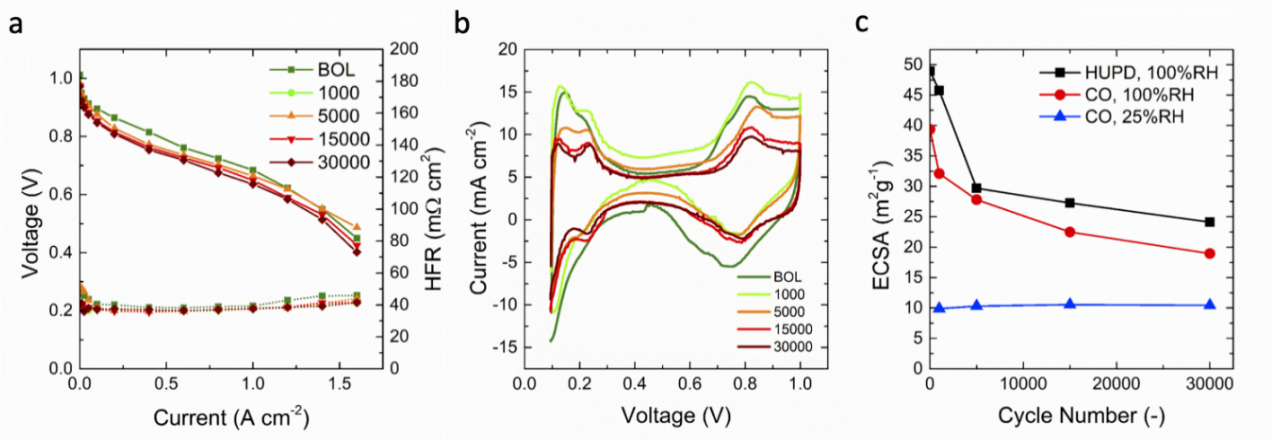


Figure 4-1 Electrochemical properties of MEA 1 collected at different stages of the catalyst AST: a) polarization curves at 80°C, 100 RH, 1.5/1.8 stoichiometric flows with 150 kPa absolute back-pressure, b) cyclic voltammograms, c) evolution of the ECSA determined by both $H_{UPD}$ region of the $H_2/N_2$ CV and CO-stripping charge at indicated RH.

Figure 4-1c exhibits the difference in ECSA obtained from dry and wet measurements which is most likely due to the difference in the amount of Pt within the micro- and meso-pores and that on the surface of the high surface area carbon. As already mentioned, for 25 % RH most of the detected ECSA is attributed to Pt on the surface of the carbon and not within the carbon support pores. The ionomer polymer chains are in the range of tens of nanometer in diameter and cannot penetrate the meso and micropores of the carbon support due to the size exclusion[94] and only water is expected to conduct ions in the micro- and meso-pores. For 25 % RH, we expect no liquid water condensation in the pores and hence Pt in the pores will not be detected by the ECSA measurements. By comparing the ECSA value at the BOL in dry and wet conditions, which is about 10 and 40 $m^2\ g^{-1}$, respectively, one can conclude that most of the nanoparticles (about 75% of them) are dispersed inside the micropores of the carbon support and are not accessed by the ionomer. Furthermore, while the total surface area under 100 % RH decreases with cycling, the

area contacted by the ionomer (determined by dry CO measurements) remains constant. Several conclusions can be implied from this data: (i) Pt in contact with ionomer does not degrade or/and (ii) Pt dissolves from micro- and meso-pores and redeposits in the areas with ionomer coverage but Pt still dissolves from under ionomer. It is possible that positively charged Pt ions are expelled from the micro- and meso-pores with positive pore surface charge at these high potentials and then redeposited in the locations where sulfonic acid groups partially balance surface positive charge.

Figure 4-2a shows the variation of the double layer capacitance for MEA 1 under wet and dry conditions. Double layer capacitance for wet condition includes all interface, such as Pt/i, Pt/w, C/i and C/w. The double layer capacity for 100 % RH was 300 mF $cm^{-2}$ at the BOL and it decreased to 175 mF $cm^{-2}$ after 30,000 AST cycles. ECSA loss amounted to 50 % from the BOL to 30,000 cycles, and double layer capacitance loss was about 40 %, indicating that C/i and C/w double layer capacitance cannot be neglected. The double layer capacitance for dry conditions was75 mF $cm^{-2}$ and it was reduced to 30 mF $cm^{-2}$ after 30,000 cycles. The ratio of double layer capacitance in wet and dry conditions is similar to that of wet and dry ECSA which is about 4. The double layer capacitance data is in alignment with the ECSA data confirming that about 75 % of the Pt particles are in contact with water and only 25 % of them are in contact with the ionomer.

Figure b shows the evolution of the ionomer coverage on Pt and carbon obtained from the difference between the double layer capacitances at various RH, as described in Section 4.2.2.2. About 50 % of accessible carbon area is covered by ionomer, indicating that the remaining 50 % is covered by water. This agrees with the carbon support having high surface area. The fraction of C/i interface remained constant from the BOL to EOL, as catalyst AST does not have a strong effect on carbon corrosion. The Pt/i interface fraction decreases with the AST cycling. At the BOL, the Pt/i interface is about 20 %, whereas the remaining 80 % is Pt/w interface. The ionomer

coverage here agrees well with the ECSA and double layer capacitances data. At 15,000 AST cycles, the ionomer coverage increased to 38 % but decreased to below 10 % at 30,000 cycles because the ionomer coverage is a relative value and the sum of Pt/i and Pt/w must be equal to 100 %. At 15,000 cycles, the relative fraction of Pt/i increased as Pt has been lost from the micro- and meso-pores (indicated by wet ECSA), where it was in contact with water. The loss of Pt/i at 30,000 cycles can potentially be due to ionomer degradation, which will be explored when the XPS data is discussed.

The evolution of $SO_3^-$ coverage on Pt is reported in Figure 4-2c. This coverage is different from the ionomer coverage, as it shows only the fraction of the Pt surface that the side chain of the PFSA-based polymer is adsorbed on, as described by Equation 4-2. Both in the wet and dry cases, the $SO_3^-$ coverage on Pt is decreasing with AST. For 100 % RH at the BOL, the $SO_3^-$ coverage on Pt is 0.32, which is similar to what has been reported in literature [144,150]. At 15,000 cycles, the $SO_3^-$ coverage decreased to 0.25 in wet conditions. As can be seen, some $SO_3^-$ coverage data points are not available due to the complexity of the measurements and the fact that reproducibility was not achieved for these points.

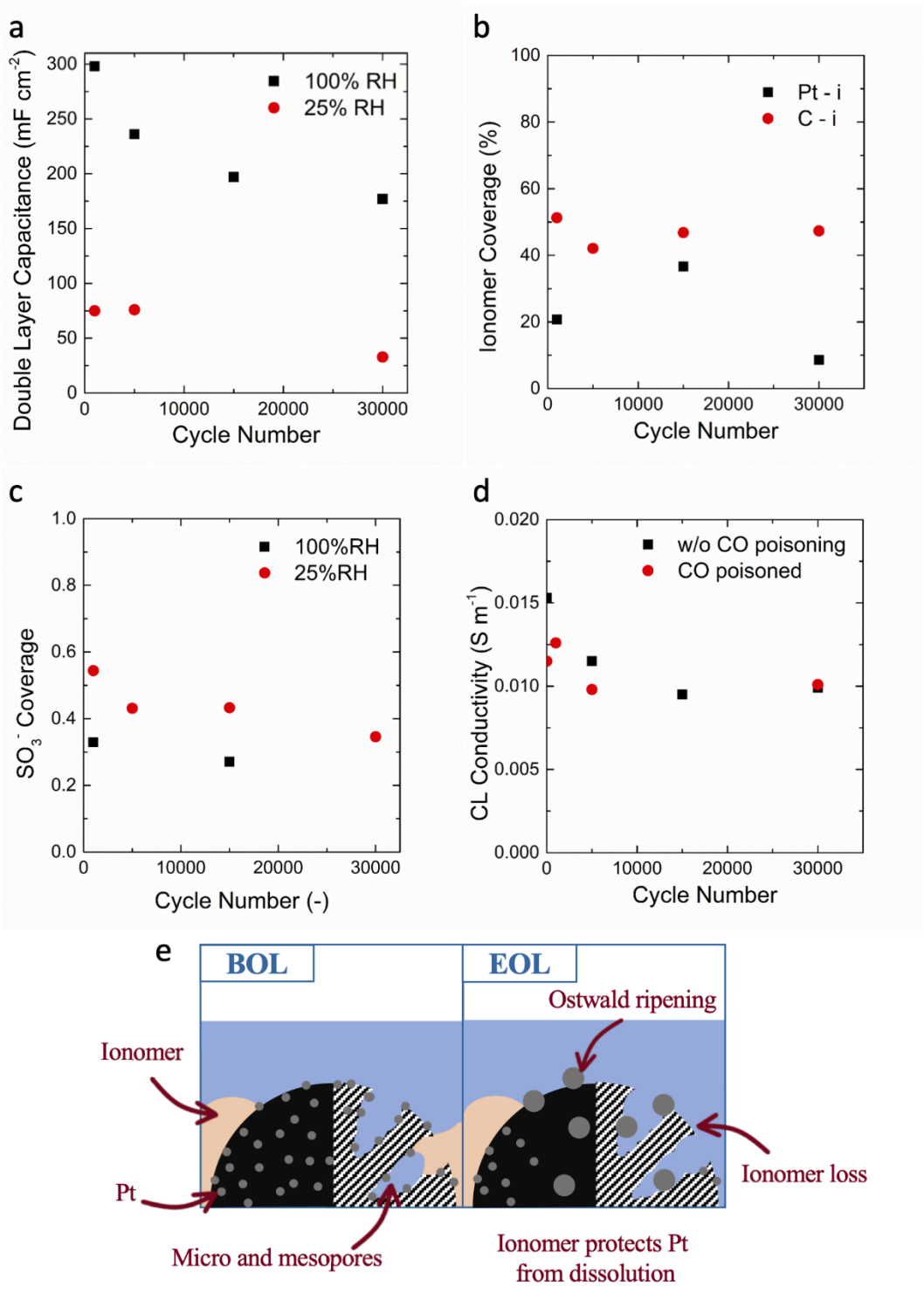


Figure 4-2 a) Double layer capacitance for MEA 1 for humidified and dry conditions, b) ionomer coverage for MEA 1 on platinum and carbon support, c) $SO3^-$ coverage on Pt surface for the specified RH values, d) catalyst layer conductivity at 25% RH from the EIS for MEA 1 with and

without CO. e) A schematic of the proposed degradation phenomena occurring for MEA 1 subjected to catalyst AST.

Similar decreasing trend in $SO_3^-$ coverage on Pt was observed for 25 % RH, but the ionomer coverage was much higher. This is because of low CO-stripping charge on Pt at 25 %. As can be seen from Equation 4-2, the $SO_3^-$ coverage is proportional to the ratio of CO-displacement and CO-stripping. For both 100 % and 25 % RH, the CO-displacement charge is similar (Figure 4-3), but CO-stripping charge is much higher for 100 % RH as Pt that is covered by water in the micro- and meso-pores is detected in wet conditions. We also observe the CO-stripping charge (proportional to ECSA values from Figure 4-1) does not change with AST cycling at dry conditions. Figure 4-3 and Table 4-3 show the change in displacement and stripping charges for MEA 1.

However, the $SO_3^-$ coverage on Pt at 25 % RH decreases from 0.55 to 0.35. This decrease is due to reduction in CO-displacement charge (absolute value). This decrease in the coverage can be attributed to a chemical degradation of the ionomer itself. It is reported in the literature that at high potentials, OH radicals react with Nafion side chains and contribute to degradation of the membrane[151]; therefore, ionomer is also affected.

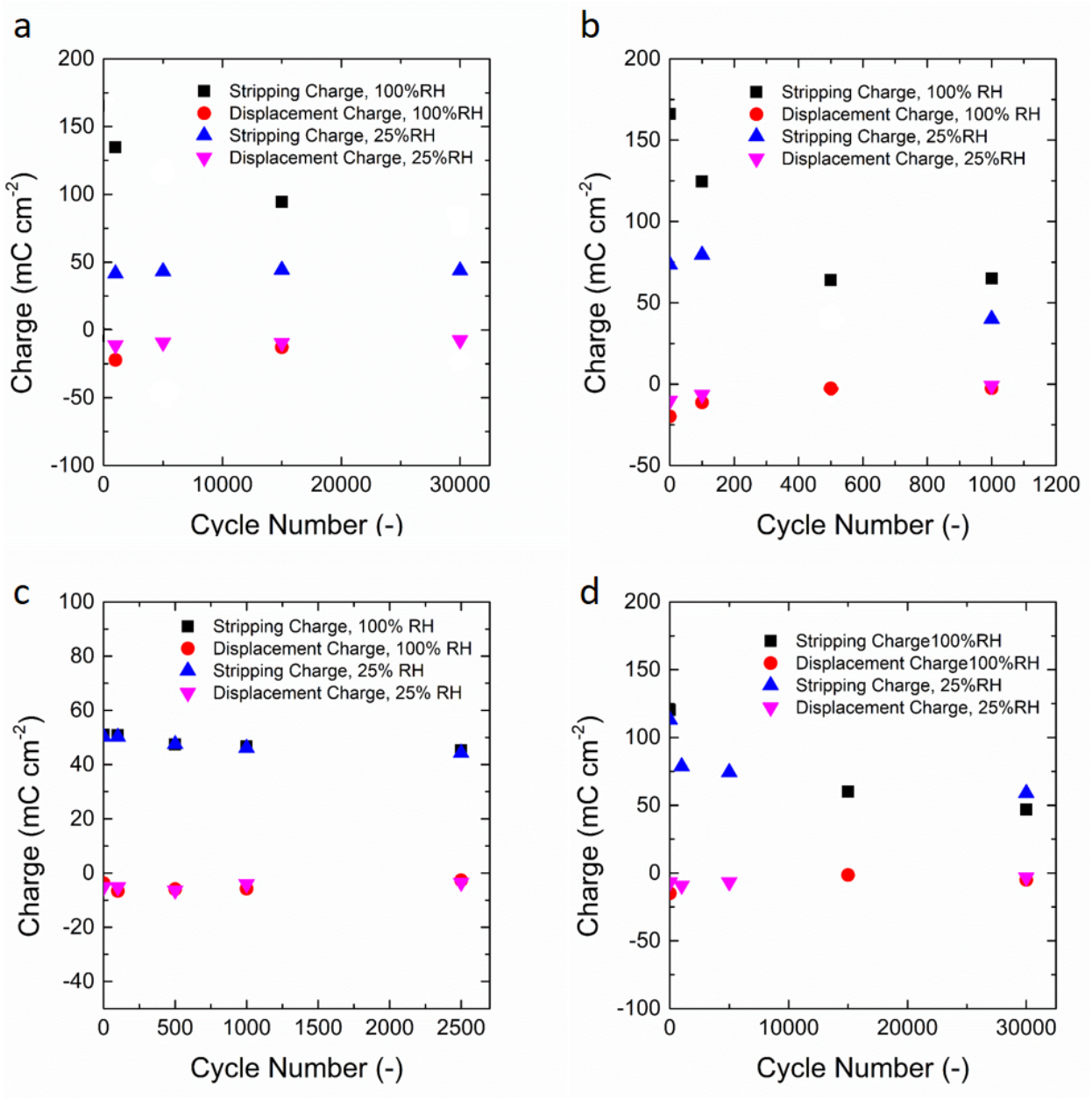


Figure 4-3 CO-displacement and stripping charges for the indicated relative humidity of a) MEA 1, b) MEA 2, c) MEA 3, d) MEA 4.

Table 4-3 Values of the stripping and displacement charges from the plots in Figure 4-3

| MEA 1, Charge | | | | |
|---|---|---|---|---|
| Number of cycles | Stripping 25%RH | Displacement 25%RH | Stripping 100%RH | Displacement 100%RH |
| - | mC $cm^{-2}$ | mC $cm^{-2}$ | mC $cm^{-2}$ | mC $cm^{-2}$ |
| 0 | - | - | - | - |
| 1000 | 41.5 | -11.29 | 134.8 | -22.17 |
| 5000 | 43.3 | -9.33 | - | - |
| 15000 | 44.3 | -9.59 | 94.5 | -12.8 |
| 30000 | 43.8 | -7.57 | 79.6 | - |

| MEA 2, Charge | | | | |
|---|---|---|---|---|
| Number of cycles | Stripping 25%RH | Displacement 25%RH | Stripping 100%RH | Displacement 100%RH |
| - | mC $cm^{-2}$ | mC $cm^{-2}$ | mC $cm^{-2}$ | mC $cm^{-2}$ |
| 0 | 73.45 | -10.12 | 166 | -19.81 |
| 100 | 79.45 | -6.5 | 124.5 | -11.23 |
| 500 | - | - | 64 | -2.61 |
| 1000 | 40.1 | -0.956 | 65 | -2.52 |

| MEA 3, Charge | | | | |
|---|---|---|---|---|
| Number of cycles | Stripping 25%RH | Displacement 25%RH | Stripping 100%RH | Displacement 100%RH |
| - | mC $cm^{-2}$ | mC $cm^{-2}$ | mC $cm^{-2}$ | mC $cm^{-2}$ |
| 0 | 50.2 | -5.13 | 50.95 | -3.71 |
| 100 | 50.2 | -5.2 | 50.9 | -6.59 |
| 500 | 47.5 | -6.4 | 47.4 | -5.9 |
| 1000 | 46.1 | -4.09 | 46.7 | -5.75 |
| 2500 | 44.25 | -3.53 | 45.3 | -2.65 |
| | | | | |
| MEA 4, Charge | | | | |
| Number of cycles | Stripping 25%RH | Displacement 25%RH | Stripping 100%RH | Displacement 100%RH |
| - | mC $cm^{-2}$ | mC $cm^{-2}$ | mC $cm^{-2}$ | mC $cm^{-2}$ |
| 0 | 113.1 | -6.80 | 120.2 | -15 |
| 1000 | 78.7 | -9.1 | - | - |
| 5000 | 74.4 | -6.76 | - | - |
| 15000 | - | - | 60.05 | -1.43 |
| 30000 | 59 | -3.166 | 46.85 | -5.10 |

These observations are supported by XPS analysis in Figure 4-4a by comparing the changes in the intensity of C-F bond peak with the pristine case (in Figure 4-4c) where we see a smaller intensity. This peak is related to the bond between C and only one fluorine, which corresponds to the position in the PTFE backbone where the side chain is present. From the elemental survey in Figure 4-4d, we also register a smaller atomic concentration of sulfur, which indicates the loss of side chains and $SO_3^-$ groups.

Figure d shows the evolution of the ionic conductivity in the catalyst layer obtained from the EIS spectra fitting for dry conditions. This ionic conductivity captures only ionomer and not water clusters that can connect the disconnected ionomer segments. The ionic conductivity of the catalyst layer does not change significantly during AST cycling. EIS data was available for catalyst layer as is, and also after CO-poisoning. Both show similar trends with the loss of ionic conductivity within first 5,000 cycles and then leveling off conductivity values from 5,000 to 30,000 cycles.

In summary, behavior of ionomer in the cathode catalyst layer during a catalyst AST can be summarized by Figure 4-2e. Pt dissolution reaction is triggered by the voltage cycling but the dissolution rates are different for Pt in contact with ionomer vs. Pt in contact with water (in micro- and meso-pores). Higher dissolution rates are observed for Pt in contact with water, perhaps due to higher Pt ions transport in confined water environment in micro- and meso-pores that can be affected by electric double layers and surface charge (positive for high applied potentials). In parallel, due to the high potential and production of OH radicals, some ionomer loss is observed because of the chemical attack, resulting in loss of $SO_3^-$ group coverage on the platinum surface.

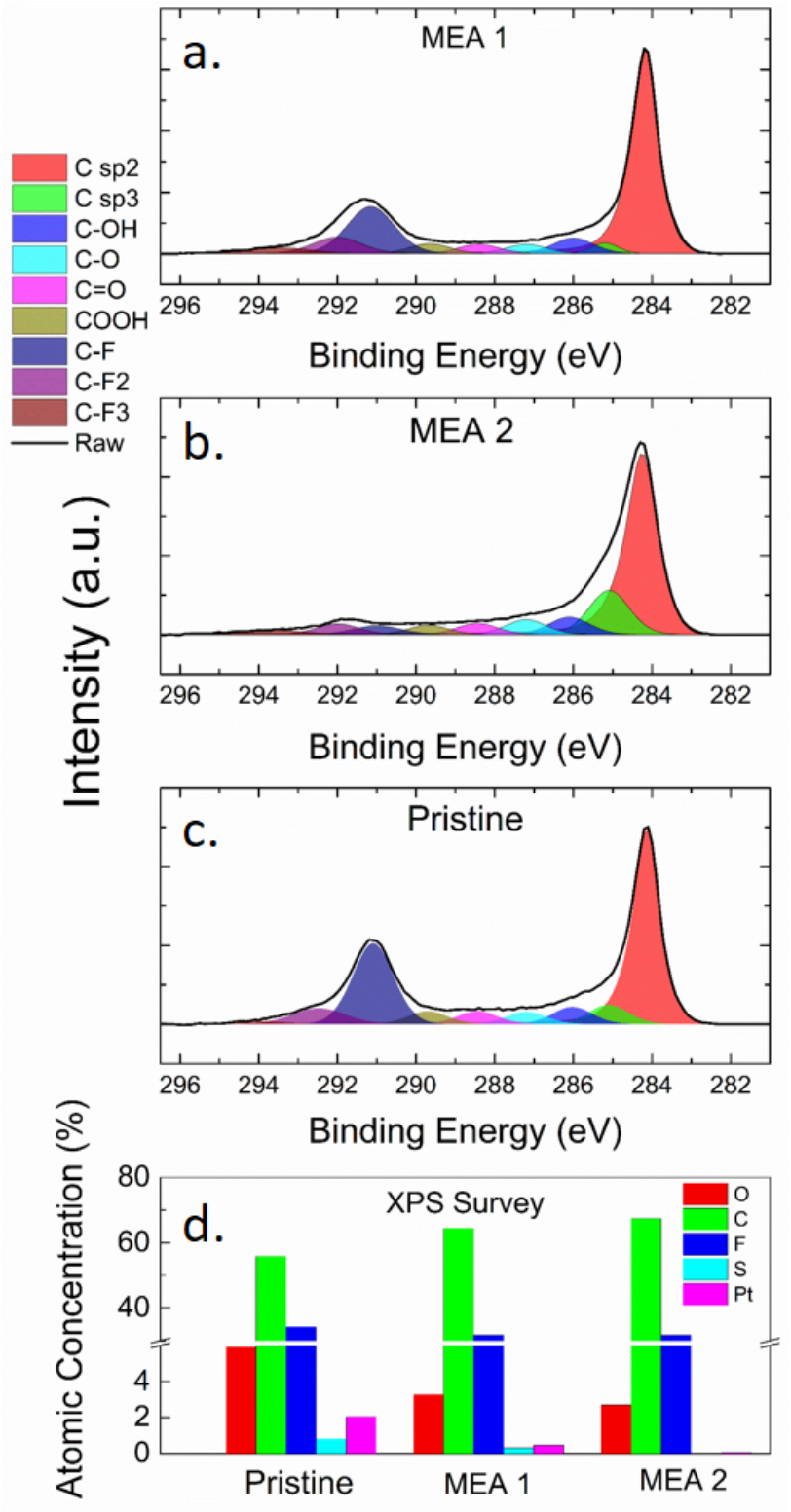


Figure 4-4 a) XPS of carbon for MEA 1, b) MEA 2 and c) pristine MEA. d) Elemental survey for the three MEAs.

TEM using Jeol Grand Arm has been performed on the pristine and aged MEA 1. The results are shown in Figure 4-5, where particle size distributions were reported, as an average over multiple images collected over various locations. From the particle size analysis, the mean particle size increased from 3 nm for pristine MEA to around 6 nm for aged MEA. For aged MEA 1, one observes a broad particle size distribution range, ranging from 2 nm to 14 nm. This might be due to protective effect of the ionomer over the small platinum particles. From the TEM image it is not possible to discern which particles are covered or not covered by ionomer. The inhomogeneity in particle size partially supports the conclusion on different modes of degradation for Pt covered and not covered by ionomer.

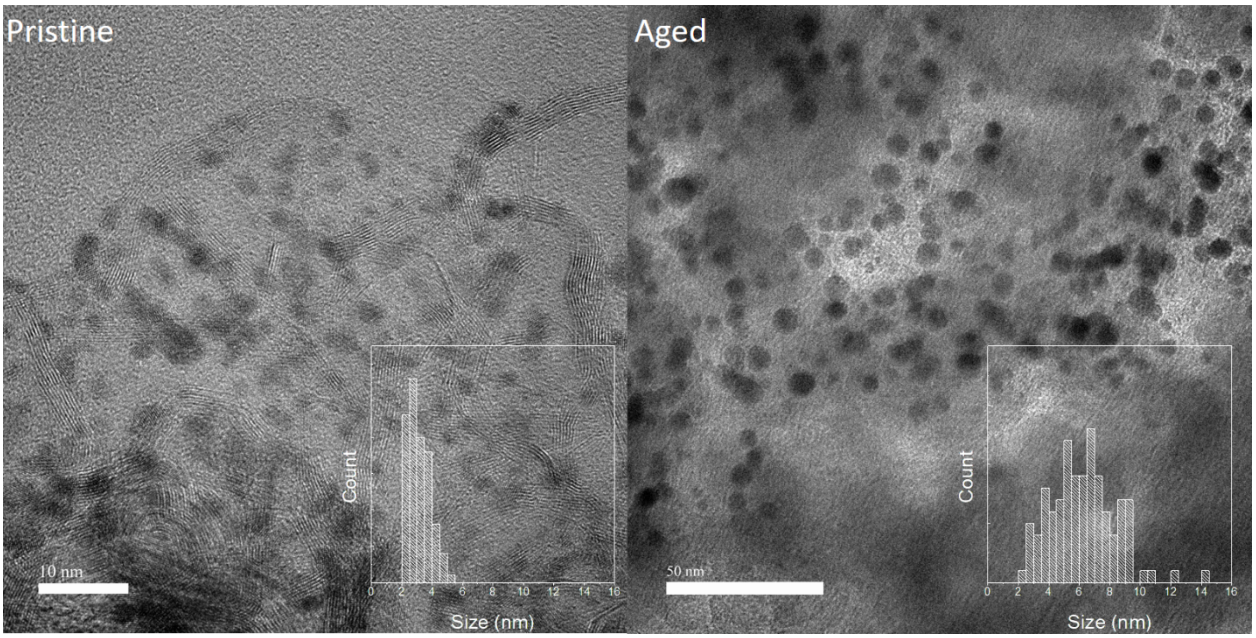


Figure 4-5 TEM images of the MEA 1 catalyst particles and support before and after the platinum dissolution AST. Particle size distributions are reported within the images.

Figure 4-6 displays the polarization curves, CVs, Tafel plots and ECSA loss for MEA 4, which was subjected to starvation conditions in terms of gas flow. MEA 4 was identical to MEA 1 but used 5 times lower gas flow-rates during catalyst AST. The polarization loss and ECSA loss was observed to be more dramatic for MEA 4 compared to MEA 1. Voltage loss in some polarization regions between BOL and EOL was higher than 100 mV. At 0.2 A $cm^{-2}$ cell voltage difference between the BOL and EOL was close to 100 mV, compared to only 70 mV for MEA 1. The ECSA loss was 60–63% at wet conditions and for dry conditions it was about 50%. Similar to MEA 1 majority of ECSA loss happened within 5000 AST cycles. Unlike MEA 1, this reactant starved MEA has seen increase in HFR at 15000 and 30,000 cycles. Figure 4-7 shows the changes in double layer capacitances, ionomer coverage, sulfonic acid group coverages and catalyst layer conductivities for MEA 4. For most of these similar trends are observed with the MEA 1 but for $SO3^-$ coverage that did not show trend. Figure 4-8 shows the decrease in C-F bond intensity from BOL to EOL, indicating that MEA 4 similarly to MEA 1 had ionomer degradation. High gas flow-rates are important during the AST as they ensure the stable potential of the anode and uniform along-the-channel conditions for both anode and cathode. Otherwise, the AST will be conducted in inhomogeneous conditions for gas flow along the channel and heterogeneous degradation of catalyst layers will occur.

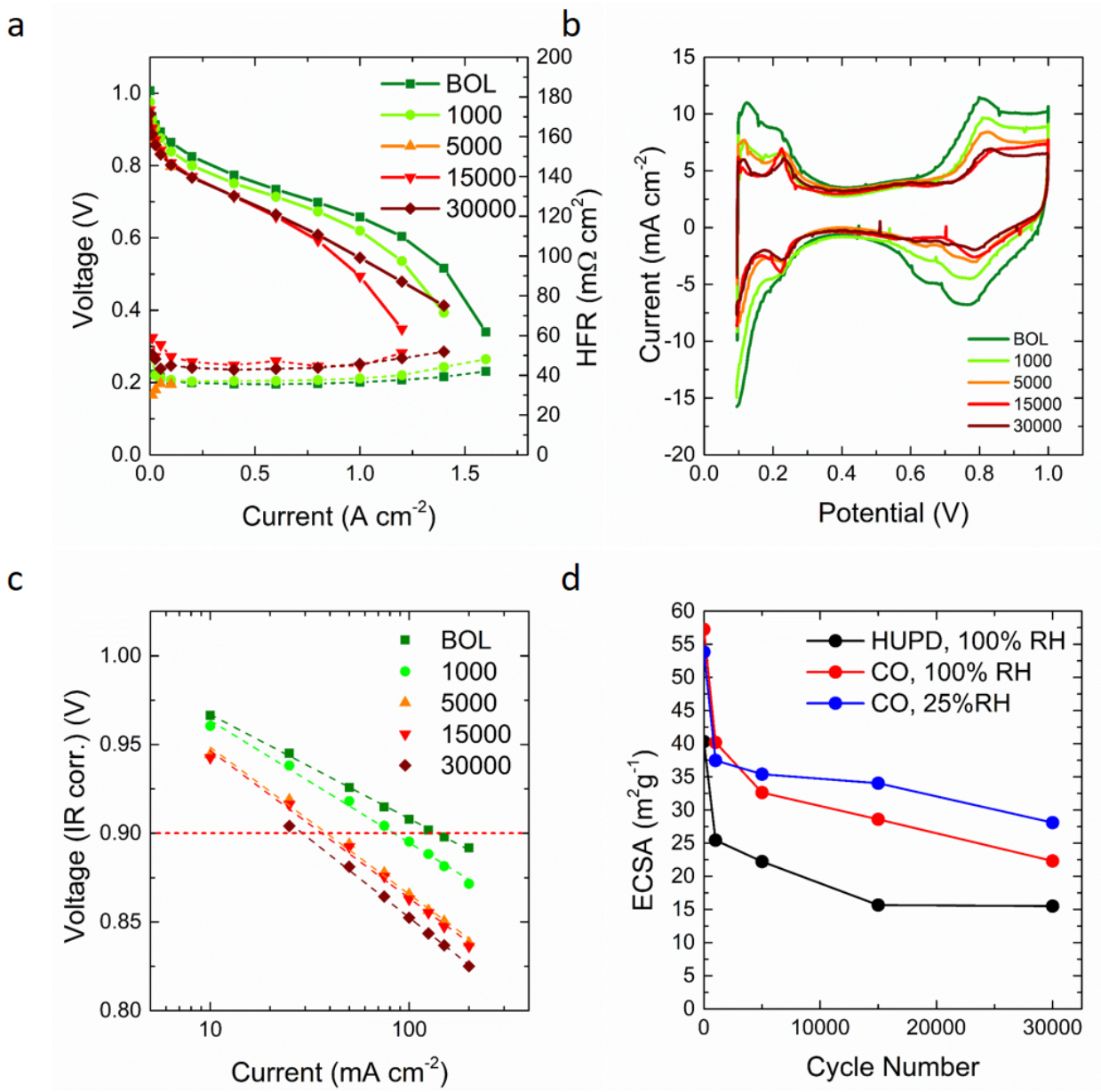


Figure 4-6 Electrochemical properties of MEA 4 collected at different stages of catalyst AST: a) polarization curves, b) cyclic voltammograms, c) oxygen polarization curves. d) ECSA evolution for MEA 4 collected from $H_{UPD}$ and CO-stripping for the indicated relative humidity values.

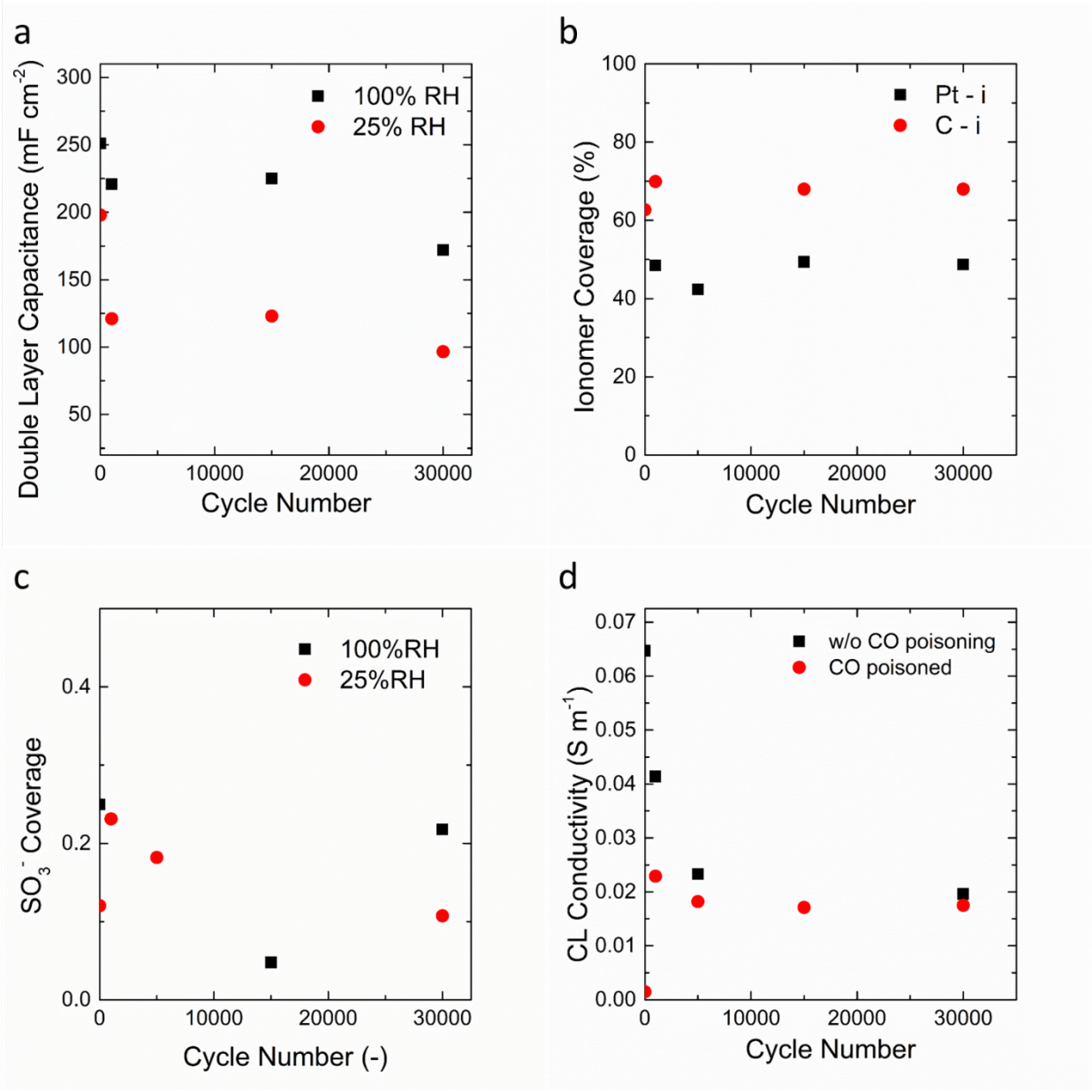


Figure 4-7 a) Double layer capacitance for MEA 4 for humidified and dry conditions, b) ionomer coverage for MEA 2 on platinum and carbon support, c) SO3- coverage on Pt surface for the specified RH values, d) catalyst layer conductivity at 25% RH from EIS.

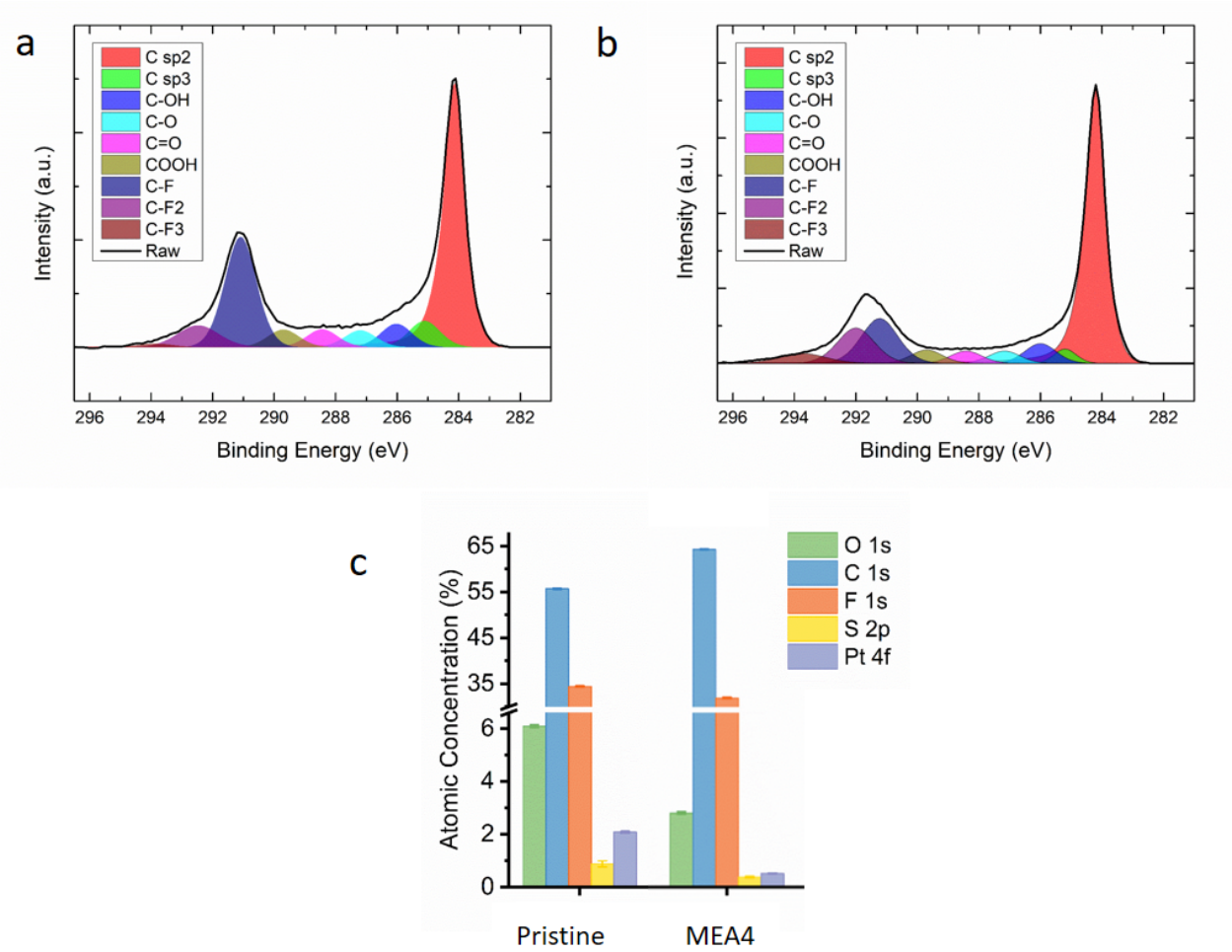


Figure 4-8 a) XPS of carbon for pristine MEA, b) MEA 4 after Pt AST in starved conditions and c) element survey for the two MEAs.

## 4.3.2 Carbon Corrosion AST

During carbon corrosion AST, the cell voltage is swept between 1 and 1.5 V. In this condition, Pt is almost fully oxidized on the surface and does not participate in the degradation phenomena; thus, we can expect that most of the ECSA loss be attributed to the corrosion of the support that disconnects the catalyst from the electron and proton pathways. Figure -9a shows the polarization performance of the cell during the first 1,000 carbon corrosion AST cycles. Dramatic loss of the

polarization is seen between 100 and 500 cycles; however, no increase in the HFR was observed. The HFR increased significantly between 500 and 1000 cycles because of the lack of electron and proton pathways after carbon corrosion. This does not seem to induce a major limitation to the cell performance because most of the losses are observed prior to the HFR increase. ECSA, as can be seen from the CV plots in Figure -9b and 4-9d**,** has a steady decrease up to 500 cycles, where the cell loses half of its initial active Pt surface, and then stabilizes for the remaining 500 cycles. MEA 1 and 2 show similar ECSA in wet condition, while the dry ECSA is slightly higher for MEA 2 compared to MEA 1. The ECSA loss is also observed at 25 % RH, indicating that Pt/i interface is also lost. The CVs are similar in MEA 1 and MEA 2, as predominantly the first $H_{UPD}$ peak (Pt(110)) is lost during AST. However, a distinct feature on the CV is observed for MEA 2 at 500 and 1000 cycles, at around 0.6 V that is attributed typically to carbon oxidation.

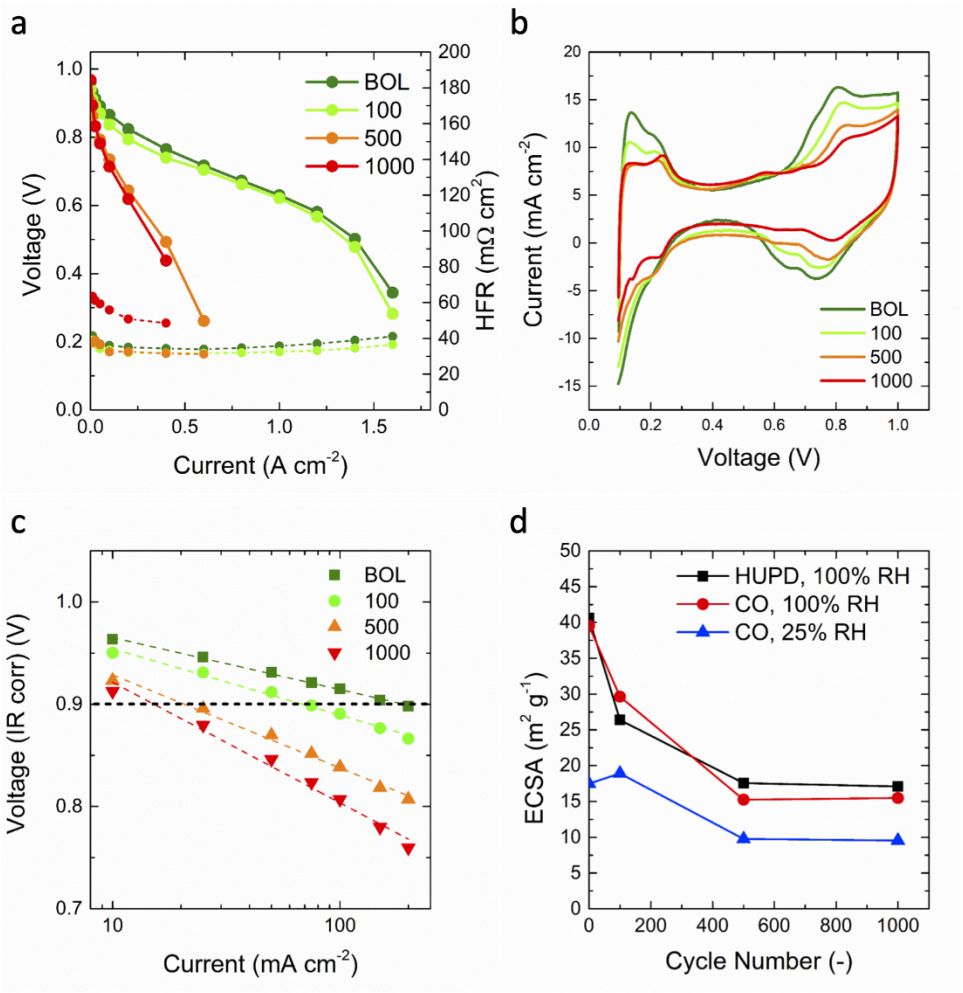


Figure 4-9 Electrochemical properties of MEA 2 collected at different stages of carbon corrosion AST: a) polarization curves, b) cyclic voltammograms. c) oxygen polarization curves. d) ECSA evolution for MEA 2 collected from HUPD and CO stripping for the indicated RH values.

Similar dramatic loss in polarization is observed in $H_2/O_2$ as shown by Figure -9c, where the IR-corrected I-V curves are reported on the x-log scale. The slope of the curves is the Tafel slope that represents the mechanism of ORR (number of electrons that participate in reaction), assuming a single rate-determining step and that all the losses are kinetic in nature. The Tafel slopes are tabulated in Table 4-4, where Tafel slopes change from 50.8 mV $dec^{-1}$ at the BOL to 133 mV dec-

$^{1}$ at 1000 cycles. Since, the catalyst composition did not change, there is no reason for the reaction mechanism to change. The only explanation for the increased Tafel slope is that at higher cycles (500 and 1000), transport and ohmic limitations become significant. The mass and specific activities (per geometric area) also show dramatic decrease between 100 and 500 cycles. A sharp decrease in the catalytic activity seems to be the main factor that determines the degradation of the cell. This should be attributed to the Pt ECSA loss (about 50 %) due to the failure of the support during corrosion, disconnecting and mechanically removing Pt particles. From the ECSA plot, an ECSA loss of 10 $m^2$ $g^{-1}$ is observed from the BOL to 1000 cycles, but the polarization behavior does not change significantly with a small decrease in kinetic region, as expected. However, when ECSA was further reduced to 15-17.5 $m^2$ $g^{-1}$ in wet conditions, this is where the catastrophic polarization loss was observed. The large kinetic loss is apparent in both Figure 4-9a and Figure 4-9c. When using Tafel model for ORR kinetics, one can derive equation where the loss in overpotential per decade of catalyst loading corresponds to the value of Tafel slope.[152] The ECSA ratio of the BOL to 500 cycles is about 3; therefore, the effective loss of loading is most likely similar to this ratio. From Table 4-4, about 22 mV (Tafel slope of 65 mV $dec^{-1}$ divided by 3) is expected to be lost as overpotential due to the reduction in the ECSA between the BOL and 500 cycles and the actual loss at 10 mA $cm^{-2}$ (from Figure 4-9c) is close to this value and is 38 mV. The loss of ECSA explains the increase in overpotential in the kinetic regime, but it does not explain the increase in the Tafel slope (Table 4-4 and Figure 4-9c) and progressively higher overpotential losses in the Ohmic region that cannot be elucidated by the HFR as the HFR value is very similar in BOL and after 500 cycles.

Table 4-4 Slope and $i_{0.9V}$ from IR corrected I-V curves in $H_2/O_2$ for MEA 2.

| Cycles | Tafel slope, absolute value (mV $dec^{-1}$) | $i_{0.9V}$ (mA $cm^{-2}_{geo}$) | Mass Activity (mA $mg^{-1}$) | Specific Activity (mA $cm^{-2}_{Pt}$) |
|---|---|---|---|---|
| 0 | 50.8 | 192.1 | 320.1 | 0.486 |
| 100 | 65.0 | 67.73 | 112.9 | 0.229 |
| 500 | 91.1 | 20.76 | 34.6 | 0.137 |
| 1000 | 133 | 15.96 | 26.6 | 0.104 |

Figure 4-10a shows the double layer capacitance trend as a function of AST cycles and the decrease of the double layer capacitance for wet conditions is similar to that of MEA 1. At the BOL, the double layer capacitance was 300 mF $cm^{-2}$ (also 300 mF $cm^{-2}$ for MEA 1) and it decreased to about 175 mF $cm^{-2}$ at 1000 AST cycles. At 25 % RH, MEA 2 showed higher double layer capacitance of 130 mF $cm^{-2}$ at the BOL while MEA 1 exhibited a double layer capacitance of 75 mF $cm^{-2}$. This indicates that MEA 2 has more Pt on the surface compared to the Pt in contact with ionomer, which is most likely due to MEA to MEA variability. Dry conditions show an initial slight increase in the double layer capacitance from BOL to 100 cycles followed by a decrease. This might be attributed to a higher Pt area becoming exposed to the ionomer at 100 cycles due to carbon corrosion, followed by Pt and ionomer loss as the support degradades after 100 AST cycles.

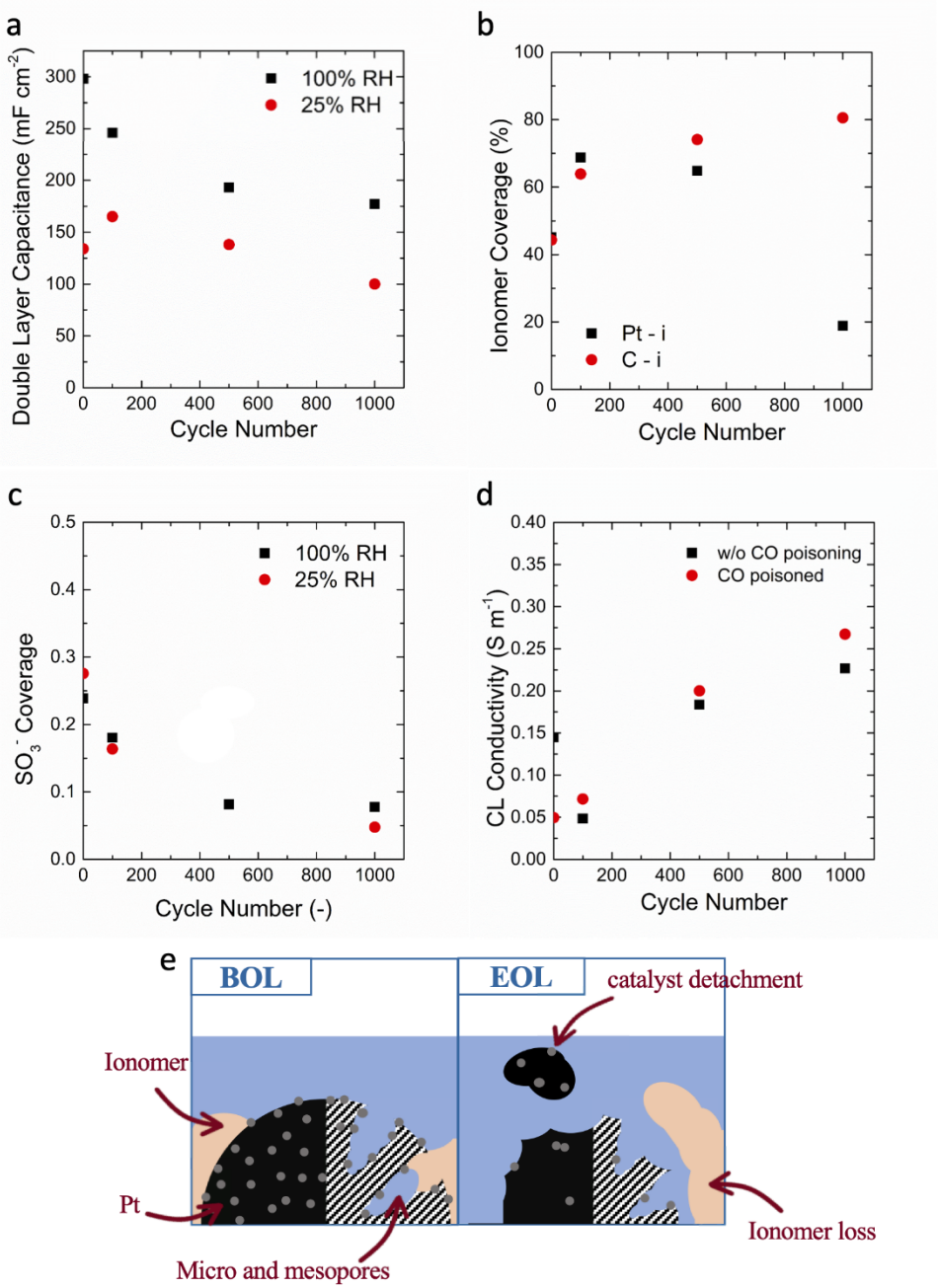


Figure 4-10 a) Double layer capacitance for MEA 2 for humidified and dry conditions, b) ionomer coverage for MEA 2 on platinum and carbon support, c) $SO_3^-$ coverage on Pt surface for the specified RH values, d) catalyst layer conductivity at 25% RH from EIS for MEA 2 with and without CO poisoning. e) A schematic of the proposed mechanism of degradation for the carbon support AST.

Figure 4-10b shows ionomer coverage as a function of number of cycles. At the BOL, the C/i for MEA 2 is 45 %, which is close to the C/i value of 50 %. for MEA 1. However, as already mentioned, Pt/i double layer capacitance is higher for MEA 2 compared to MEA 1 at the BOL. The C/i percentage increases with the cycle number. This increasing trend is due to the reduction in "free" carbon surface after corrosion, increasing the fraction of the total that is contacted by the PFSA polymer. After 1000 cycles, 80 % of carbon surface is covered by ionomer and only 20 % is covered by water. Ionomer coverage on Pt first increases from 45 to 69 % from BOL to 100 cycles, and then decreases to 20 % at 1000 cycles. The Pt/i trend is similar to the dry ECSA and double layer capacitance trends: in the initial cycles more Pt surface is exposed to the ionomer before the drastic degradation of the polymer and support that causes disconnection of both proton and electron pathways.

$SO_3^-$ coverage in wet conditions is similar for MEA 1 and MEA 2 at the BOL. Since more Pt is present on the surface of carbon in MEA 2, the $SO_3^-$ coverage in dry and wet conditions is very similar. The coverage shows a severe decrease of around 90 % over the 1000 cycles. The same trend of decrease in the ECSA was also observed for wet conditions. The CO-stripping charge mostly shows the decreasing trend with increase in the cycle number due to loss of Pt surface area (Figure 4-3b). The absolute value of the CO-displacement charge is very similar for wet and dry conditions and monotonically decreased for MEA 2. Since both CO-displacement and stripping charges decreased with AST cycling number, the net $SO3^-$ coverage decrease is large, indicating the loss of Pt/i interface due to both Pt and ionomer loss (Figure 4-3b). From XPS data in Figure 4-4b, the intensity of C-F bond peak is significantly reduced for MEA 2 compared to Baseline, indicating the loss of the side chains in the ionomer. The fluorine content is reduced but sulfur atomic relative percentage is extremely low, showing additional proof of ionomer degradation.

Ionomer loss for MEA 2 is larger than that of MEA 1 (Pt dissolution AST case). We can attribute this to higher potential of the carbon corrosion AST and therefore an enhanced production of radicals which offers much harsher conditions to the polymer. One might argue if this could be factored in to attribute the source of degradation that comes from this type of accelerated stress tests: the effect of ionomer loss and the disconnection of pathways for protons might be of the same order of magnitude compared to the loss of active material and ECSA. This is reflected directly in the loss of polarization as shown in Figure 4-9c.

Catalyst layer conductivity from Figure 4-10d shows a monotonic increasing trend that can be explained by the thinning of the catalyst layer due to carbon corrosion, leaving shorter ionic pathways that results in a better ionic conductivity. The thickness reduction in the catalyst layer after carbon corrosion experiment is shown by Figure 4-11.

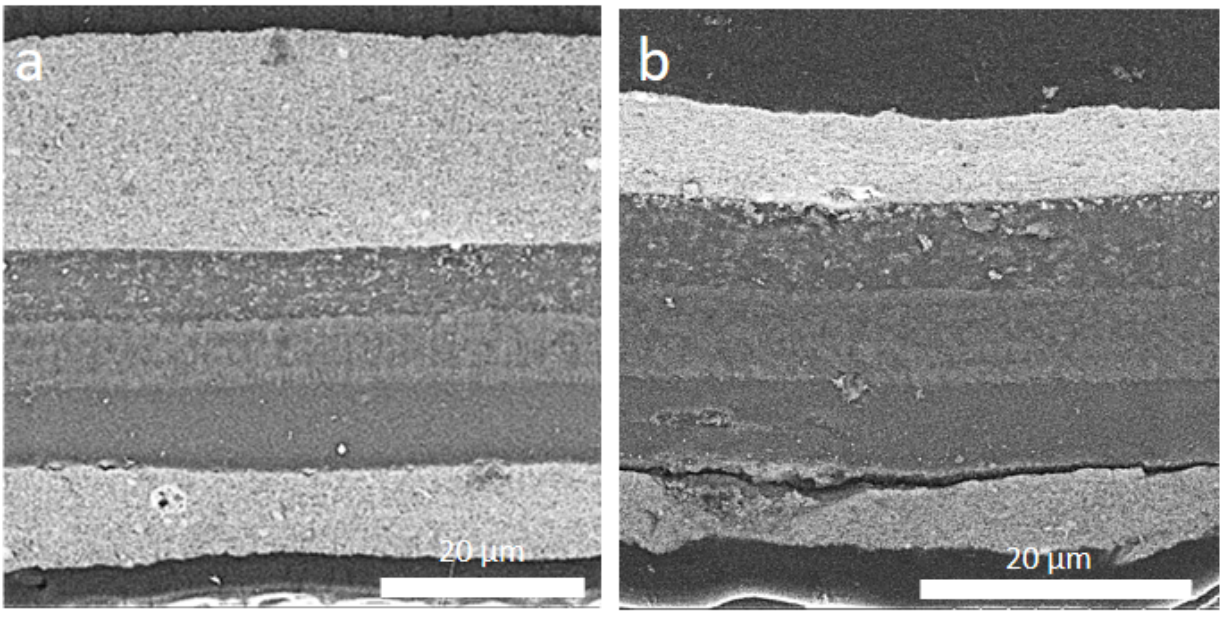


Figure 4-11 SEM cross section to show the effect of carbon corrosion: a) Pristine, high surface area carbon b) MEA 2 after carbon corrosion.

As summarized in Figure 4-10e, during support AST, the high potential the cathode is subjected to leads to the corrosion of the carbon in the electrode, resulting in the detachment of catalyst particles with the loss of active sites. At the same time, both for mechanical degradation and chemical attack, the ionomer is also deteriorating, progressively eliminating access for protons to the remaining active Pt sites. The two combined effects lead to a severe loss in polarization performance, as well as a sharp ECSA loss in the first hundred of cycles.

Carbon corrosion AST on MEA 3 was performed to show the behavior of a corrosion-tolerant cathode compared to the high surface area carbon of MEA 2. Figure a displays the polarization performance during the first 2500 AST cycles. The cycling was interrupted between 2500 and 5000 cycles due to a shunt that short circuited the cell, unrelated to the degradation phenomena. In this set of polarization curves, it is possible to see how both the activation and ohmic regions are not changing significantly and therefore we can assume both kinetic properties and electric conductivity are preserved in the cell.

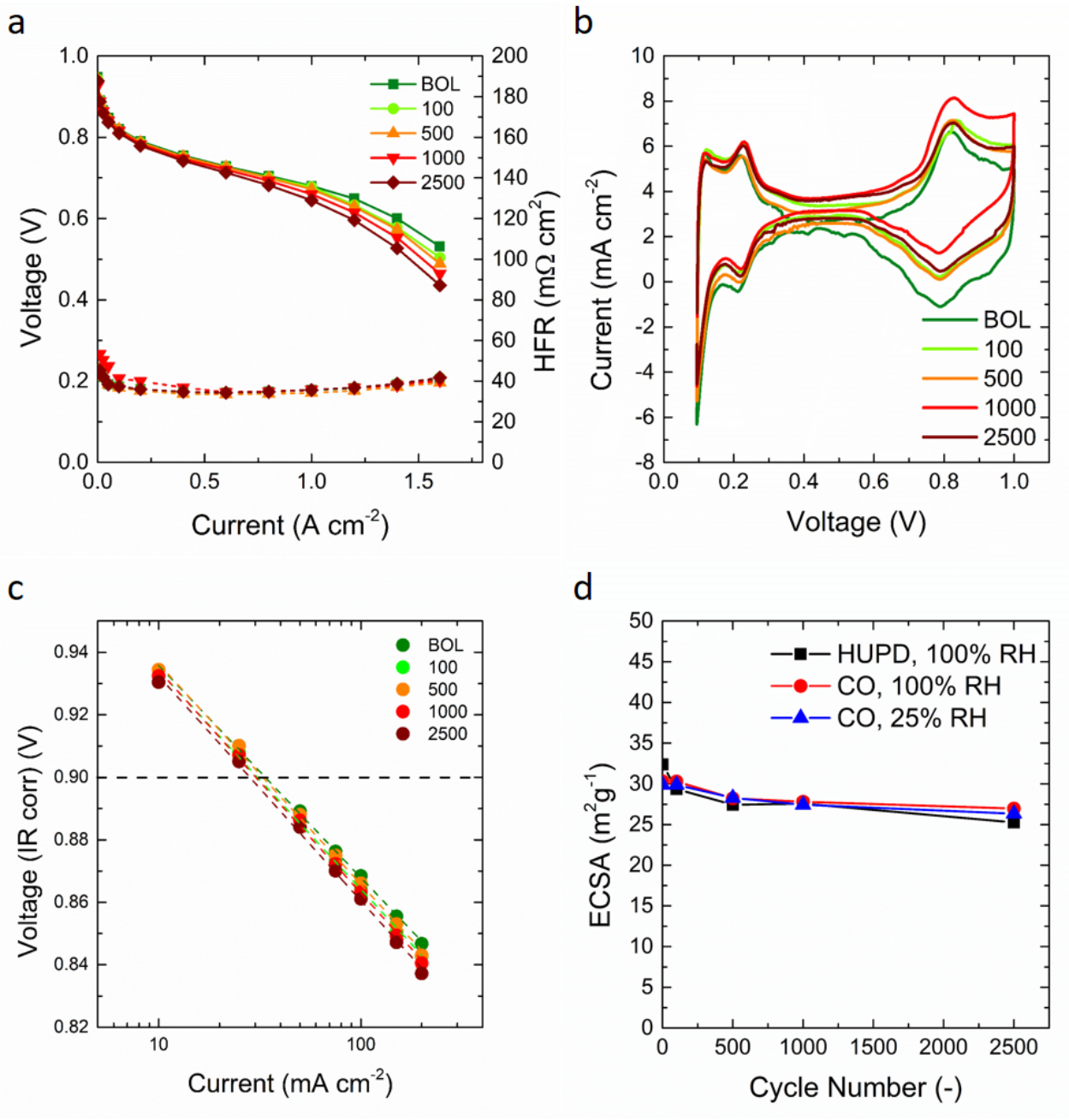


Figure 4-12 Electrochemical properties of MEA 4 collected at different stages of carbon corrosion AST: a) polarization curves, b) cyclic voltammograms c) mass activity plots from oxygen polarization curves, d) evolution of the ECSA determined by both HUPD region of the $H_2/N_2$ CV and CO stripping charge at indicated RH.

From $H_{UPD}$ region in Figure 4-12b, no dramatic change in the Pt features is observed, and from mass activity plots in Figure 4-12c, the current values at 0.9 V show little change overall, indicating only minor decrease in the kinetic performance of the catalyst. The measured Tafel slopes do not change significantly with cycling, increasing from 67.9 mV $dec^{-1}$ at the BOL to 71.9 mV $dec^{-1}$ at 2,500 cycles. Degradation is mostly limited to the high current density region, where the cell shows mass transport limitations. This might be due to carbon oxidation and flooding. The ECSA measured with $H_{UPD}$ and CO-stripping is plotted as a function of AST cycle number. BOL ECSA is measured to be around 30 $m^2$ $g^{-1}$ for both 100 % and 25 % RH. This stability comes at the cost of a lower initial ECSA: graphitized carbon generally is less porous compared to other types of support [153] and it is more difficult to disperse Pt uniformly on it. For this graphitized cathode carbon support, most of the Pt is on the surface of carbon because graphitized support has minimum amount of meso- and micro-pores [153]. After 2,500 carbon corrosion AST cycles, the ECSA decreased to 27.5 $m^2$ $g^{-1}$, which is a negligible loss of surface area, showing that the graphitized support is very durable. Table 4-5 also reveals that mass activity and specific activities show virtually no change with number of cycles, again indicating that the graphitized support is very well designed to protect Pt from dissolution.

Table 4-5 Slope and $i_{0.9V}$ from IR corrected I-V curves in $H_2/O_2$ for MEA 3.

| Cycles | Tafel Slope, absolute value (mV $dec^{-1}$) | $i_{0.9V}$ (mA $cm^{-2}_{geo}$) | Mass Activity (mA $mg^{-1}$) | Specific Activity (mA $cm^{-2}_{Pt}$) |
|---|---|---|---|---|
| 0 | 67.9 | 33.79 | 112.6 | 0.278 |
| 100 | 70.1 | 30.88 | 102.9 | 0.255 |
| 500 | 70.6 | 32.88 | 109.6 | 0.291 |
| 1000 | 71.3 | 30.24 | 100.8 | 0.270 |
| 2500 | 71.9 | 28.31 | 94.37 | 0.263 |

Figure 4-13a shows the double layer capacitance for MEA 3 in both 100 % and 25 % RH. Although, most of Pt is on the surface of carbon, not all of it is in contact with ionomer, as there is about two times higher double layer capacitance at 100 % RH compared to 50 % RH. The BOL double layer capacitance in 100 % RH is 95 mF $cm^{-2}$, which is three times less than for MEAs 1 and 2. The graphitized support has lower double layer capacitance due to non-porous nature of the carbon, lower Pt surface area reducing Pt's contribution to the double layer capacitance. The double layer capacitance for 100 % RH first increases to 120 mF $cm^{-2}$ at 1,000 cycles and then reduces to 85 mF $cm^{-2}$ at 2,500 cycles. The increase in double layer capacitance during first 1,000 cycles is most likely due to oxidation and wetting of carbon. The double layer capacitance for 25 % RH stayed about 50 mF $cm^{-2}$ for the entire AST, indicating very stable C/i and Pt/i interface. The ionomer coverage on carbon is as high as 80 % or more, which is much higher than that of MEA 1 or 2, as there are no pores within graphitized carbon and most of the carbon surface is in

contact with ionomer. The Pt/i coverage is also higher for MEA 3 compared to MEAs 1 and 2, as most of the Pt is on the surface of carbon and is accessed by the ionomer. At the BOL, 50 % of Pt is in contact with ionomer and after 2,500 cycles, it increases to 58 %. $SO_3^-$ coverage on the other hand (Figure 4-13c), is only about 10 % at the BOL which is much lower compared to MEA 1 or 2. High value of Pt/i double layer capacitance and low $SO_3^-$ coverage is most likely due to the different ionomer orientation near the surface of Pt. Carbon wettability also controls ionomer orientation near the surface [138,139].

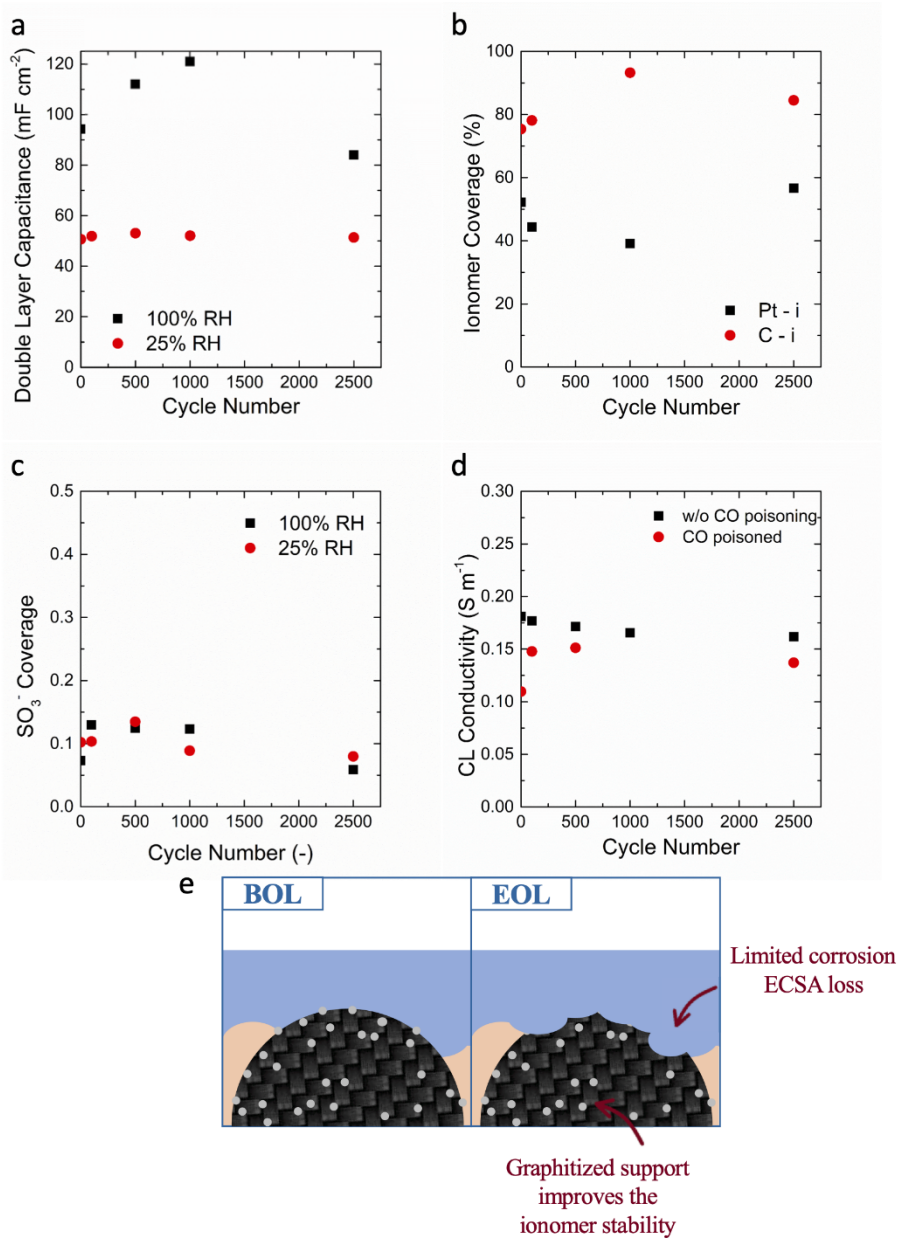


Figure 4-13 a) Double layer capacitance for MEA 3 for humidified and dry conditions, b) ionomer coverage for MEA 3 on platinum and carbon support, c) $SO_3^-$ coverage on Pt surface for the specified RH values, d) catalyst layer conductivity at 25% RH from EIS for MEA 3 with and without CO poisoning. e) A schematic of the proposed mechanism of degradation for the carbon support AST.

CO-displacement charge is very similar for 25 % and 100 % RH. CO-stripping charge is also similar for 25 and 100 % RH (Figure 4-3d and Table 4-3). Nevertheless, although the ECSA remained constant after 2,500 cycles, CO-displacement charge reduced at both RH conditions. For this MEA, the ionomer is most likely to degrade due to radicals' formation and chemical attack alone, rather than the combined effects together with the loss of carbon support or Pt ECSA. Figure 4-14 represents XPS spectra for this MEA compared to the Baseline which was identical for MEA 1 and 2.

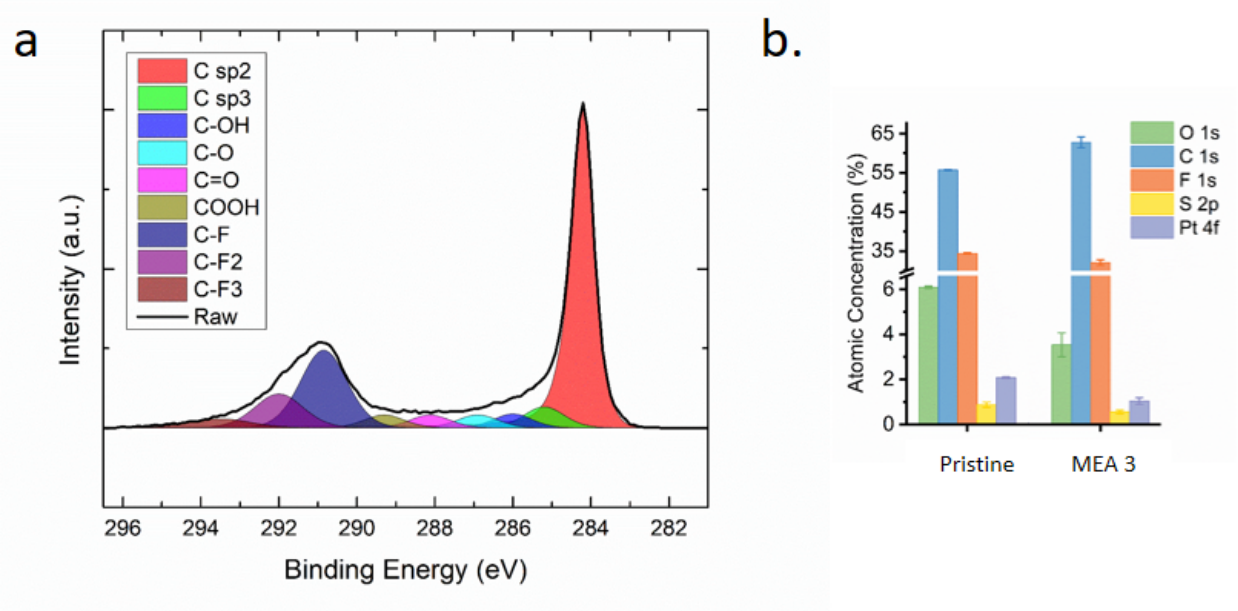


Figure 4-14: a) XPS for carbon for MEA 3 after carbon corrosion AST, b) elemental survey for the same MEA.

Higher content of carbon and lower content of oxygen as well as the signature of graphitized carbon support can clearly be seen in MEA 3 XPS spectra. Lower sulfur (S) signal can be an indicative of ionomer degradation. This MEA also exhibits higher catalyst layer ionic conductivity

at the BOL (Figure 4-13d) compared to MEAs 1 and 2 which is due to the better ionomer coverage on the low surface area of carbon, as shown earlier by Ramaswamy et al.[20]. Ionic conductivity does not change significantly with cycling, when no CO was introduced into the system. To summarize, as opposed to high surface area carbon, this class of graphitized support catalysts (Figure 4-13e), not only has a better tolerance to corrosion, which prevents Pt from detachment, but at the same time helps keep the polymer adhesion, maintain the ionomer content in the electrode, preserve ionic pathways and ionic conductivity, and prevent further polarization loss.

## 4.4 Summary

This chapter aimed to understand the evolution of Pt-ionomer and carbon-ionomer interfaces undergoing catalyst AST and carbon corrosion AST. Two MEAs with HSA carbon support on the cathode were subjected to the ASTs of DOE platinum dissolution protocol in air environment one of which was under gas starving condition. Two MEAs, one with HSA and one with durable graphitized carbon support (LSA support), underwent carbon corrosion AST. Electrochemical characterization at different stages of the ASTs was performed and ionomer and $SO_3^-$ coverage on Pt were investigated. Double layer capacitance, ionomer and $SO_3^-$ coverages were measured in wet (100% RH) and dry (25% RH) conditions. And furthermore, Pt/i and C/i interfaces were elucidated by use of CO poison during EIS measurements. In wet conditions all Pt and carbon is contacted by either ionomer or condensed water. In dry conditions Pt and C that is not contacted by ionomer will not be detected. This study was the first one to understand Pt/i, C/i, Pt/ w and C/w interfaces evolution during ASTs.

Pt dissolution AST performed on a HSA carbon support cathode (MEA 1) revealed a limited polarization loss throughout polarization curve (<70 mV), most likely attributed to the ECSA decrease under wet conditions, which was around 50% from the BOL to the EOL, defined by 30,000 AST cycles. For this MEA with HSA carbon support the following observations were obtained:

- Most of the Pt nanoparticles were in the micro- and meso-pores, as detailed by differences in ECSA (40 vs. 10 $m^2 g^{-1}$ for wet vs. dry) and double layer capacitances (300 vs. 75 mF $cm^{-2}$) in wet and dry conditions.
- Pt that was not in contact with ionomer (in micro- and meso- pores) degraded more compared to Pt in contact with ionomer, as evidenced by ECSA loss, double layer capacitances and ionomer coverage for wet and dry conditions.
- For dry conditions no Pt ECSA loss was observed during AST, indicating that Pt in contact with ionomer did not degrade significantly
- Ionomer degradation was observed especially for 30,000 cycles, resulting in both Pt/i interface loss and also loss in $SO3^-$ coverage. Ionomer degradation was also confirmed with the XPS study.

MEA 4 was identical to MEA 1 but was cycled with catalyst AST under starving conditions for gas-flow. Significantly higher degradation rate was observed for MEA 4 due to larger ECSA loss and also larger polarization loss where the ECSA decreased by 60–63% and the cell voltage was reduced by more than 100 mV in some polarization regions at EOL. MEA 4 results indicate that gas flow-rates during catalyst ASTs are important as if flow-rates are low heterogeneous degradation of catalyst can happen.

Carbon corrosion AST was performed on MEA 2 that had HSA carbon support. The polarization curve showed a sharp voltage decrease be- tween 100 and 500 cycles, and the cell had to be stopped early, after 1000 cycles due to lack of performance. The following were observed:

- Majority of polarization loss occurred at 100 and 500 AST cycles. This loss cannot be explained purely by Pt agglomeration and detachment (ECSA loss). This polarization loss (~160mV at 0.2 A $cm^{-2}$) was mostly due to a combination of ionomer loss, carbon loss and Pt detachment.
- Significant loss of carbon was observed during the 1000 cycles, and catalyst layer thickness was reduced by half. Because of the loss of carbon the C/i interface increased from 45% at the BOL to 80% at the EOL (defined by 1000 support AST cycles).
- Pt was lost regardless whether it was in contact with ionomer or water. This is indicative of Pt agglomeration and mechanical detachment or isolation from electric or ionic domains.
- Pt/i interface dramatically decreased from 65% at 500 cycles to 20% at 1000 cycles. This is indicative of ionomer loss, as confirmed by XPS study. $SO_3^-$ coverage monotonically decreased throughout the cycling indicating both Pt loss and also ionomer loss.

As a comparison, the same support AST was performed on a graphitized carbon support. MEA 3 performed without any seeming degradation up to 2500 cycles, but it was shut down after that due to an unexpected short circuit that ended the cell's life. In this MEA, platinum ECSA was smaller than that for MEAs 1 and 2 having high surface area carbon as larger fraction of Pt was on the surface of carbon support, indicating a smaller amount of meso and micropores within the carbon support. Differently from the previous case, here both performance and ionomer coverage were preserved through the cycling. The effect of a stable support is not

only to mitigate the corrosion and the consequent ECSA loss, but also to offer a better anchoring to ionomer and preservation of ionic connection and proton availability.

# Chapter 5

# Conclusion, Contributions and Recommendations for Future work

## 5.1 Conclusions

This dissertation studied the fundamentals of ORR and transport properties of the catalyst layer in PEFC from kinetics and morphological point of view. Three-electrode set-up measurements in acidic electrolyte was performed on Pt polycrystalline extended surface and Pt nanoparticles where the loading of Pt was high on the carbon support surface. To gain mechanistic insight into ORR, kinetic isotope effect approach was applied. Understanding of ORR mechanism and kinetics unraveled the rational design of more efficient electrocatalysts towards ORR by inducing nanoconfinements for better transport of ions and oxygen. Nanoconfinement was then explored from the perspective of ORR and Knudsen diffusion of air molecules and ion transport in the nanopores based on the EDL thickness (Debye length), ionic strength of the material, and pore sizes. Then, a novel approach based on IL integration into the catalyst layer was used to accommodate oxygen and proton transport in porous electrodes of PEFCs. This wholistic approach included ink and IL amount optimization, preliminary testing with RDE, then MEA fabrication and rigorous testing within PEFC hardware. Analytical and physiochemical characterizations brought insight into the ionomer|IL interface in presence of confinement. In addition, two in-situ experimental methodologies along with XPS characterization provided quantitative data on Pt|ionomer and carbon|ionomer interfaces evolution during catalyst and carbon corrosion ASTs on

Pt supported on HSA and graphitized carbon. These methods were based on the double layer capacitance measurements and combination of CO displacement and CO stripping procedures. The following subsections summarize the developments and findings of this research.

### 5.1.1 Confinement Effects for Nano-electrocatalysts for Oxygen Reduction Reaction

1- Confinement is induced by ionomer, ionic liquids or molecular additives and its impact on electrocatalyst reactivity and transport properties is currently not well understood.

2- Modifiers impact the ORR activity in practical fuel cell application as the studies showed higher mass and specific activities for modified commercial catalysts. Activity improvements are due to the induced hydrophobic microenvironment and improved proton conductivity.

3- Interpretation of nanoconfinements and their role on ion conductivity and water molecules repulsion from Pt surface in the presence of different modifiers can help understanding the ORR kinetics dependence on the morphology of the carbon-supported electrocatalyst.

### 5.1.2 Kinetic Isotope Effect as a Tool to Investigate the Oxygen Reduction Reaction on Pt-based Electrocatalysts. Part I: High-loading Pt/C and Pt Extended Surface

1- KIE is defined as the ratio of the kinetic current measured in protonated electrolyte vs. deuterated electrolyte. KIE larger than one indicates protons participation in the rate-determining step of ORR.

2- Kinetic currents can be calculated by Koutecky-Levich equation using currents measured in the mass transport limited potential regime of the ORR and Tafel approximation to Butler-Volmer equation extrapolated to low-magnitude overpotentials where the reaction is kinetically limited.

3- A KIE of 1 was observed for Pt/C (with a 40 wt. % Pt loading) and poly-Pt, thus indicating that, on 40 wt. % Pt/C and Pt-poly, the rate determining step is proton independent.

4- The effect of the poisoning anions on the platinum rate determining step was investigated by assessing the KIE in perchloric (non-poisoning) and sulfuric acid-based electrolytes. Both measurements showed KIE of ca. 1 indicating that poisoning effect of $SO_3^-$ groups does not impact the ratio that determines KIE.

### 5.1.3 Ionic Liquids in Polymer Electrolyte Fuel Cells: New State-of-the-art in the Oxygen Reduction Reactivity and Durability

1- In order to investigate the effect of chemical structure on interfacial interactions and electrochemical properties of the CL, three Imidazolium-based ILs were impregnated in HSA commercial Pt/C catalyst.

2- Nitrogen physisorption along with TEM imaging of IL-modified powders revealed that most of the nanoparticles were well-covered by the ILs.

3- Intramolecular interactions between the IL molecules and Nafion domains were studied using zeta potential and hydrophobicity degree of the CL showing that ($[C_4mim]^+[NTf_2]^-$) has the smallest electrostatic repulsion with Nafion chains.

4- Modified Pt/C-($[C_4mim]^+[NTf_2]^-$) electrocatalyst with optimized CL microstructure and highest hydrophobicity improved ORR kinetics; the optimized Pt|modifier interface showed i) noticeably higher proton diffusivity in the CL, ii) suppression of surface-oxygenated species (OHad and $O_{ad}$) formation, iii) interfacial hydrogen-bonding between IL's cation and adsorbed intermediate oxygenated species of ORR.

5- Pt/C-($[C_4mim]^+[NTf_2]^-$) catalyst showed ORR activity enhancement in RDE setup.

6- Our ($[C_4mim]^+[NTf_2]^-$)-modified MEA with optimal hydrophobicity, proton conductivity, and oxygen transport resistance achieved a peak power density of 0.909 W $cm^{-2}$ at 64% voltage efficiency, and enhanced MA and SA by 20% and 75%, respectively.

7- Higher proton conductivity comes at the expense of larger oxygen transport resistance. Therefore, based on the MEA design needs, an optimal point should be selected which was the case for MEA containing ($[C_4mim]^+[NTf_2]^-$) in this work.

8- ILs have a predominant role in protecting Pt surface from $SO_3^-$ poisoning.

9- All IL-containing MEAs provided a stable electrocatalyst|modifier|ionomer system that could tolerate load cycling durability, per DOE-specified protocols. Superior durability after 30k catalyst AST cycling was due to i) high ECSA retention, ii) limiting redeposition of the Pt not in contact with the ionomer (within the pores), iii) proton conductivity of remaining IL molecules within the pores after Nafion degradation.

### 5.1.4 Investigation of Cathode Catalyst Layer Interfaces Evolution during Accelerated Stress Tests for Polymer Electrolyte Fuel Cells

1- The evolution of Pt|ionomer and catbon|ionomer during catalyst AST and carbon corrosion were quantified using double layer capacitance measurements in dry and wet conditions combined with CO poisoning.

2- HSA carbon support can host up to 75% of Pt active surface area within the mesopores. This fraction of Pt is not in contact with ionomer and degrade more compared to the ones in contact with ionomer.

3- XPS data together with $SO_3^-$ coverage results revealed the ionomer degradation during AST as it losses the side chains and $SO_3^-$ groups.

4- Carbon corrosion on HSA support showed severe decrease in ECSA, $SO_3^-$ coverage and Pt|ionomer interface with cycling number. SEM imaging also revealed thinning of the catalyst layer. These results indicate Pt detachment and ionomer degradation that is due to higher production of radicals under harsh condition and mechanical deterioration of polymer. They eventually led to disconnection of electron and proton pathways and loss of performance.

5- In graphitized carbon most of the Pt and carbon are in contact with ionomer because there are no micro and mesopores. It is more durable compared to HSA supports as Pt|ionomer and carbon|ionomer interfaces were pretty stable. Graphitized support provides better tolerance to carbon corrosion by preserving ionic pathways and keeping ionomer anchored to the support.

## 5.2 Recommendations for Future Work

1- It would be beneficial to utilize KIE to study the effect of carbon support morphology on rate determining step of ORR. For example, how induced nanoconfinement using ILs, Pt nanoparticles dispersion on carbon support and agglomeration states can change KIE.

2- It would be interesting to evaluate the viscosity of IL-containing inks. Viscosity depends on catalyst powder degree of agglomeration, aggregation of ionomer in presence of ILs, and how the ink solvent ratios affect the ionomer|IL-modified catalyst interface and interactions. Rheological evaluation with rheometer will help the goal of optimizing the ink recipe to achieve the best electrode microstructure.

3- We have only performed catalyst AST on IL-modified MEAs. Evaluation of CL performance under carbon corrosion and start-up shut-down with intermittent performance evaluation would reveal how promising IL modification will be in real-life automotive industry.

4- To quantify the IL leaching during AST, amount of dissolved IL in water can be measured from cathode outlet. This data combined with XPS, elemental survey, and in-situ measurements in dry and wet conditions can help understand the evolution of Pt|IL interface during AST.

5- Molecular dynamics simulations can be used to explore the interfacial interactions between IL molecules, Pt surface, and Nafion chains.

5- Although small molecule ILs showed superb durability, a stable Poly-(IL)|Nafion system may have longer life-time.

6- A better understanding of proton conduction mechanism in ILs, specifically at high current densities, is crucial and indeed requires further improvements. This can be done by deep fundamental analysis and modeling efforts to unravel the interfacial phenomena.

## Reference


1. Avid, A. *et al.* Surface modification of MWCNT and its influence on properties of paraffin/MWCNT nanocomposites as phase change material. *J. Appl. Polym. Sci.* **137**, 48428 (2020).

2. Lüthi, D. *et al.* High-resolution carbon dioxide concentration record 650,000–800,000 years before present. *Nature* **453**, 379–382 (2008).

3. Kiss, J. T., Bellér, G., Árpád, I. & Kocsis, D. Trends in Greenhouse Gas Emissions and Renewable Energy Policies in the EU and USA, with Special Emphasis on the Transportation Sector. *Műszaki és Menedzsment Tudományi Közlemények* **5**, (2020).

4. Zohuri, B. Hydrogen-Powered Fuel Cell and Hybrid Automobiles of the Near Future BT - Hydrogen Energy: Challenges and Solutions for a Cleaner Future. in (ed. Zohuri, B.) 37–59 (Springer International Publishing, 2019). doi:10.1007/978-3-319-93461-7_2

5. Lindorfer, J., Rosenfeld, D. C. & Böhm, H. 23 - Fuel Cells: Energy Conversion Technology. in (ed. Letcher, T. M. B. T.-F. E. (Third E.) 495–517 (Elsevier, 2020). doi:https://doi.org/10.1016/B978-0-08-102886-5.00023-2

6. Lee, D.-Y., Elgowainy, A., Kotz, A., Vijayagopal, R. & Marcinkoski, J. Life-cycle implications of hydrogen fuel cell electric vehicle technology for medium- and heavy-duty trucks. *J. Power Sources* **393**, 217–229 (2018).

7. Wang, Y., Ruiz Diaz, D. F., Chen, K. S., Wang, Z. & Adroher, X. C. Materials, technological status, and fundamentals of PEM fuel cells – A review. *Mater. Today* **32**, 178–203 (2020).

8. Huang, J., Li, Z. & Zhang, J. Review of characterization and modeling of polymer electrolyte fuel cell catalyst layer: The blessing and curse of ionomer. *Front. Energy* **11**, 334–364 (2017).

9. Litster, S. & McLean, G. PEM fuel cell electrodes. *J. Power Sources* **130**, 61–76 (2004).

10. Ejigu, A. & Walsh, D. A. Electrocatalysis in Room Temperature Ionic Liquids BT - Electrochemistry in Ionic Liquids: Volume 2: Applications. in (ed. Torriero, A. A. J.) 483–506 (Springer International Publishing, 2015). doi:10.1007/978-3-319-15132-8_17

11. Weber, A. Z. *et al.* A Critical Review of Modeling Transport Phenomena in Polymer-Electrolyte Fuel Cells. *J. Electrochem. Soc.* **161**, F1254–F1299 (2014).

12. Ruvinskiy, P. S., Bonnefont, A., Pham-Huu, C. & Savinova, E. R. Using Ordered Carbon Nanomaterials for Shedding Light on the Mechanism of the Cathodic Oxygen Reduction Reaction. *Langmuir* **27**, 9018–9027 (2011).

13. Nørskov, J. K. *et al.* Origin of the Overpotential for Oxygen Reduction at a Fuel-Cell Cathode. *J. Phys. Chem. B* **108**, 17886–17892 (2004).

14. Kulkarni, A., Siahrostami, S., Patel, A. & Nørskov, J. K. Understanding Catalytic Activity Trends in the Oxygen Reduction Reaction. *Chem. Rev.* **118**, 2302–2312 (2018).

15. Debe, M. K. Electrocatalyst approaches and challenges for automotive fuel cells. *Nature* **486**, 43 (2012).

16. Kongkanand, A. & Mathias, M. F. The Priority and Challenge of High-Power Performance of Low-Platinum Proton-Exchange Membrane Fuel Cells. *J. Phys. Chem. Lett.* **7**, 1127–1137 (2016).

17. Wang, X. X., Swihart, M. T. & Wu, G. Achievements, challenges and perspectives on cathode catalysts in proton exchange membrane fuel cells for transportation. *Nat. Catal.* **2**, 578–589 (2019).

18. Cullen, D. A. *et al.* New roads and challenges for fuel cells in heavy-duty transportation. *Nat. Energy* **6**, 462–474 (2021).

19. Marcinkoski, J. *et al.* Hydrogen Class 8 Long Haul Truck Targets. 1–31 (2019).

20. Ramaswamy, N., Gu, W., Ziegelbauer, J. M. & Kumaraguru, S. Carbon Support Microstructure Impact on High Current Density Transport Resistances in PEMFC Cathode. *J. Electrochem. Soc.* **167**, 64515 (2020).

21. Lazaridis, T. & Gasteiger, H. A. Pt-Catalyzed Oxidation of PEMFC Carbon Supports: A Path to Highly Accessible Carbon Morphologies and Implications for Start-Up/Shut-Down Degradation. *J. Electrochem. Soc.* **168**, 114517 (2021).

22. Perego, A. *et al.* Investigation of Cathode Catalyst Layer Interfaces Evolution during Accelerated Stress Tests for Polymer Electrolyte Fuel Cells. *Appl. Catal. B Environ.* 120810 (2021). doi:https://doi.org/10.1016/j.apcatb.2021.120810

23. Qiao, M. *et al.* Boosting the Oxygen Reduction Electrocatalytic Performance of Nonprecious Metal Nanocarbons via Triple Boundary Engineering Using Protic Ionic Liquids. *ACS Appl. Mater. Interfaces* **11**, 11298–11305 (2019).

24. Grommet, A. B., Feller, M. & Klajn, R. Chemical reactivity under nanoconfinement. *Nat. Nanotechnol.* **15**, 256–271 (2020).

25. Tesfaye, M. Understanding the Impact of Confinement on Ionomer Thin Film Transport

Properties. (UC Berkeley, 2019).

26. Kodama, K. *et al.* Effect of the Side-Chain Structure of Perfluoro-Sulfonic Acid Ionomers on the Oxygen Reduction Reaction on the Surface of Pt. *ACS Catal.* **8**, 694–700 (2018).

27. Song, Z., Cao, X. & Huang, H. Electroneutral models for a multidimensional dynamic Poisson-Nernst-Planck system. *Phys. Rev. E* **98**, 32404 (2018).

28. Krämer, G., Hausen, F. & Bennewitz, R. Dynamic shear force microscopy of confined liquids at a gold electrode. *Faraday Discuss.* **199**, 299–309 (2017).

29. Tokuda, H., Tsuzuki, S., Susan, M. A. B. H., Hayamizu, K. & Watanabe, M. How Ionic Are Room-Temperature Ionic Liquids? An Indicator of the Physicochemical Properties. *J. Phys. Chem. B* **110**, 19593–19600 (2006).

30. Zenyuk, I. V. Interfaces in Polymer Electrolyte Fuel Cells. (Carnegie Mellon University, 2013).

31. Kumar, R. *et al.* Capacitance of thin films containing polymerized ionic liquids. *Sci. Adv.* **6**, eaba7952 (2020).

32. Yang, Y. D., Moon, G. J., Oh, J. M. & Kang, I. S. Discrete and Continuum Analyses of Confinement Effects of an Ionic Liquid on the EDL Structure and the Pressure Acting on the Wall. *J. Phys. Chem. C* **123**, 2516–2525 (2019).

33. Nishi, N. *et al.* Potential-Dependent Structure of the Ionic Layer at the Electrode Interface of an Ionic Liquid Probed Using Neutron Reflectometry. *J. Phys. Chem. C* **123**, 9223–9230 (2019).

34. Klein, J. M., Panichi, E. & Gurkan, B. Potential dependent capacitance of [EMIM][TFSI],

[N1114][TFSI] and [PYR13][TFSI] ionic liquids on glassy carbon. *Phys. Chem. Chem. Phys.* **21**, 3712–3720 (2019).

35. Katakura, S., Nishi, N., Kobayashi, K., Amano, K. & Sakka, T. Surface Structure of Quaternary Ammonium-Based Ionic Liquids Studied Using Molecular Dynamics Simulation: Effect of Switching the Length of Alkyl Chains. *J. Phys. Chem. C* **123**, 7246–7258 (2019).

36. Watanabe, S. *et al.* Interfacial structuring of non-halogenated imidazolium ionic liquids at charged surfaces: effect of alkyl chain length. *Phys. Chem. Chem. Phys.* **22**, 8450–8460 (2020).

37. Avni, Y., Adar, R. M. & Andelman, D. Charge oscillations in ionic liquids: A microscopic cluster model. *Phys. Rev. E* **101**, 10601 (2020).

38. Feng, G. *et al.* Free and Bound States of Ions in Ionic Liquids, Conductivity, and Underscreening Paradox. *Phys. Rev. X* **9**, 21024 (2019).

39. Begić, S., Chen, F., Jónsson, E. & Forsyth, M. Overscreening and crowding in electrochemical ionic liquid systems. *Phys. Rev. Mater.* **3**, 95801 (2019).

40. Mao, X. *et al.* Self-assembled nanostructures in ionic liquids facilitate charge storage at electrified interfaces. *Nat. Mater.* **18**, 1350–1357 (2019).

41. Bazant, M. Z., Storey, B. D. & Kornyshev, A. A. Double Layer in Ionic Liquids: Overscreening versus Crowding. *Phys. Rev. Lett.* **106**, 46102 (2011).

42. Liu, J. & Zenyuk, I. V. Proton transport in ionomer-free regions of polymer electrolyte fuel cells and implications for oxygen reduction reaction. *Curr. Opin. Electrochem.* **12**,

202–208 (2018).

43. Marion, S., Davis, S. J., Wu, Z.-Q. & Radenovic, A. Nanocapillary confinement of imidazolium based ionic liquids. *Nanoscale* **12**, 8867–8874 (2020).

44. Chen, D., Kongkanand, A. & Jorne, J. Proton Conduction and Oxygen Diffusion in Ultra-Thin Nafion Films in PEM Fuel Cell: How Thin? *J. Electrochem. Soc.* **166**, F24–F33 (2019).

45. Ono, Y. & Nagao, Y. Interfacial Structure and Proton Conductivity of Nafion at the Pt-Deposited Surface. *Langmuir* **32**, 352–358 (2016).

46. Paul, D. K., McCreery, R. & Karan, K. Proton Transport Property in Supported Nafion Nanothin Films by Electrochemical Impedance Spectroscopy. *J. Electrochem. Soc.* **161**, F1395–F1402 (2014).

47. Kusoglu, A., Dursch, T. J. & Weber, A. Z. Nanostructure/Swelling Relationships of Bulk and Thin-Film PFSA Ionomers. *Adv. Funct. Mater.* **26**, 4961–4975 (2016).

48. Eastman, S. A. *et al.* Effect of Confinement on Structure, Water Solubility, and Water Transport in Nafion Thin Films. *Macromolecules* **45**, 7920–7930 (2012).

49. Knudsen, M. Die Molekularströmung der Gase durch Offnungen und die Effusion. *Ann. Phys.* **333**, 999–1016 (1909).

50. Scorrano, G. *et al.* Gas Flow at the Ultra-nanoscale: Universal Predictive Model and Validation in Nanochannels of Ångstrom-Level Resolution. *ACS Appl. Mater. Interfaces* **10**, 32233–32238 (2018).

51. Debe, M. K. Effect of Electrode Surface Area Distribution on High Current Density

Performance of PEM Fuel Cells. *J. Electrochem. Soc.* **159**, B53–B66 (2011).

52. Gewirth, A. A. & Thorum, M. S. Electroreduction of Dioxygen for Fuel-Cell Applications: Materials and Challenges. *Inorg. Chem.* **49**, 3557–3566 (2010).

53. Wroblowa, H. S., Yen-Chi-Pan & Razumney, G. Electroreduction of oxygen: A new mechanistic criterion. *J. Electroanal. Chem. Interfacial Electrochem.* **69**, 195–201 (1976).

54. Huang, J., Zhang, J. & Eikerling, M. Unifying theoretical framework for deciphering the oxygen reduction reaction on platinum. *Phys. Chem. Chem. Phys.* **20**, 11776–11786 (2018).

55. Gómez-Gallego, M. & Sierra, M. A. Kinetic Isotope Effects in the Study of Organometallic Reaction Mechanisms. *Chem. Rev.* **111**, 4857–4963 (2011).

56. Winkler, F. J. Reaction Rates of Isotopic Molecules. Von L. Melander und W. H. Saunders, Jr. Wiley, New York 1980. XIV, 391 S., geb. £ 16.30. *Angew. Chemie* **93**, 220 (1981).

57. Christensen, N. J. & Fristrup, P. Kinetic Isotope Effects (KIE) and Density Functional Theory (DFT): A Match Made in Heaven? *Synlett* **26**, 508–513 (2015).

58. Ghoneim, M. M., Clouser, S. & Yeager, E. Oxygen Reduction Kinetics in Deuterated Phosphoric Acid. *J. Electrochem. Soc.* **132**, 1160–1162 (1985).

59. Matter, P. H., Biddinger, E. J. & Ozkan, U. S. Non-precious metal oxygen reduction catalysts for PEM fuel cells. in *Catalysis: Volume 20* **20**, 338–366 (The Royal Society of Chemistry, 2007).

60. Malko, D. & Kucernak, A. Kinetic isotope effect in the oxygen reduction reaction (ORR)

over Fe-N/C catalysts under acidic and alkaline conditions. *Electrochem. commun.* **83**, 67–71 (2017).

61. Sakaushi, K. *et al.* Microscopic Electrode Processes in the Four-Electron Oxygen Reduction on Highly Active Carbon-Based Electrocatalysts. *ACS Catal.* **8**, 8162–8176 (2018).

62. Tse, E. C. M., Varnell, J. A., Hoang, T. T. H. & Gewirth, A. A. Elucidating Proton Involvement in the Rate-Determining Step for Pt/Pd-Based and Non-Precious-Metal Oxygen Reduction Reaction Catalysts Using the Kinetic Isotope Effect. *J. Phys. Chem. Lett.* **7**, 3542–3547 (2016).

63. Attard, G. A., Brew, A., Hunter, K., Sharman, J. & Wright, E. Specific adsorption of perchlorate anions on Pt{hkl} single crystal electrodes. *Phys. Chem. Chem. Phys.* **16**, 13689–13698 (2014).

64. Kunimatsu, K., Hanawa, H., Uchida, H. & Watanabe, M. Role of adsorbed species in methanol oxidation on Pt studied by ATR-FTIRAS combined with linear potential sweep voltammetry. *J. Electroanal. Chem.* **632**, 109–119 (2009).

65. Stamenkovic, V., Chou, K. C., Somorjai, G. A., Ross, P. N. & Markovic, N. M. Vibrational Properties of CO at the Pt(111)−Solution Interface: the Anomalous Stark-Tuning Slope. *J. Phys. Chem. B* **109**, 678–680 (2005).

66. Wang, J. X., Markovic, N. M. & Adzic, R. R. Kinetic Analysis of Oxygen Reduction on Pt(111) in Acid Solutions: Intrinsic Kinetic Parameters and Anion Adsorption Effects. *J. Phys. Chem. B* **108**, 4127–4133 (2004).

67. Markovic, N., Gasteiger, H. & Ross, P. N. Kinetics of Oxygen Reduction on Pt(hkl) Electrodes: Implications for the Crystallite Size Effect with Supported Pt Electrocatalysts. *J. Electrochem. Soc.* **144**, 1591–1597 (1997).

68. Garsany, Y., Baturina, O. A., Swider-Lyons, K. E. & Kocha, S. S. Experimental Methods for Quantifying the Activity of Platinum Electrocatalysts for the Oxygen Reduction Reaction. *Anal. Chem.* **82**, 6321–6328 (2010).

69. Kocha, S. S. *et al.* Best Practices and Testing Protocols for Benchmarking ORR Activities of Fuel Cell Electrocatalysts Using Rotating Disk Electrode. *Electrocatalysis* **8**, 366–374 (2017).

70. Garsany, Y., Singer, I. L. & Swider-Lyons, K. E. Impact of film drying procedures on RDE characterization of Pt/VC electrocatalysts. *J. Electroanal. Chem.* **662**, 396–406 (2011).

71. Shinozaki, K., Zack, J. W., Pylypenko, S., Pivovar, B. S. & Kocha, S. S. Oxygen Reduction Reaction Measurements on Platinum Electrocatalysts Utilizing Rotating Disk Electrode Technique: II. Influence of Ink Formulation, Catalyst Layer Uniformity and Thickness . *J. Electrochem. Soc.* **162**, F1384–F1396 (2015).

72. Mayrhofer, K. J. J. *et al.* Measurement of oxygen reduction activities via the rotating disc electrode method: From Pt model surfaces to carbon-supported high surface area catalysts. *Electrochim. Acta* **53**, 3181–3188 (2008).

73. Biegler, T., Rand, D. A. J. & Woods, R. Limiting oxygen coverage on platinized platinum; Relevance to determination of real platinum area by hydrogen adsorption. *J. Electroanal. Chem. Interfacial Electrochem.* **29**, 269–277 (1971).

74. Breiter, M. W. Comparative electrochemical study of hydrogen and deuterium adsorption on platinum. *Trans. Faraday Soc.* **60**, 1445–1449 (1964).

75. Bard, A. J. & Faulkner, L. R. Electrochemical Methods Fundamentals and Applications. *Electrochem. Methods* **2**, 864 (2001).

76. Ivanov, E. V & Abrosimov, V. K. Specific Features of Hydration of Gaseous Nitrogen and Oxygen, Revealed from Data on Their Solubility in Water H/D Isotopomers. *Russ. J. Gen. Chem.* **75**, 1851–1856 (2005).

77. Bard, A., Parsons, R. & Jordan, J. *Standard potentials in aqueous solution. Marcel Dekker, New York. Standard potentials in aqueous solution. Marcel Dekker, New York.* (1985).

78. Dumont, J. H. *et al.* Nitrogen-Doped Graphene Oxide Electrocatalysts for the Oxygen Reduction Reaction. *ACS Appl. Nano Mater.* **2**, 1675–1682 (2019).

79. Kabir, S., Artyushkova, K., Serov, A. & Atanassov, P. Role of Nitrogen Moieties in N-Doped 3D-Graphene Nanosheets for Oxygen Electroreduction in Acidic and Alkaline Media. *ACS Appl. Mater. Interfaces* **10**, 11623–11632 (2018).

80. Shao, Y., Sui, J., Yin, G. & Gao, Y. Nitrogen-doped carbon nanostructures and their composites as catalytic materials for proton exchange membrane fuel cell. *Appl. Catal. B Environ.* **79**, 89–99 (2008).

81. Ding, D. *et al.* Plasma-assisted nitrogen doping of graphene-encapsulated Pt nanocrystals as efficient fuel cell catalysts. *J. Mater. Chem. A* **2**, 472–477 (2014).

82. Zhou, Y. *et al.* Enhancement of Pt and Pt-alloy fuel cell catalyst activity and durability via

nitrogen-modified carbon supports. *Energy Environ. Sci.* **3**, 1437–1446 (2010).

83. Asahi, M., Yamazaki, S., Taguchi, N. & Ioroi, T. Facile Approach to Enhance Oxygen Reduction Activity by Modification of Platinum Nanoparticles by Melamine-Formaldehyde Polymer. *J. Electrochem. Soc.* **166**, F498–F505 (2019).

84. Snyder, J., Fujita, T., Chen, M. W. & Erlebacher, J. Oxygen reduction in nanoporous metal–ionic liquid composite electrocatalysts. *Nat. Mater.* **9**, 904–907 (2010).

85. Zhang, G.-R., Munoz, M. & Etzold, B. J. M. Accelerating Oxygen-Reduction Catalysts through Preventing Poisoning with Non-Reactive Species by Using Hydrophobic Ionic Liquids. *Angew. Chemie Int. Ed.* **55**, 2257–2261 (2016).

86. Snyder, J., Livi, K. & Erlebacher, J. Oxygen Reduction Reaction Performance of [MTBD][beti]-Encapsulated Nanoporous NiPt Alloy Nanoparticles. *Adv. Funct. Mater.* **23**, 5494–5501 (2013).

87. Kabir, S. *et al.* Elucidating the Dynamic Nature of Fuel Cell Electrodes as a Function of Conditioning: An ex Situ Material Characterization and in Situ Electrochemical Diagnostic Study. *ACS Appl. Mater. Interfaces* **11**, 45016–45030 (2019).

88. Harzer, G. S., Schwämmlein, J. N., Damjanović, A. M., Ghosh, S. & Gasteiger, H. A. Cathode Loading Impact on Voltage Cycling Induced PEMFC Degradation: A Voltage Loss Analysis. *J. Electrochem. Soc.* **165**, F3118–F3131 (2018).

89. Macauley, N. *et al.* Carbon Corrosion in PEM Fuel Cells and the Development of Accelerated Stress Tests. *J. Electrochem. Soc.* **165**, F3148–F3160 (2018).

90. Yarlagadda, V. *et al.* Boosting Fuel Cell Performance with Accessible Carbon Mesopores.

*ACS Energy Lett.* **3**, 618–621 (2018).

91. Soboleva, T. *et al.* On the Micro-, Meso-, and Macroporous Structures of Polymer Electrolyte Membrane Fuel Cell Catalyst Layers. *ACS Appl. Mater. Interfaces* **2**, 375–384 (2010).

92. Zenyuk, I. V & Litster, S. Spatially Resolved Modeling of Electric Double Layers and Surface Chemistry for the Hydrogen Oxidation Reaction in Water-Filled Platinum–Carbon Electrodes. *J. Phys. Chem. C* **116**, 9862–9875 (2012).

93. Thompson, E. L. & Baker, D. Proton Conduction on Ionomer-Free Pt Surfaces. *ECS Trans.* **41**, 709–720 (2019).

94. Avid, A. & Zenyuk, I. V. "Confinement effects for nano-electrocatalysts for oxygen reduction reaction". *Curr. Opin. Electrochem.* **25**, 100634 (2021).

95. Zenyuk, I. V & Litster, S. Modeling ion conduction and electrochemical reactions in water films on thin-film metal electrodes with application to low temperature fuel cells. *Electrochim. Acta* **146**, 194–206 (2014).

96. Saha, P. & Zenyuk, I. V. Electric Double Layer at the Polycrystalline Platinum–Electrolyte Interface Probed by the Electrokinetic Streaming Current Method. *J. Phys. Chem. C* **125**, 19706–19715 (2021).

97. Huang, K., Song, T., Morales-Collazo, O., Jia, H. & Brennecke, J. F. Enhancing Pt/C Catalysts for the Oxygen Reduction Reaction with Protic Ionic Liquids: The Effect of Anion Structure. *J. Electrochem. Soc.* **164**, F1448–F1459 (2017).

98. Yan, X. *et al.* Improving Oxygen Reduction Performance by Using Protic Poly(Ionic

Liquid) as Proton Conductors. *ACS Appl. Mater. Interfaces* **11**, 6111–6117 (2019).

99. Yasuda, T. & Watanabe, M. Protic ionic liquids: Fuel cell applications. *MRS Bull.* **38**, 560–566 (2013).

100. Avid, A. & Zenyuk, I. V. Ionic Liquid Modified Pt/C Electrocatalysts for the Oxygen Reduction Reaction in Polymer Electrolyte Fuel Cells. *ECS Meet. Abstr.* **MA2020-02**, 2155 (2020).

101. Pozo-Gonzalo, C. Oxygen Reduction Reaction in Ionic Liquids: An Overview BT - Electrochemistry in Ionic Liquids: Volume 2: Applications. in (ed. Torriero, A. A. J.) 507–529 (Springer International Publishing, 2015). doi:10.1007/978-3-319-15132-8_18

102. Khedekar, K. *et al.* Probing Heterogeneous Degradation of Catalyst in PEM Fuel Cells under Realistic Automotive Conditions with Multi-Modal Techniques. *Adv. Energy Mater.* **n/a**, 2101794 (2021).

103. Zhang, G.-R., Munoz, M. & Etzold, B. J. M. Boosting Performance of Low Temperature Fuel Cell Catalysts by Subtle Ionic Liquid Modification. *ACS Appl. Mater. Interfaces* **7**, 3562–3570 (2015).

104. Zhang, G.-R. *et al.* Tuning the Electrocatalytic Performance of Ionic Liquid Modified Pt Catalysts for the Oxygen Reduction Reaction via Cationic Chain Engineering. *ACS Catal.* **8**, 8244–8254 (2018).

105. Li, Y. *et al.* Modifying the Electrocatalyst–Ionomer Interface via Sulfonated Poly(ionic liquid) Block Copolymers to Enable High-Performance Polymer Electrolyte Fuel Cells. *ACS Energy Lett.* **5**, 1726–1731 (2020).

106. Avid, A. & Zenyuk, I. V. “Confinement effects for nano-electrocatalysts for oxygen reduction reaction”. *Curr. Opin. Electrochem.* (2020). doi:https://doi.org/10.1016/j.coelec.2020.09.001

107. Miran, M. S. *et al.* Key factor governing the physicochemical properties and extent of proton transfer in protic ionic liquids: ΔpKa or chemical structure? *Phys. Chem. Chem. Phys.* **21**, 418—426 (2018).

108. Kresge, A. J. What makes proton transfer fast. *Acc. Chem. Res.* **8**, 354–360 (1975).

109. Noda, A. *et al.* Brønsted Acid−Base Ionic Liquids as Proton-Conducting Nonaqueous Electrolytes. *J. Phys. Chem. B* **107**, 4024–4033 (2003).

110. Moschovi, A. M., Dracopoulos, V. & Nikolakis, V. Inter- and Intramolecular Interactions in Imidazolium Protic Ionic Liquids. *J. Phys. Chem. B* **118**, 8673–8683 (2014).

111. Rogers, R. D. & Seddon, K. R. Ionic Liquids--Solvents of the Future? *Science (80-. ).* **302**, 792 LP – 793 (2003).

112. Stamenkovic, V. R. *et al.* Improved Oxygen Reduction Activity on Pt<sub>3</sub>Ni(111) via Increased Surface Site Availability. *Science (80-. ).* **315**, 493 LP – 497 (2007).

113. George, T. Y., Asset, T., Avid, A., Atanassov, P. & Zenyuk, I. V. Kinetic Isotope Effect as a Tool To Investigate the Oxygen Reduction Reaction on Pt-based Electrocatalysts – Part I: High-loading Pt/C and Pt Extended Surface. *ChemPhysChem* **21**, 469–475 (2020).

114. Baker, D. R., Caulk, D. A., Neyerlin, K. C. & Murphy, M. W. Measurement of Oxygen Transport Resistance in PEM Fuel Cells by Limiting Current Methods. *J. Electrochem.*

*Soc.* **156**, B991 (2009).

115. Jahnke, T., Futter, G. A., Baricci, A., Rabissi, C. & Casalegno, A. Physical Modeling of Catalyst Degradation in Low Temperature Fuel Cells: Platinum Oxidation, Dissolution, Particle Growth and Platinum Band Formation. *J. Electrochem. Soc.* **167**, 13523 (2019).

116. Abbou, S., Tajiri, K., Medici, E., Haug, A. T. & Allen, J. S. Liquid Water Uptake and Contact Angle Measurement of Proton Exchange Membrane Fuel Cell (PEMFC) Electrodes. *ECS Trans.* **86**, 163–169 (2018).

117. Abbou, S. *et al.* Capillary Penetration Method for Measuring Wetting Properties of Carbon Ionomer Films for Proton Exchange Membrane Fuel Cell (PEMFC) Applications. *J. Electrochem. Soc.* **166**, F3227–F3233 (2019).

118. Mehrazi, S., Sarker, M., Mojica, F., Rolfe, P. & Chuang, P.-Y. A. A rheological approach to studying process-induced structural evolution of the microporous layer in a proton exchange membrane fuel cell. *Electrochim. Acta* **389**, 138690 (2021).

119. Berlinger, S. A., McCloskey, B. D. & Weber, A. Z. Understanding Binary Interactions in Fuel-Cell Catalyst-Layer Inks. *ECS Trans.* **80**, 309–319 (2017).

120. Zhang, H., Pan, J., He, X. & Pan, M. Zeta potential of Nafion molecules in isopropanol-water mixture solvent. *J. Appl. Polym. Sci.* **107**, 3306–3309 (2008).

121. Sobota, M. *et al.* Ligand Effects in SCILL Model Systems: Site-Specific Interactions with Pt and Pd Nanoparticles. *Adv. Mater.* **23**, 2617–2621 (2011).

122. Wang, T. *et al.* Enhancing oxygen reduction electrocatalysis by tuning interfacial hydrogen bonds. *Nat. Catal.* **4**, 753–762 (2021).

123. Makharia, R., Mathias, M. F. & Baker, D. R. Measurement of Catalyst Layer Electrolyte Resistance in PEFCs Using Electrochemical Impedance Spectroscopy. *J. Electrochem. Soc.* **152**, A970 (2005).

124. Goldin, M. M. *et al.* Open circuit potential shifts of activated carbon in aqueous solutions during chemical and adsorption interactions. *J. Appl. Electrochem.* **38**, 1369–1374 (2008).

125. Podlovchenko, B. I., Gladysheva, T. D. & Kolyadko, E. A. Experimental check-up of the relationship between transients of current and open circuit potential for strong adsorption of neutral species and ions on a hydrogen electrode. *J. Electroanal. Chem.* **552**, 85–96 (2003).

126. Rana, U. A., Forsyth, M., MacFarlane, D. R. & Pringle, J. M. Toward protic ionic liquid and organic ionic plastic crystal electrolytes for fuel cells. *Electrochim. Acta* **84**, 213–222 (2012).

127. Susan, M. A. B. H., Noda, A., Mitsushima, S. & Watanabe, M. Brønsted acid–base ionic liquids and their use as new materials for anhydrous proton conductors. *Chem. Commun.* 938–939 (2003). doi:10.1039/B300959A

128. Stevens, D. A., Hicks, M. T., Haugen, G. M. & Dahn, J. R. Ex Situ and In Situ Stability Studies of PEMFC Catalysts. *J. Electrochem. Soc.* **152**, A2309 (2005).

129. Borup, R. L. *et al.* Recent developments in catalyst-related PEM fuel cell durability. *Curr. Opin. Electrochem.* **21**, 192–200 (2020).

130. Ren, P. *et al.* Degradation mechanisms of proton exchange membrane fuel cell under typical automotive operating conditions. *Prog. Energy Combust. Sci.* **80**, 100859 (2020).

131. Schmittinger, W. & Vahidi, A. A review of the main parameters influencing long-term performance and durability of PEM fuel cells. *J. Power Sources* **180**, 1–14 (2008).

132. Stariha, S. *et al.* Recent Advances in Catalyst Accelerated Stress Tests for Polymer Electrolyte Membrane Fuel Cells. *J. Electrochem. Soc.* **165**, F492–F501 (2018).

133. Cheng, L. *et al.* Mapping of Heterogeneous Catalyst Degradation in Polymer Electrolyte Fuel Cells. *Adv. Energy Mater.* **10**, 2000623 (2020).

134. Liu, H., Epting, W. K. & Litster, S. Gas Transport Resistance in Polymer Electrolyte Thin Films on Oxygen Reduction Reaction Catalysts. *Langmuir* **31**, 9853–9858 (2015).

135. Jinnouchi, R., Kudo, K., Kitano, N. & Morimoto, Y. Molecular Dynamics Simulations on O2 Permeation through Nafion Ionomer on Platinum Surface. *Electrochim. Acta* **188**, 767–776 (2016).

136. Kurihara, Y., Mabuchi, T. & Tokumasu, T. Molecular Simulation of Oxygen Solubility and Diffusivity in Ionomer on Pt Surface. *ECS Trans.* **69**, 691–699 (2015).

137. Morawietz, T. *et al.* High-Resolution Analysis of Ionomer Loss in Catalytic Layers after Operation. *J. Electrochem. Soc.* **165**, F3139–F3147 (2018).

138. Ott, S. *et al.* Ionomer distribution control in porous carbon-supported catalyst layers for high-power and low Pt-loaded proton exchange membrane fuel cells. *Nat. Mater.* **19**, 77–85 (2020).

139. Orfanidi, A. *et al.* The Key to High Performance Low Pt Loaded Electrodes. *J. Electrochem. Soc.* **164**, F418–F426 (2017).

140. Katzenberg, A. *et al.* Highly Permeable Perfluorinated Sulfonic Acid Ionomers for

Improved Electrochemical Devices: Insights into Structure–Property Relationships. *J. Am. Chem. Soc.* **142**, 3742–3752 (2020).

141. Malek, K., Mashio, T. & Eikerling, M. Microstructure of Catalyst Layers in PEM Fuel Cells Redefined: A Computational Approach. *Electrocatalysis* **2**, 141 (2011).

142. Jung, C.-Y. *et al.* Engineering ionomer homogeneously distributed onto the fuel cell electrode with superbly retrieved activity towards oxygen reduction reaction. *Appl. Catal. B Environ.* **298**, 120609 (2021).

143. Iden, H. & Ohma, A. An in situ technique for analyzing ionomer coverage in catalyst layers. *J. Electroanal. Chem.* **693**, 34–41 (2013).

144. Garrick, T. R., Moylan, T. E., Yarlagadda, V. & Kongkanand, A. Characterizing Electrolyte and Platinum Interface in PEM Fuel Cells Using CO Displacement. *J. Electrochem. Soc.* **164**, F60–F64 (2016).

145. Andersen, S. M. Nano carbon supported platinum catalyst interaction behavior with perfluorosulfonic acid ionomer and their interface structures. *Appl. Catal. B Environ.* **181**, 146–155 (2016).

146. Cells, T. F. *et al.* Fuel Cell 2016 Multi-Year Research, Development, and Demonstration Plan. **2015**, 1–58 (2016).

147. Obermaier, M., Bandarenka, A. S. & Lohri-Tymozhynsky, C. A Comprehensive Physical Impedance Model of Polymer Electrolyte Fuel Cell Cathodes in Oxygen-free Atmosphere. *Sci. Rep.* **8**, 4933 (2018).

148. Barcia, O. E. *et al.* Application of the impedance model of de Levie for the

characterization of porous electrodes. *Electrochim. Acta* **47**, 2109–2116 (2002).

149. Lopes, P. P. *et al.* Relationships between Atomic Level Surface Structure and Stability/Activity of Platinum Surface Atoms in Aqueous Environments. *ACS Catal.* **6**, 2536–2544 (2016).

150. Van Cleve, T. *et al.* Tailoring electrode microstructure via ink content to enable improved rated power performance for platinum cobalt/high surface area carbon based polymer electrolyte fuel cells. *J. Power Sources* **482**, 228889 (2021).

151. Gubler, L., Dockheer, S. M. & Koppenol, W. H. Radical (HO●, H● and HOO●) Formation and Ionomer Degradation in Polymer Electrolyte Fuel Cells. *J. Electrochem. Soc.* **158**, B755 (2011).

152. Gasteiger, H. A., Panels, J. E. & Yan, S. G. Dependence of PEM fuel cell performance on catalyst loading. *J. Power Sources* **127**, 162–171 (2004).

153. Kruk, M., Li, Z., Jaroniec, M. & Betz, W. R. Nitrogen Adsorption Study of Surface Properties of Graphitized Carbon Blacks. *Langmuir* **15**, 1435–1441 (1999).